Lawrence Berkeley National Laboratory
Recent Work

Title

DYNAMICAL ELECTRON SCATTERING APPROXIMATIONS AND THEIR VALIDITY DOMAINS IN ELECTRON MICROSCOPY

Permalink

https://escholarship.org/uc/item/6v39x8pz

Author

Jap, Bing K.

Publication Date

1975-07-29

eScholarship.org Powered by the California Digital Library
University of California

RECEIVED
LAWRENCE
BERKELEY LABORATORY

JUL 29 1975

LIBRARY AND
DOCUMENTS SECTION

LBL-2870

DYNAMICAL ELECTRON SCATTERING APPROXIMATIONS AND THEIR VALIDITY DOMAINS IN ELECTRON MICROSCOPY

DONNER LABORATORY

Bing K. Jap
(Ph. D. thesis)

Prepared for the U. S. Energy Research and
Development Administration under Contract W-7405-ENG-48

TWO-WEEK LOAN COPY

This is a Library Circulating Copy which may be borrowed for two weeks. For a personal retention copy, call Tech. Info. Division,

LAWRENCE BERKELEY LABORATORY • UNIVERSITY OF CALIFORNIA •

LBL-2870

DISCLAIMER

This document was prepared as an account of work sponsored by the United States Government. While this document is believed to contain correct information, neither the United States Government nor any agency thereof, nor the Regents of the University of California, nor any of their employees, makes any warranty, express or implied, or assumes any legal responsibility for the accuracy, completeness, or usefulness of any information, apparatus, product, or process disclosed, or represents that its use would not infringe privately owned rights. Reference herein to any specific commercial product, process, or service by its trade name, trademark, manufacturer, or otherwise, does not necessarily constitute or imply its endorsement, recommendation, or favoring by the United States Government or any agency thereof, or the Regents of the University of California. The views and opinions of authors expressed herein do not necessarily state or reflect those of the United States Government or any agency thereof or the Regents of the University of California.

TABLE OF CONTENTS

ABSTRACT 1

I. INTRODUCTION AND REMARKS 3

II. THEORY OF ELECTRON SCATTERING BY ATOMS AND CRYSTALS. 12

A. Kinematic Approximation. 13

B. Phase Object Approximation 20

C. Higher Order Phase Object Approximation. 24

D. Multislice Dynamical Approximation 31

III. THE VALIDITY DOMAIN OF THE PHASE OBJECT APPROXIMATION. 36

A. The Structures of Crystals Used as our Test Objects. . . . 38

1. Anhydrous cytosine crystal 38

2. Disodium 4-oxypyrimidine-2-sulfanate hexahydrate ('DISOPS') 38

B. Method of Computation. 38

1. Diffracted wave. 41

a) Kinematic approximation. 42

b) Phase object approximation 43

c) Multislice dynamical approximation 46

2. A validity measure for the diffracted beam intensities. 47

3. The projected potential retrieved by the phase object approximation 48

4. The dissimilarity factor for the retrieved projected potential. 49

C. Results and Discussion 53

1. The validity of the kinematic approximation for the calculation of the diffracted beam intensity . . . 54

2. The validity of the phase object approximation for the calculation of the diffracted beam intensity. 65

3. The diffracted wave. 66

4. The validity of the phase object approximation for the retrieval of the projected potential 78

TABLE OF CONTENTS

IV. THE VALIDITY DOMAIN OF THE HIGHER ORDER PHASE OBJECT APPROXIMATION 88
A. Approximation 88
B. Calculation Method. 90
C. Results and Discussion. 90
1. The phase of the diffracted wave. 91
2. The image intensity 91
3. The validity of the higher order phase object approximation for the retrieval of the projected potential 95

V. VOLTAGE DEPENDENT CONTRAST IN ORGANIC CRYSTAL IMAGES. 99
A. "Optimum Defocus Condition" 101
B. Image Contrast of Crystals. 102
C. Image Wave and the Fourier Spectrum of the Image Intensity 104
D. Calculation Method. 105
E. Results and Discussion. 107

VI. CONSLUSION AND SUMMARY. 119

APPENDIX A: The Validity of the Kinematic Approximation for the Structural Determination of Biological Structures by Electron Microscopy. 123

APPENDIX B: Evaluation of the Integral [in Equation (8)] 126

ACKNOWLEDGMENTS 128

REFERENCES. 129

LBL-2870

DYNAMICAL ELECTRON SCATTERING APPROXIMATIONS AND THEIR VALIDITY DOMAINS IN ELECTRON MICROSCOPY

Bing K. Jap

Donner Laboratory
Lawrence Berkeley Laboratory
University of California
Berkeley, California 94720

ABSTRACT

The kinematic approximation, the phase object approximation and the multislice dynamical approximation have been derived following Feynman's path integral formulation of quantum mechanics. The higher order phase object approximation was, for the first time, developed in order to extend the validity domain of the phase object approximation. The validity domains of the kinematic approximation, the phase object approximation and the higher phase object approximation were evaluated. In this evaluation, the multislice dynamical approximation was considered to be exact and used also as standards of reference. It was shown that the validity of the diffracted beam intensities in the kinematic approximation at 100 keV, is limited to a small crystal thickness and remains approximately unchanged as electron accelerating voltage increases. On the other hand, the validity of the diffracted beam intensities in the phase object approximation at 100 keV is limited to a slightly smaller crystal thickness but increases as electron energy increases. The validity domains for the retrieval of the projected potential in the phase object approximation were determined for various electron

accelerating voltages. The validity domain for the higher order phase object approximation was also evaluated.

The effect of high voltage to the contrast of organic crystal images under "optimum defocus condition" was also studied. It was shown that the contrast increases with increasing electron energy. This increase in contrast is beneficial for the reduction of radiation damage. It was concluded, that high voltage electron microscopy not only gives the beneficial increase in contrast, but also gives a larger domain for the retrieval of the projected potential by the phase object approximation.

I. INTRODUCTION AND REMARKS

The discovery in 1927 of the diffraction of electrons by periodic arrays of atoms in crystals proved the wave nature of electron beams (Davisson, C.J. and Germer, L.H., 1927). It was then clear that electron diffraction could be used, in principle, for structural analysis of crystalline materials. The rigorous attempts to use electron diffraction for structural investigation of crystals did not come, however, until much later (Vainshstein, B.K. and Pinsker, Z.G., 1949; Vainshstein, B.K. et al, 1958; Imamov, R.M. and Pinsker, Z.G., 1965). Not until recently has electron diffraction been applied in the investigation of biological structures (see, for example, Parsons, D.F., 1968; Glaeser, R.M. and Thomas, G., 1969). Electron diffraction is therefore far behind x-ray diffraction as a tool for the structural study of crystals. The reason lies mainly in the difficulty in the interpretation of electron diffraction data. Unlike in x-ray diffraction, the multiple scattering effects appear to be more important in electron diffraction. The simple linear approximation, also called the Born approximation, is inadequate to explain the observed diffraction pattern intensities. A greater complication of interaction of the diffracted beams involved within the crystals occurs in electron diffraction.

Electron microscopy and electron diffraction have been widely used for many structural investigations in biological as well as materials science. Unlike x-ray diffraction and neutron diffraction techniques, electron microscopy can provide not only the crystallographical data from the diffraction pattern, but also the direct morphological information

from the image. With the selected area diffraction technique, an image and a diffraction pattern from the same area of the specimen can be easily obtained. Indeed, electron microscopy is able to record the amplitude and phase of the diffracted beams whereas the "phase problem" imposes the greatest task in x-ray diffraction studies. In comparison with x-rays, electrons interact strongly with each atom of the crystals. Electron microscopy, therefore, requires a much smaller specimen size. This is advantageous to the structural investigation of biological specimens such as viruses and macromolecules because of their inherently small specimen size which limits study by x-ray technique. Electron microscopy has been successfully used to reconstruct the three-dimensional structures of biological specimens with resolution poorer than $\sim$ 20 Å. A review describing the application of electron microscopical technique for three-dimensional reconstruction of biological structures has already been given (Lake, J.A., 1972). Another example which is suitable for electron microscopical investigation but not for x-ray studies is the study of the formation of defects and phases in organic crystals which has been especially well exploited in metallurgical research.

The very large scattering power of electrons can be a disadvantage in that multiple scattering effect occurs even in gas molecules of high atomic number (Schomaker, V. and Glauber, R., 1952; Glauber, R. and Schomaker, V., 1953). The dynamical scattering effect severely confounds then, the interpretation of the electron diffraction and electron image data. Erickson and Klug (1971) and others (Dorset, D. and Parsons, D.F., 1974) have claimed, however, the validity of the kinematic approximation for interpretation of the electron scattering by biological, periodic

objects. The basis of their claim is based mainly on the fact that, for relatively thin objects, the total intensity of the scattered electrons is much smaller than the intensity of the forward-scattered electrons together with the unscattered ones.* An attempt has been made in this laboratory (Quon, W.K., 1970) to investigate the significance of the dynamical effect in the determination of biological structure. It has been shown that the kinematic approximation, used in x-ray structural determination, was inadequate to be used for electron diffraction studies. Use of the relatively simple two beam dynamical theory did not give, however, any significant improvement in the determination. It was concluded that a more accurate dynamical approximation is needed to determine the crystallographic structure of biological crystals.

The use of electron microscopy as a tool for biological structural investigation is also limited by factors such as specimen hydration and radiation damage. Biological specimens which are associated with water in their natural state are normally maintained in a dehydrated condition in the high vacuum of the electron microscope. They may, therefore, become disordered during the dehydration process. Normally, dried specimens do not retain their native structure at the level of molecular and atomic detail.

Although the specimen dehydration problem is mainly technical in nature, it is only very recently that it has been partially overcome by approaches such as:

---

*The validity of the argument is discussed in detail in Appendix A.

a) the differentially pumped hydration stages (Matricardi, V.R. et al, 1972; Hui, S.W. and Parsons, D.F., 1974)

b) the closed, thin window environmental chambers (Joy, R.T., 1973)

c) the frozen specimen hydration technique (Taylor, K.A. and Glaeser, R.M., 1974).

Radiation damage due to the electron beams may impose a limiting factor for high resolution electron microscopical investigation of biological materials. Studies have shown that many biological specimens exposed to the electron beam are disordered before sufficient irradiation dose is attained for detection of the high resolution information (Glaeser, R.M., 1971, 1975). Although many remarkable methods such as staining, shadowing, replication and minimum exposure techique have been developed to overcome radiation damage, yet these methods are useful only to preserve medium resolution ($\sim$ 20 Å) information. There is, therefore, still a desperate need to resolve the biological structure down to the level of atomic detail without destroying the native object structure.

The use of high voltage electron microscopy may contribute a small amount to the reduction of radiation damage to the specimen under electron microscopical investigation. Experiments in high voltage electron microscopy have shown that the "critical exposure" which gives a measure of the electron dose beyond which meaningful results cannot be obtained, increases with electron accelerating voltage. For organic materials, the improvement in critical exposure at 1.0 MeV can be 2.5 to 3.0 times greater than at 100 keV (Glaeser, R.M., 1974). In principle, radiation damage can be overcome in the case of crystalline or periodic objects. The electron exposure can be substantially reduced by taking advantage

of the redundancy of the periodicity of the image. This technique is referred to as *Statistically Noisy Averaged Pictures* (Glaeser, R.M. et al, 1971), and has been successfully tested for the case where the specimen is a carbon replica of an optical diffraction grating (Kuo, I.M., 1975). With the use of hydrated specimens and reduction in irradiation dose technique, electron microscopy can be the most direct method for structural investigation of biological crystals or periodic specimens at the level of atomic dimensions.

Although the electron microscope was first developed as early as 1931 (Knoll, M. and Ruska, E., 1932), the use of electron microscopy for investigation of high resolution crystal structure became possible only in the last few years. It is only recently that the electron microscope has achieved sufficient resolving power to show crystal images at the level of atomic dimensions. Images of non-periodic and periodic structural features at resolution down to $\sim$ 3 Å have been reported (Iijima, S., 1971; Yada, K. and Hibi, T., 1969; Hashimoto H. et al, 1973; Ottensmeyer, R.P. et al, 1973). By detailed comparison between the observed crystal image at a resolution of about 6 Å and the images computed by the multislice dynamical formulation, Allpress et al (1969) were able to derive useful information regarding the nature of crystal defects. The image was calculated from the crystal structure determined by x-ray crystallographical technique. It is noteworthy that, in the multislice dynamical approximation, there is no invertible relationship between the object structure and the scattered electron wave. The object potential cannot, therefore, be retrieved from the image and the diffraction intensities. It is clear that the multislice dynamical formulation is useful only for a study of

electron scattering by crystals for the cases where the object structure is previously known. The main interest of electron microscopy and electron diffraction lies, however, in a structure determination of the object from the observed image and diffraction intensities. There is need, then, to have other dynamcial approximations which can be used to determine the structure of the object from electron microscopical data.

The objective of this research is to find a practical solution to the problem of dynamical scattering effects, which have been known to play an important role in the interpretation of the diffraction intensities and the high resolution image. The long term goal will be to retrieve the object structure from the high resolution object image and diffraction intensities. The method will be used for correction of the dynamical effect on electron micrograph images of biological specimens such as gap junction membranes, catalase and tobacco mosaic virus. The three-dimensional reconstruction of these objects at high resolution will be the ultimate goal.

The phase object approximation seems to be the simplest dynamical formulation for retrieving the projected potential of the object. It gives an invertible relationship between the projected potential and the transmitted wave: the transmitted wave from the object is directly proportional to the complex exponential of the projected potential. This approximation is derived on the basis that the scattering angle is sufficiently small. It can be obtained by summing the infinite Born series after approximating each term by the method of the stationary phase (Schiff, L.I., 1956), by the use of the partial wave method (Olsen, H. et al, 1957), by the application of WKB approximation (Moliere, G., 1947; Zeitler, E. and

Olsen, H., 1967; Schiff, L.I., 1968), by a physical optics approach (Cowley, J.M. and Moodie, A.F., 1957) and by imposing a small angle approximation to the scattering integral equation (Parzen, G., 1951; Berry, M.V., 1971). Because of the nature of the phase object approximation, its validity is limited to small angle scattering, depending in addition on the object thickness and on the electron accelerating energy; the thicker the object and the smaller the electron energy, the smaller will be the angular domain of validity. There is a limited domain in terms of resolution, specimen thickness and electron accelerating voltage beyond which the phase object approximation becomes invalid. Our concern here is, in part, to set up some criteria for the validity of the phase object approximation, and to determine its domain of validity.

In this manuscript, the phase object approximation is derived for the first time by Feynman's path integral formulation of quantum mechanics, which has a kind of simplicity that is often lost in the complex formulations of quantum mechanics. In the derivation, it is clear that the phase object approximation is valid only to a very small angle since the approximation assumes that high energy electrons, when passing through object potential, follow the classical straight line path. This assumption, therefore, becomes invalid as the object thickness increases.

It appears that the limitation of the phase object approximation can be overcome by considering that high energy electrons have a significant probability to be scattered at small angles. These electrons have to be considered in the derivation of the scattered wave function in order to get a more accurate description of the electron scattering. Results from this consideration lead to the multislice dynamical theory of Cowley and

Moodie (1957). Multislice dynamical theory does not give, however, a simple invertible relationship between the projected potential and the scattered wave. We develop, in this thesis, a new dynamical theory which takes into consideration that the electrons can be scattered at small angles and yet preserves the invertible characteristic of the phase object approximation. This we call the higher order phase object approximation (HOPO). Compared to the phase object approximation, this approximation is superior in accuracy, and has, therefore, a larger domain of validity. In order to retrieve the projected potential over a unit cell from the transmitted wave, this approximation requires, however, that the object thickness be known. For biological specimens such as membranes and viruses, this new approximation is particularly useful since the thickness of these objects can be determined by other electron microscopical techniques such as thin section technique.

In Chapter 2, the kinematic approximation as well as various dynamical approximations, the phase object approximation, the higher order phase object approximation, and the multislice dynamical approximation, are derived following Feynman's path integral formulation of quantum mechanics. The higher order phase object approximation is, for the first time, developed. Compared to the phase object approximation, this newly developed approximation is not only superior in accuracy but also preserves the invertible relationship of the phase object approximation.

Chapter 3 and 4 describe respectively the validity of the phase object approximation and of the higher order phase object approximation for structual studies of organic crystals. The domains of validity for both approximations are also evaluated. In this evaluation, the multi-

slice dynamical approximation is used as our standard of reference. A measure of validity of these approximations is based on the reliability factor of the projected potential that is retrieved by the approximation under consideration.

In Chapter 5, the voltage dependence of contrast is theoretically investigated for calculated images of crystals. The images were computed for various crystal thicknesses at the "optimum defocus condition". In biological specimens, a change in image contrast is related to the dose of irradiation for the interpretable image data. It is known that the higher the contrast, the smaller the dose of irradiation can be used and still have sufficient statistics of measurement to give the same amount of structural information. An increase in image contrast in high voltage microscopy means that the complication of data processing to reduce the dose of irradiation needed can be significantly reduced.

II. THEORY OF ELECTRON SCATTERING BY ATOMS AND CRYSTALS

The motion of electrons under the influence of a potential field can be described by the Schrödinger equation. The solution in terms of the Born series, however, either converges too slowly or else leads to results which are not easily interpreted. Bethe's dynamical theory of electron diffraction by crystals, for instance, gives a solution which is highly complicated and also tedious to be applied to cases where more than two scattered beams are considered. The first Born approximation, which is commonly used in x-ray diffraction study, appears to be inadequate to be applied in electron diffraction cases. The Born series, where the dynamical scattering effect is taken into account, seems to converge too slowly in the region where the first Born approximation fails significantly. There is need, therefore, for simple, interpretable formulations which give adequate account of the electron scattering processes.

The path integral formulation of quantum mechanics developed by Feynman (1948, 1965) appears to be a logical as well as an intuitive way of describing the electron scattering problem. It can associate the wave and particle duality in a natural manner. Furthermore, the classic limit arises naturally as a special case of quantum mechanics when the dimensions, masses, velocity, etc., are so large that the Planck constant can be considered infinitesimal when compared to the momentum of the particles. The path integral formulation has been shown to be consistent with the Schrödinger equation (Nelson, E., 1964).

In this chapter, the kinematic approximation as well as various dynamical approximations will be derived following the path integral

approach. A new dynamical approximation, the higher order phase object approximation, will also be developed.

A. Kinematic Approximation

The kinematic approximation or the first Born approximation (Scott, W.T., 1963; Schiff, L.I., 1955) was first derived by a first order perturbation treatment of scattering (Born, M., 1926). It assumes that the scattered waves are weak compared to the initial wave. The far field, Fraunhofer scattered wave can be shown to be a spherical wave with an amplitude proportional to the Fourier transform integral of the potential field. The derivation gives, however, no clear physical meaning of the approximation. Here the kinematic approximation will be obtained following the path integral formulation. With this approach, the kinematic approximation can be clearly interpreted as a single scattering process.

The wave function of the electron, $\psi(\vec{r})$, under the influence of the potential field of an atom or a crystal can be described by the following integral equation

$$\psi(\vec{r}) = \int \psi_o(\vec{r}_o) P(\vec{r},\vec{r}_o) d\vec{r}_o \qquad (1)$$

where $P(\vec{r},\vec{r}_o)$ is the propagator of the electron wave and $\psi_o(\vec{r}_o)$ is the initial wave function (Feynman, R.P. and Hibbs, A.R., 1965).

The propagator depends on the strength of the potential field and on the wavelength of the electron. It can be written as the path integral in going from the initial point $\vec{r}_o$ to the observation point $\vec{r}$ of the object, as follows (Feynman, R.P. and Hibbs, A.R., 1965)

$$P(\vec{r},t;\vec{r}_o,t_o) = \int_{\vec{r}_o}^{\vec{r}} \exp\left(-\frac{i}{\hbar}\int_{t_o}^{t} L(\dot{\vec{r}}',\vec{r}',t')dt'\right)\mathcal{D}\vec{r}' \qquad (2)$$

and,

$$L(\dot{\vec{r}}',\vec{r}',t') = \frac{1}{2}m\dot{\vec{r}}'^2 + V(\vec{r}',t')$$

where m, V and h are the electron mass, object potential and Planck's constant respectively; $\mathcal{D}\vec{r}'$ denotes the continuous sum of integrals over all possible paths.

For high energy electrons and weak object potential, such that $\left|\frac{i}{\hbar}\int^{t} V(r',t')dt'\right| << 1$, the exponential function which depends on the object potential can be expanded in a power series. The propagator function can thus be written as

$$P(\vec{r},t;\vec{r}_o,t_o) = \int_{\vec{r}_o}^{\vec{r}} \exp\left(-\frac{i}{\hbar}\int_{t_o}^{t}\frac{1}{2}m\dot{\vec{r}}'^2(t)dt'\right)\cdot\left[1 + \frac{i}{\hbar}\int_{t_o}^{t} V(\vec{r}',t')dt' + \text{higher order terms}\right]\mathcal{D}\vec{r}' \qquad (3)$$

In the case where the sum of the higher terms in the potential is much smaller than the first order term,* the propagator can be simplified to the following form (Feynman, R. P. and Hibbs, A. R., 1965):

---

*In crystalline objects, the contribution from the sum of many higher order terms in the potential to the large angle reflections may be quite significant because the amplitudes of these first-order reflections are also very small.

$$P(\vec{r}',t;\vec{r}_o,t_o) \cong \int_{\vec{r}_o}^{\vec{r}} \exp\left(-\frac{i}{\hbar}\int_{t_o}^{t}\frac{1}{2}\,m\dot{\vec{r}}''^2dt''\right)\mathcal{D}r''$$

$$+\frac{i}{\hbar}\int_{\vec{r}_o}^{\vec{r}} \exp\left(-\frac{i}{\hbar}\int_{t_o}^{t'}\frac{1}{2}m\dot{\vec{r}}''^2dt''\right)\left(\int_{t_o}^{t} V(\vec{r}',t')dt'\right)$$

$$\exp\left(-\frac{i}{\hbar}\int_{t'}^{t}\frac{1}{2}\,m\dot{\vec{r}}''^2dt''\right)\mathcal{D}\vec{r}'' \qquad (4)$$

where t' is the time at $t_o < t' < t$. $\mathcal{D}\vec{r}''$ includes the notion of integration for all paths between position and time $(\vec{r}_o,t_o)$ to $(\vec{r}',t')$ as well as between $(\vec{r}',t')$ to $(\vec{r},t)$, and also the integration over all possible values $\vec{r}'$. To avoid confusion in the integration of $V(\vec{r}',t')$ over t', we replace variable t' by s. The order of integration over the variable s and that over $\mathcal{D}\vec{r}''$ can be interchanged, and equation (4) becomes

$$P(\vec{r},t;\vec{r}_o,t_o) = \int_{\vec{r}_o}^{\vec{r}} \exp\left(-\frac{i}{\hbar}\int_{t_o}^{t}\frac{1}{2}\,m\dot{\vec{r}}''^2dt''\right)\mathcal{D}\vec{r}''$$

$$+\frac{i}{\hbar}\int_{t_o}^{t}\left[\int_{\vec{r}_o}^{\vec{r}} \exp\left(-\frac{i}{\hbar}\int_{t_o}^{s}\frac{1}{2}\,m\dot{\vec{r}}''^2dt''\right) V(\vec{r}',s)\right.$$

$$\left.\exp\left(-\frac{i}{\hbar}\int_{s}^{t}\frac{1}{2}\,m\dot{\vec{r}}''^2dt''\right)\mathcal{D}\vec{r}''\right] ds \qquad (5)$$

The first term is the propagator for the free electron. The second term is associated with the scattering by the potential field, and can be

interpreted as an electron starting from the incoming position $\vec{r}_o$, moving as a free particle to the point $\vec{r}'$, and then being scattered by the potential field of the object, after which it moves as a free particle to the point $\vec{r}$. It should be noted that the electron which is scattered at point $\vec{r}'$ has the possibility to be scattered in any direction (Fig. 1).

By substituting the propagator to equation (1), the wave function for the outgoing electron can be written as

$$\psi(\vec{r},t) = \int \psi_o(\vec{r}_o,t_o)\left[\int_{\vec{r}_o}^{\vec{r}} \exp\left(-\frac{i}{\hbar}\int_{t_o}^{t}\frac{1}{2}\,m\dot{\vec{r}}''^2 dt''\right)\mathcal{D}\vec{r}''\right] d\vec{r}_o$$

$$+ \frac{i}{\hbar}\int \psi_o(\vec{r}_o,t_o)\left[\int_{t_o}^{t}\left[\int_{\vec{r}_o}^{\vec{r}} \exp\left(-\frac{i}{\hbar}\int_{t_o}^{s}\frac{1}{2}\,m\dot{\vec{r}}''^2 dt''\right) V(\vec{r}',s)\right.\right.$$

$$\left.\left. \exp\left(-\frac{i}{\hbar}\int_{s}^{t}\frac{1}{2}\,m\dot{\vec{r}}''^2 dt''\right)\mathcal{D}\vec{r}''\right] ds\right] d\vec{r}_o \qquad (6)$$

where $\psi_o(\vec{r}_o)$ is the initial wave function of the electron.

The wave function for the incoming electron having momentum $\hbar\vec{k}_o$ and energy E_o can be described by $\exp\left(i\vec{k}_o\cdot\vec{r} - (\frac{i}{\hbar})E_o t\right)$. In equation (6), the propagator for an electron going from the interaction point $\vec{r}'$ to the point $\vec{r}$ can be represented by the following equation (Feynman, R.P. and Hibbs, A.R., 1965)

$$P(\vec{r},t';\vec{r}',o) = \left[\frac{m}{2\pi i\hbar t'}\right]^{3/2} \exp\left(-\frac{im\,|\vec{r}-\vec{r}'|^2}{2\hbar t'}\right) \qquad (7)$$

where t' is the time required for the electron to travel the distance

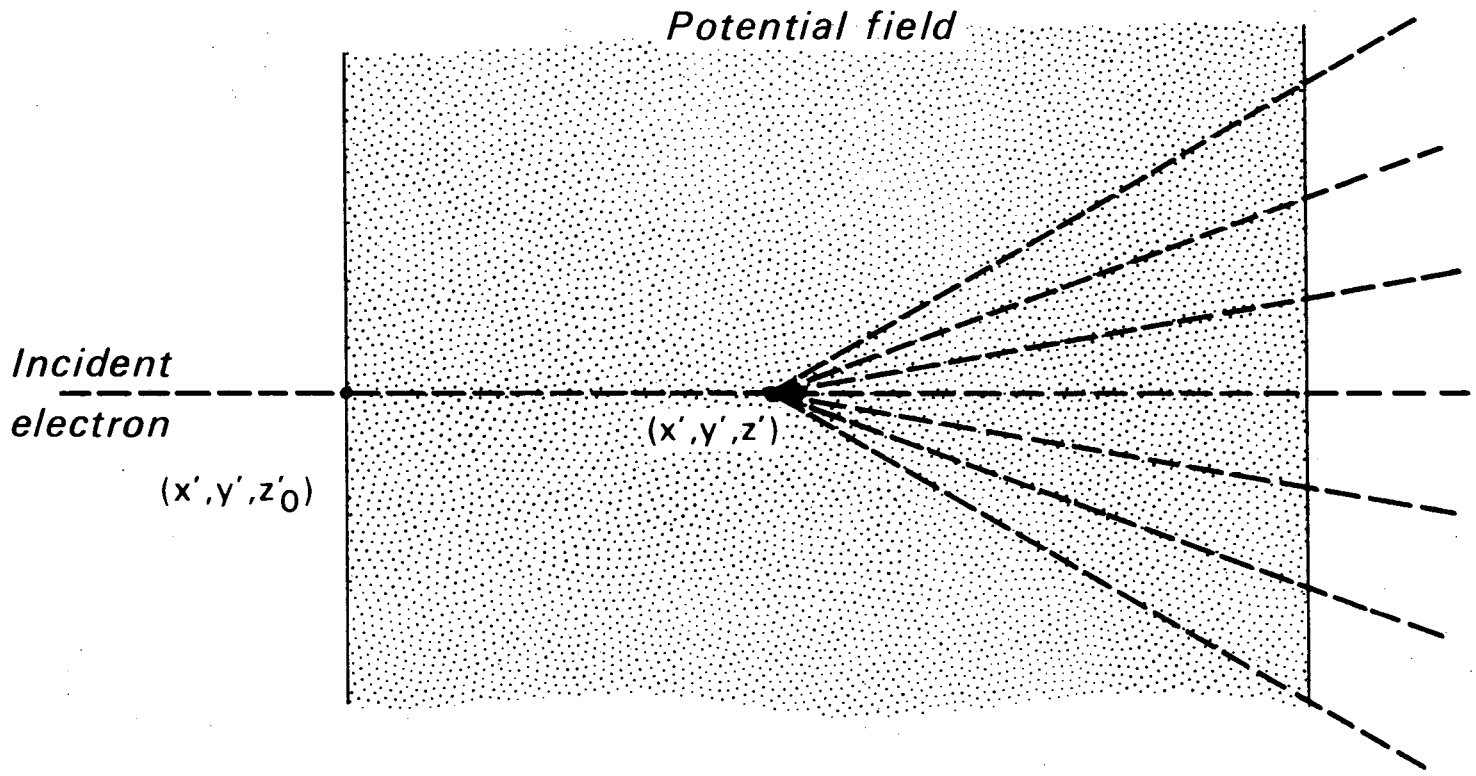

XBL 7412-8183

Figure 1. Schematic electron paths for the kinematic approximation: single scattering events can occur anywhere in the potential field with subsequent straight-line propagation at any angle.

$|\vec{r} - \vec{r}'|$. In this equation, we have assumed that the propagation is in the forward direction. The wave function for the outgoing electron can then be rewritten as

$$\psi(\vec{r},t) = \exp\left(-i\vec{k}_o \cdot \vec{r} + \left(\frac{i}{\hbar}\right) E_o t\right) + \frac{i}{\hbar} \int_0^t \int_{\vec{r}_o}^{\vec{r}} \exp\left(-i\vec{k}_o \cdot \vec{r}' + \left(\frac{i}{\hbar}\right) E_o t'\right) V(\vec{r}',t')$$

$$\cdot \left[\frac{m}{2\pi i\hbar t'}\right] \exp\left(-\frac{im|\vec{r} - \vec{r}'|^2}{2\hbar t'}\right) d\vec{r}'\, dt' \qquad (8)$$

where t is the time needed for electron to go from the initial position $\vec{r}_o$ to the final point $\vec{r}$. We have assumed here that the wave function at the initial position $\vec{r}_o = 0$ and at the time $t_o = 0$, can be described by $\exp\left(-i\vec{k}_o \cdot \vec{r}_o + (\frac{i}{\hbar})E_o t_o\right) = 1$. The first term in equation (8) is the wave function of the free electron which passed through the potential field without being scattered. The second term is the scattered wave function.

The outgoing wave function of the electron, for the far field region, can be obtained by setting $|\vec{r}| \to \infty$. After performing the integration over t' in equation (8), this wave function, for the case where the potential $V(\vec{r},t)$ is independent of t, can be expressed by the following relation (Appendix B)

$$\psi_\infty(\vec{r},t) = \exp\left(-i\vec{k}_o \cdot \vec{r} + (\frac{i}{\hbar}) E_o t\right) - \frac{m}{2\pi\hbar^2} \int \exp(-i\vec{k}_o \cdot \vec{r}')V(\vec{r}') \frac{\exp(-ik|\vec{r}-\vec{r}'|)}{|\vec{r} - \vec{r}'|} d\vec{r}' \qquad (9)$$

Noting that the wave function $\psi_\infty(\vec{r})$ is for the far field region, we can simplify this wave function by using the following approximation

$$\frac{\exp(-ik|\vec{r}-\vec{r}'|)}{|\vec{r}-\vec{r}'|} \underset{|\vec{r}|\to\infty}{\cong} \exp(i\vec{k}\cdot\vec{r}')\,\frac{\exp(-ikr)}{r} \qquad (10)$$

Thus we can write the wave function as

$$\psi_\infty(\vec{r},t) = \exp\left(-i\vec{k}_o\cdot\vec{r} + \left(\frac{i}{\hbar}\right)E_o t\right) - \frac{m}{2\pi\hbar^2}\,\phi(\vec{s})\,\frac{\exp(-ikr)}{r} \qquad (11)$$

where $\phi(\vec{s})$ is the Fourier transform of the potential and $\vec{s} = \vec{k}_o - \vec{k}$. Elastic scattering requires that $|\vec{k}_o| = |\vec{k}|$ so that the Fourier transform integral should be evaluated only on the Ewald sphere.

The amplitude of the scattered wave is, therefore, proportional to the Fourier integral over the potential of the object. For a crystalline object, the effective potential is limited to the object dimensions. The form of the crystal can be described by a shape function, $s(\vec{r})$, which is equal to zero outside the crystal and unity within it. A finite crystal of a given form is thus described by multiplication of the infinite periodic distribution with the shape function. The scattering amplitude of a finite crystal can be written as the convolution of the infinite crystal amplitude and the shape transform, $\Sigma(\vec{s})$.

$$F(\vec{k},\vec{k}_o) = \frac{m}{2\pi\hbar^2}\left[\phi(\vec{s}) * \Sigma(\vec{s})\right]' \qquad (12)$$

where $F(\vec{k},\vec{k}_o)$ is the scattering amplitude, * sign denotes a convolution and prime indicates that only those values that lie on the Ewald sphere are used.

This feature of the diffracted beams can be conveniently described by means of the Ewald sphere construction in reciprocal space. The

diffracted beams occur when the Ewald sphere intersects the reciprocal lattice points. For a finite crystal, each reciprocal point is spread out by the shape transform. The Ewald sphere may intersect the shape transform near to the reciprocal lattice point and give a diffracted beam.

The kinematic approximation can describe the pattern of the diffracted beams, but fails in most cases to give correct amplitudes, and especially phases of these beams. The fact that the kinematic approximation is inadequate even for heavy atom gas molecules was realized first by Schomaker and Glauber (1952, 1953), who tried to explain the anomalies in the gas diffraction pattern from UF_6 molecules. Recent results in a test study with the crystalline structure of β glycine have also shown that the kinematic approximation is insufficient for the description of the scattering of electrons by organic crystals (Quon, W.K., 1970). The dynamical effect, therefore, plays an important role in both electron diffraction and electron imaging of biological material.

B. Phase Object Approximation

Since the wavelength of an electron in the high voltage microscope is very small and since the object potential, at resolution comparable with atomic dimensions, varies slowly over a single electron wavelength, the electron can be considered to propagate through the object following the classical path. The classical approach may therefore be quite sufficient to describe electron diffraction by crystals for the high voltage microscope.

In the classical approximation, the single classical path is the only one which contributes to the path integral instead of a continuous

sum of integrals over all paths. For this case, the propagator from $(\vec{r}_o, t_o)$ to $(\vec{r}, t)$ can be written as the single path integral:

$$P(\vec{r},t;\vec{r}_o,t_o) = \exp\left(-\frac{i}{\hbar}\underbrace{\int_{t_o}^{t}\frac{1}{2}m\dot{\vec{r}}'^2dt'}_{\substack{\text{classical}\\\text{path}}} - \frac{i}{\hbar}\underbrace{\int_{t_o}^{t}V(\vec{r}')dt'}_{\substack{\text{classical}\\\text{path}}}\right) \tag{13}$$

where the first term is the propagator for the free electron. For a path length much greater than the electron wavelength, this term can be described by the plane wave $\exp\left(-i\vec{k}\cdot(\vec{r}-\vec{r}_o) + (\frac{i}{\hbar})E_o(t-t_o)\right)$. In the second term, the integral over the time t' can be converted to an integral over the electron trajectory by the use of the following relation between the electron velocity, $\vec{v}$, and the position and time

$$\vec{v} = \frac{\vec{r}'}{t'} \tag{14}$$

The propagator can then be written as

$$P(\vec{r},t;\vec{r}_o,t_o) = \exp\left(-\frac{i}{\hbar}\underbrace{\int_{t_o}^{t}\frac{1}{2}m\dot{\vec{r}}'^2dt'}_{\substack{\text{classical}\\\text{path}}} - \frac{i}{\hbar v}\underbrace{\int_{\vec{r}_o}^{\vec{r}}V(\vec{r}')d\vec{r}'}_{\substack{\text{classical}\\\text{path}}}\right) \tag{15}$$

where the integral is taken along the classical path trajectory.

For high energy electrons, the scattering is confined to a small angle. Thus, we can assume that the classical line path can be approximated by a straight line path parallel to the incident beam direction (Fig. 2). With such an approximation, the propagator without the time factor, $\exp\left((\frac{i}{\hbar})E_o(t-t_o)\right)$, can be written as

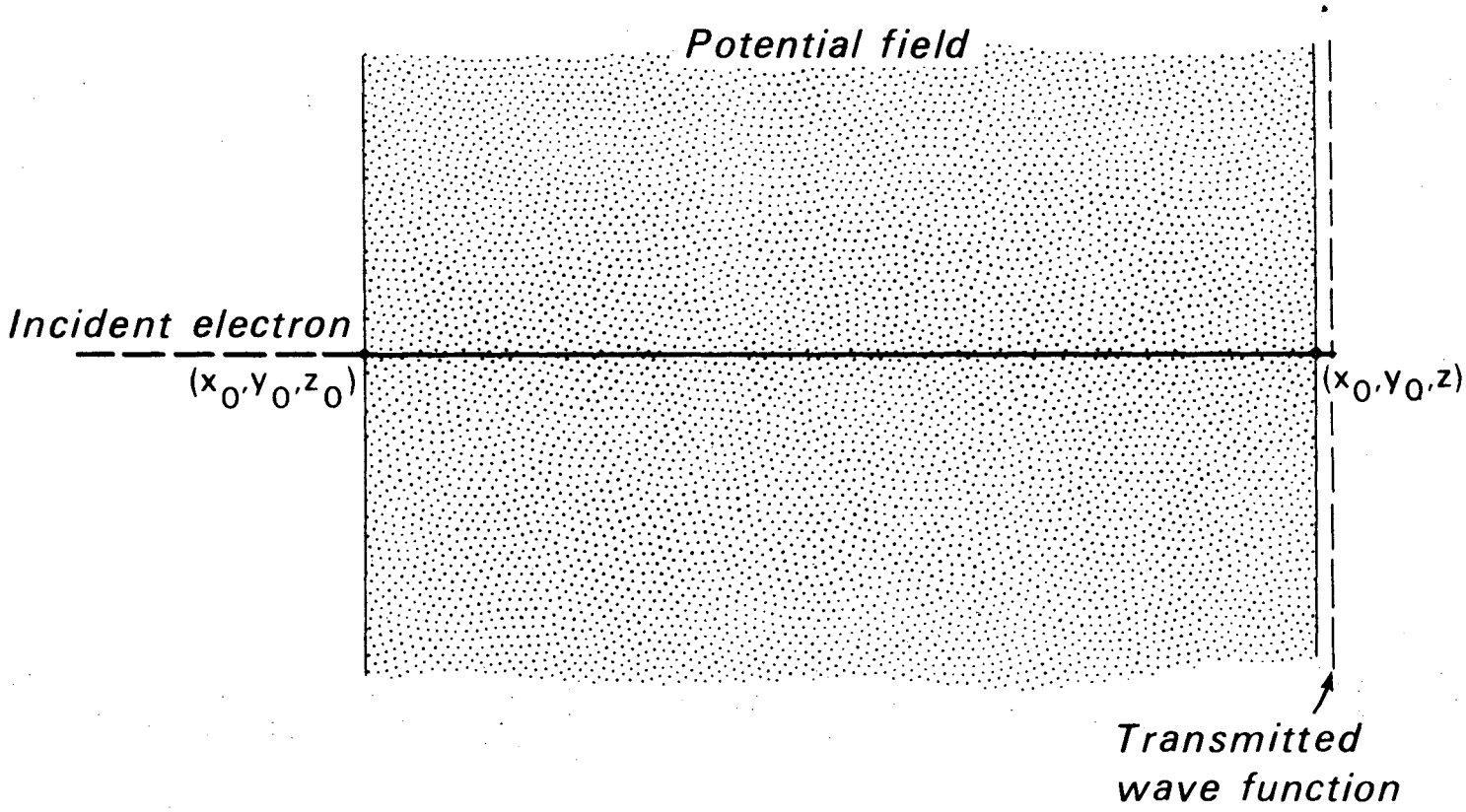

XBL 7412-8184

Figure 2. Schematic electron paths for the phase object approximation: multiple scattering processes occur along the straight-line path without any change in the direction of propagation.

$$P(\vec{r};\vec{r}_o) \cong \left[\exp\left(-i\vec{k}\cdot(\vec{Z}-\vec{Z}_o)\right)\cdot\exp\left(-\frac{i}{\hbar v}\int_{Z_o}^{Z} V(\vec{\rho},\vec{Z}')d\vec{Z}'\right)\right]\delta(\vec{x}-\vec{x}_o)\delta(\vec{y}-\vec{y}_o) \tag{16}$$

where δ is the Dirac delta function, $\vec{\rho} = (\vec{x},\vec{y})$. In equation (16), we have assumed that the incident beam direction is along the z-axis. The straight-line path approximation is valid only when both the integral of the potential as well as the kinetic energy over the classical line path at a small angle from the incident beam direction can be approximated by the integral over the straight line path parallel to the incident beam direction. In other words, the straight line path approximation is justified if and only if the following two conditions are satisfied. First, the difference in path length between the classical line path at a small angle and the straight line path parallel to the incident beam direction is much smaller than the electron wavelength, i.e.,

$$\frac{\Delta Z\theta^2}{2} \ll \lambda \tag{17}$$

In equation (17), θ is the scattering angle, ΔZ is the object thickness and λ is the electron wavelength. Equation (17) is also referred to as the stationary phase approximation (Schiff, L.I., 1956). Second, the potential does not change appreciably within the column diameter, d, associated with the angle of the stationary phase approximation (i.e., $d = \Delta Z\theta$).

The transmitted wave function, for a slab of a potential field of thickness ΔZ, can be obtained by substituting the propagator into equation (1). Noting the Dirac delta function in the propagator, we can

write the transmitted wave function as

$$\psi(\vec{\rho}) = \exp(-ik\Delta Z)\exp\left(-\frac{i}{\hbar v}\int_{Z_o}^{Z_o+\Delta Z} V(\vec{\rho},\vec{Z}')d\vec{Z}'\right) \tag{18}$$

where $\psi(\vec{\rho})$ is the transmitted wave function at the exit face of the slab, and $\vec{\rho} = (\vec{x},\vec{y})$.

Equation (18) is, of course, the transmitted wave function of the phase object approximation. The validity of this approximation depends on the electron wave length, the strength of the potential, the thickness of the object and the scattering angle.

Unlike the first Born approximation, the phase object approximation takes multiple scattering processes into account. The scattered wave in the phase object approximation is assumed to propagate in the same direction as the incoming electron wave. To the first order in potential, the phase object approximation is therefore not exactly the same as the first Born approximation. For a crystalline object, the phase object approximation can be loosely described by saying that its Ewald sphere is approximated as a plane, although it is known that the Ewald sphere construction cannot ordinarily be used to predict the amplitude of the diffracted beam intensity in the dynamical electron scattering approximation.

C. Higher Order Phase Object Approximation

The phase object approximation was derived under the condition that the electron propagates through the object following a straight line path. The validity of this approximation is limited to a very small angle and to a very thin object. For an object of sufficient thickness,

the phase object approximation fails to describe the electron scattering process. The need for an approximation which can be used for larger object thickness is therefore in demand. The expected approximation must, however, give an invertible relationship between the transmitted wave function and the object potential so that it can be used for correction of the dynamical scattering effect on the electron micrograph image. We develop here the higher order phase object approximation which has the required improvement in behavior.

The propagator for an electron influenced by the potential field $V(\vec{r})$ can be written as the separate sum of path integrals over the straight line and non-straight line paths. The propagator can then be described by

$$P(\vec{r},t;\vec{r}_o,0) = \frac{1}{N}\left\{\exp\left(-\frac{i}{\hbar v}\int_{\vec{r}_o}^{\vec{r}} V(\vec{r}')d\vec{r}' - i\vec{k}\cdot(\vec{r}-\vec{r}_o) + \left(\frac{i}{\hbar}\right)E_o t\right)\right.$$

$$\left.\delta(\vec{x}-\vec{x}_o)\delta(\vec{y}-\vec{y}_o) + \int' \exp\left(-\frac{i}{\hbar v}\int_{r_o}^{r} V(\vec{r}')d\vec{r}'\right.\right.$$

$$\left.\left.-\frac{i}{\hbar}\int_0^t \frac{1}{2}m\dot{\vec{r}}'^2 dt'\right)\mathcal{D}\vec{r}'\right. \qquad (19)$$

where the prime in the integral sign indicates that the integral is taken over all possible non-straight line paths and N is a normalizing factor.

In the previous chapter, the propagator for the phase object approximation was derived under the assumption that the contribution from the integral over all possible line paths but the straight line path, which is parallel to the incident beam direction, is negligible. For thin

objects and a weak potential field, this assumption can be expected to be valid. As the object thickness increases, however, the number of electrons that are scattered at larger angles becomes appreciable. The contribution from the integral over the straight line path as well as over the non-straight line paths to the propagators has to be considered therefore.

Let us assume that only those paths which follow the incident beam direction in a straight line path and then cascade along this path with subsequent straight line propagation, give significant contribution to the propagators of electrons passing through a laminar volume of potential field of thickness $\tilde{Z}_o$ (Fig. 3). The transmitted wave function derived by including these paths in the evaluation of the propagators can be expected to be superior in accuracy in comparison to that of the phase object approximation. Let us further assume that the scattering is limited to a small angle. For electron microscopy at high energy, this assumption is justified for reasonably thick objects because the electron momentum used is much larger than the momentum change due to interaction with the object potential field. However, as object thickness becomes very large, the number of electrons which undergo multiple scattering increases, and a large number of electrons are scattered at a large angle. In this case, the assumption breaks down. For a potential which is weak compared to the kinetic energy of the electron, the integral of the potential along any one of those non-straight line paths can be approximated by the integral along the straight line path parallel to the incident beam direction. The path integral of the kinetic energy can, however, be quite different for these two different path lines. The difference in

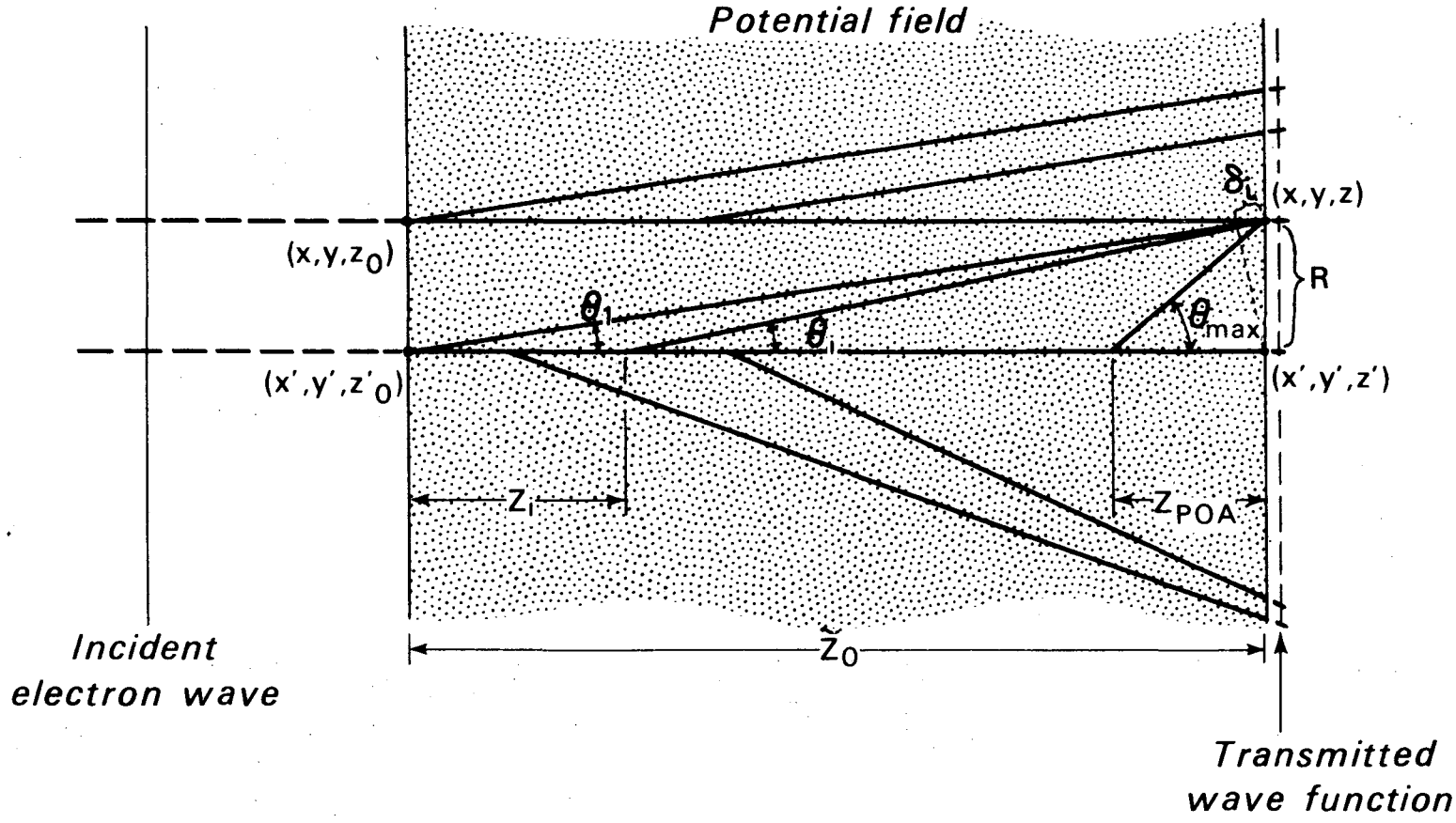

XBL 7412-8182

Figure 3. Schematic electron paths for the higher order phase object approximation: multiple scattering events occur along the straight line path and a change in direction of propagation can take place anywhere along the straight line path with subsequent propagation at small angle.

path length between the straight line and non-straight line path can be approximately described by

$$\delta_i = R(\vec{\rho},\vec{\rho}') \cdot \frac{\theta_i}{2}$$

and

$$\theta_i = \frac{R(\vec{\rho},\vec{\rho}')}{(\tilde{Z}_o - Z_i)} \tag{20}$$

where $R(\vec{\rho},\vec{\rho}') = \sqrt{(x-x')^2 + (y-y')^2}$ and $\tilde{Z}_o$ is object thickness. With this approximation, the propagator from r_o to r, without the time factor, $\exp\left(\left(\frac{i}{\hbar}\right)E_o t\right)$, can then be written as

$$P(r,r_o) = \frac{1}{N}\exp\left(-\frac{i}{\hbar v}\int_{Z_o}^{Z} V(\vec{\rho},Z')dZ' - ik\tilde{Z}_o\right) \cdot \left[\lim_{n\to\infty}\frac{1}{n}\sum_{i=1}^{n}\exp\left(-ikR(\vec{\rho},\vec{\rho}')\cdot\frac{\theta_i}{2}\right)\right] \tag{21}$$

where N is the normalizing factor and n is the total number of paths.

The sum over the angle θ_i should be restricted to some maximum value, in order to be consistent with the earlier assumption that the scattering angle is small. However, as Z approaches the object thickness, θ_i approaches a maximum value $\pi/2$. We know that the scattering of high energy electrons is confined mostly to a cone of a very small angle, and we are then left with the dilemma of how to specify this maximum angle.

In the case of the phase object approximation, we have assumed that the contribution of these non-straight line paths are negligible. The non-straight line path is insignficant for a object thickness where the phase object approximation is valid. With this idea in mind, we can set

the maximum angle as

$$\theta_{max} = \frac{R(\vec{\rho},\vec{\rho}')}{Z_{POA}}$$

and

$$R(\vec{\rho},\vec{\rho}') = \sqrt{(x-x')^2 + (y-y')^2} \tag{22}$$

where Z_{POA} is the object thickness for which the phase object approximation is valid up to the resolution, say 1 Å.

The sum of the series, depending on θ_i, in equation (21) can be expressed as an integral over θ as follows:

$$\lim_{n\to\infty} \frac{1}{n} \sum_{i=1}^{n} \exp\left(-ikR(\vec{\rho},\vec{\rho}') \frac{\theta_i}{2}\right) = \frac{\int_{\theta_1}^{\theta_{max}} \exp\left(-ikR(\vec{\rho},\vec{\rho}') \frac{\theta}{2}\right) d\theta}{\int_{\theta_1}^{\theta_{max}} d\theta}$$

After performing this integration, we can substitute the result into equation (21). We have then

$$P(\vec{r},\vec{r}_o) = \frac{1}{N} \exp\left(-\frac{i}{\hbar v}\int_{Z_o}^{Z} V(\vec{\rho},\vec{Z}')dZ' - ik_o\tilde{Z}_o\right) \left[\frac{\exp\left(-ikR(\vec{\rho},\vec{\rho}') \frac{\theta_{max}}{2}\right) - \exp\left(-ikR(\vec{\rho},\vec{\rho}') \frac{\theta_1}{2}\right)}{-ikR(\vec{\rho},\vec{\rho}')(\theta_{max} - \theta_1)}\right] \tag{23}$$

where $\theta_1 = \frac{R(\vec{\rho},\vec{\rho}')}{\tilde{Z}_o}$.

Substituting the propagator into equation (1) and also using equation (22) for θ_{max}, the transmitted wave function $\psi(\vec{\rho})$ can be described

by the following integral, which is carried out over the initial plane,

$$\psi(\vec{\rho}) = \frac{1}{N}\int \exp\left(-\frac{i}{\hbar v}\int_{Z_o}^{Z} V(\vec{\rho},\vec{Z}')d\vec{Z}' - ik\tilde{Z}_o\right)$$
$$\left[\frac{\exp\left(-ikR^2(\vec{\rho},\vec{\rho}')/2\tilde{Z}_o\right) - \exp\left(-ikR^2(\vec{\rho},\vec{\rho}')/2Z_{POA}\right)}{-ikR^2(\vec{\rho},\vec{\rho}')\left(\frac{1}{\tilde{Z}_o} - \frac{1}{Z_{POA}}\right)}\right]d\rho' \quad (24)$$

for $Z > Z_{POA}$. In this equation, we have assumed that the wave function at the initial plane $Z_o = 0$ can be described by $\exp(-i\vec{k}\cdot\vec{Z}_o) = 1$. Equation (24) is the transmitted wave function for the high order phase object approximation. In order to be consistent with the small angle approximation, the integral in equation (24) should be limited to values corresponding to a small angle. However, we have assumed that the integral of the potential energy along non-straight line paths can be approximated as an integral along the straight line path parallel to the incident beam direction. This means that the assumption is valid when the amplitudes of the diffracted waves at large angles are very small. In this case, the integration in equation (24) can be performed over all values without making a significant error to the transmitted wave function.

The complex wave amplitude of the diffracted electrons can be written as the Fourier transform of the object's transmitted wave function. We then have

$$F(\vec{k},\vec{k}_o) = \exp(-ik\tilde{Z}_o)\mathcal{F}\left[\frac{1}{N}\exp\left(-\frac{i}{\hbar v}\int_{Z_o}^{Z} V(\vec{\rho},\vec{Z}')d\vec{Z}\right)*\right.$$
$$\left.\left[\frac{\exp\left(-ik\frac{\rho^2}{2\tilde{Z}_o}\right) - \exp\left(-ik\frac{\rho^2}{2Z_{POA}}\right)}{-ik\rho^2\left(\frac{1}{\tilde{Z}_o} - \frac{1}{Z_{POA}}\right)/2}\right]\right], \quad \text{for } \tilde{Z}_o > Z_{POA} \quad (25)$$

where * sign denotes a convolution, $\mathcal{F}$ is a Fourier transform operator, and N is the normalizing factor. This is the diffracted wave for the higher order phase object approximation. Its validity can be expected to depend on the strength of the potential, the object thickness and the scattering angle.

D. Multislice Dynamical Approximation

The multislice dynamical approximation was first developed by Cowley and Moodie (1957) on the basis of the theory of physical optics. In their formulation, they considered that the electron wave passing through the potential field of a finite domain suffers a phase modification not only due to the effect of the potential field but also due to the spread of the wave by the Fresnel propagation processes. They have also shown that, for a periodic potential, the multislice dynamical approximation reduces to Bethe's two beam dynamical formulation only when the forward scattered beam and one diffracted beam have dominant amplitudes (Cowley, J.M., and Moodie, A.F., 1957). Furthermore, Fujiwara (1959) has shown that application of the higher order Born approximation to obtain the general solution for electron scattering by crystals leads to the multislice approximation. It has been reported that by comparison of the calculated and observed diffraction intensities and/or the image intensities, much important information about the object has been obtained (Allpress, J. G. et al, 1969).

It should be expected that the path integral formulation of quantum mechanics can be used to derive the multislice approximation. To show this, the multislice dynamical approximation is derived in order to

demonstrate the unity of the scattering approximations treated in this thesis. The propagator of an electron passing through a slab of a potential field can be described by the path integral equation (2). The path integral can be obtained by dividing the potential field into n-slices of thickness ΔZ. Within each slice, we assume that only the straight line paths will give a significant contribution to the propagator (Fig. 4). The validity of this assumption depends on the thickness of the slice taken as well as on the strength of the potential field. The difference in path length between the electron passing through the straight line path and the one scattered at a certain angle is

$$\Delta_i = \sqrt{R_i^2(\vec{\rho},\vec{\rho}'_{i-1}) + \Delta Z_i^2} - \Delta Z_i \tag{26}$$

where $R_i(\vec{\rho},\vec{\rho}'_{i-1}) = \sqrt{(x - x'_{i-1})^2 + (y - y'_{i-1})^2}$, $\vec{\rho} = (\vec{x},\vec{y})$ and ΔZ_i is the thickness of the ith slice. Let us assume that the slice is very thin and that the electron momentum is much larger than the change of the momentum due to interaction with the potential field. In this case, the probability of an electron being scattered at a large angle as it passes through a slice of potential field can be neglected. The electrons can be said to be scattered mostly into a small angle. The difference in path length can then be approximated as

$$\Delta_i = \frac{R_i^2(\vec{\rho},\vec{\rho}'_{i-1})}{2\Delta Z_i} = \frac{\Delta Z_i\, \theta_i^2}{2} \tag{27}$$

This path difference contributes an additional phase change to the scattered wave function of the phase object approximation. This phase change is due to the contribution from the potential energy as well as

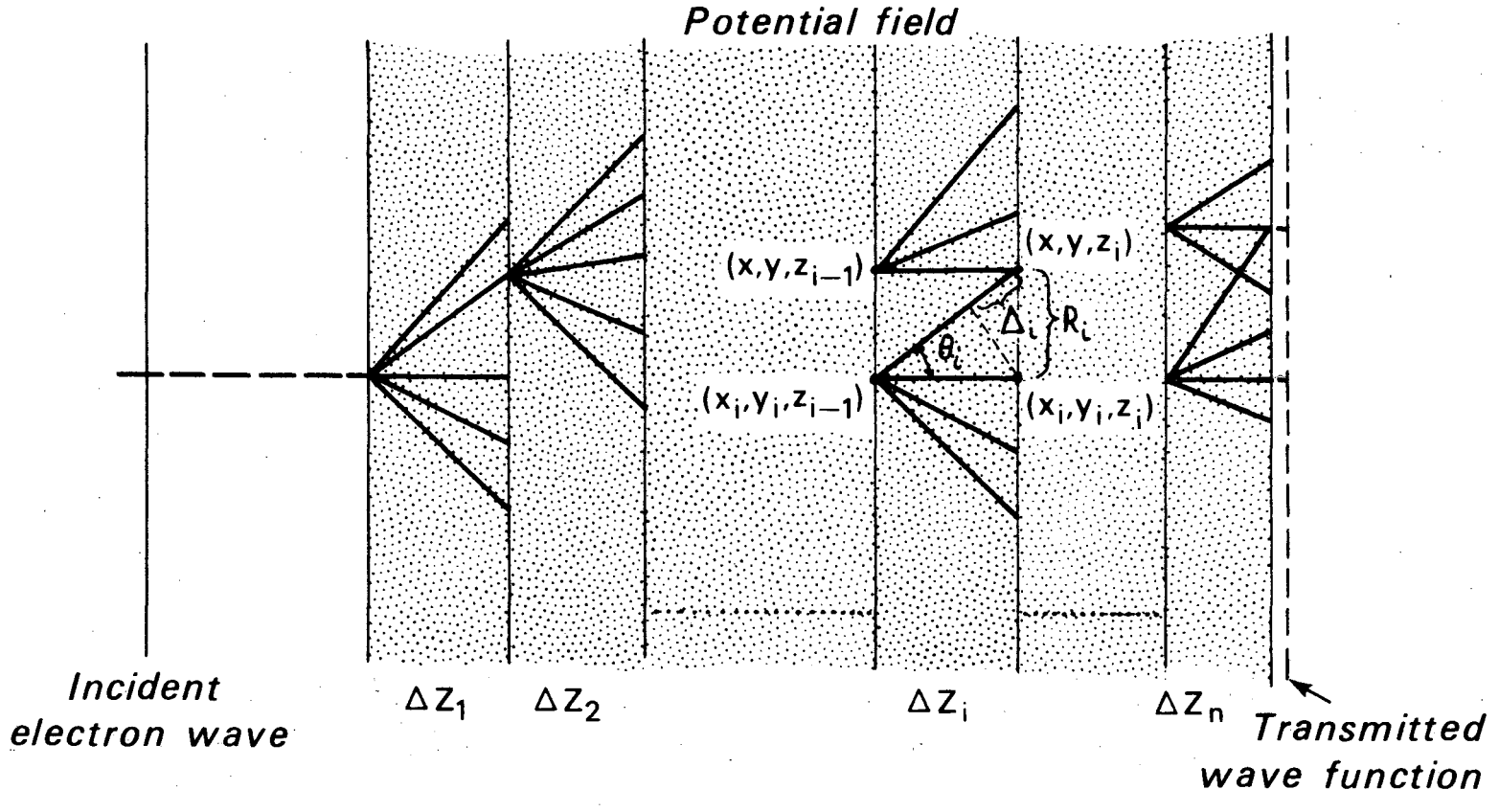

XBL 7412-8181

Figure 4. Schematic electron paths for the multislice dynamical approximation: the potential field is divided into n-slices. In each slice, multiple scattering events occur along the straight line paths. Only those paths which originate at the entrance face of the slice are considered in the evaluation of the transmitted wave function. The transmitted wave function at the exit face of the ith slice is related to the transmitted wave function of the (i-1)th slice and can be described recursively by equation (31).

from the kinetic energy of the electron. Since the object potential is small compared to the kinetic energy of electrons at significantly high energy, the contribution from the potential energy, because of the very small difference in path length, can therefore be neglected. The propagator $P(\vec{r},\vec{r}')$ following the straight line path from a point $\vec{r}'$ at the exit face of the slice can then be written as

$$P(\vec{r},\vec{r}') = \exp\left(-\frac{i}{\hbar v}\int_{Z_{i-1}}^{Z_i} V(\vec{\rho},\vec{Z}')d\vec{Z}'\right) - ik(\vec{r}-\vec{r}') \tag{28}$$

where $\vec{\rho} = (\vec{x},\vec{y})$ and Z_{i-1}, Z_i are, respectively, the z-coordinates of the entrance and the exit face of the ith slice.

The transmitted wave function emerging from the exit face of the ith slice can be described by the following equation

$$\psi_i(\vec{\rho}_i) = \int \psi_{i-1}(\vec{\rho}'_{i-1})P(\vec{\rho},\vec{\rho}'_{i-1})d\vec{\rho}'_{i-1} \tag{29}$$

where $\psi_i(\vec{\rho}_i)$ and $\psi(\vec{\rho}_{i-1})$ are, respectively, the transmitted wave function emerging from the exit face of the ith and the (i-1)th slice, and $P(\vec{\rho},\vec{\rho}')$ is the propagator function. We have then

$$\psi_i(\vec{\rho}) = \int \psi_{i-1}(\vec{\rho}'_{i-1})\exp\left(-\frac{i}{\hbar v}\int_{Z_{i-1}}^{Z_i} V(\vec{\rho},\vec{Z}')dZ' - ik\left(\Delta Z_i + \frac{R_i^2(\vec{\rho},\vec{\rho}'_{i-1})}{2\Delta Z_i}\right)\right)d\vec{\rho}'_{i-1} \tag{30}$$

where ΔZ_i is the slice thickness of the ith slice. The integral over $\vec{\rho}'_{i-1}$ should be limited to values which are associated with a small angle. For objects whose diffracted beam intensities at very large angles are very small compared to those at small angles, the integration can be

performed over all possible values of $\vec{\rho}'_{i-1}$ without giving significant error to the transmitted wave function.

Since the potential does not depend on the variable $\vec{\rho}'_{i-1}$, the exponential function, depending on $V(\vec{\rho},\vec{Z}')$, can be factored out from the integration. Equation (30) can be rewritten as

$$\psi_i(\vec{\rho}) = \exp(-ik\Delta Z_i)\left[\psi_{i-1}(\vec{\rho}) * \exp\left(-\frac{ik\rho^2}{2\Delta Z_i}\right)\right] \cdot \exp\left(-\frac{i}{\hbar v}\int_{Z_{i-1}}^{Z_i} V(\vec{\rho},\vec{Z}')d\vec{Z}'\right) \quad (31)$$

where * sign represents a convolution. This is the recursion relation for the diffracted wave in the multislice approximation. The transmitted wave function through the sequence of n-slices may be described recursively by this equation.

The validity of the multislice approximation depends on the electron energy relative to the strength of the object potential and on the thickness of the slice taken. It is noteworthy in the limiting case, that the slice thickness goes to zero and the number of slices goes to infinity, such that their product remains constant and equal to the object thickness. Then the multislice approximation becomes consistent with the conventional quantum mechanical description (Moodie, A.F., 1971).

III. THE VALIDITY DOMAIN OF THE PHASE OBJECT APPROXIMATION

The phase object approximation offers an attractive solution for the correction of the dynamical electron scattering effect in high resolution electron micrograph images. Unlike other, more complex dynamical approximations, it gives a simple and yet invertible relationship between the transmitted wave function and the projected object potential (18). In other words, the phase object approximation can be used to obtain the true structural information when the phase and amplitude of the diffracted wave,* which suffers dynamical scattering processes, are known. Several electron microscopical techniques together with data processing have been proposed for the recovery of the diffracted wave. One of the attractive techniques, in the author's opinion, is the half aperture holography technique. It is not, however, the purpose of this manuscript to deal with the recovery of the diffracted waves. We leave this problem aside for future research.

It is essential to determine the validity domain of the phase object approximation before it can be readily applied to correct the dynamical scattering effect in the electron micrograph image. The phase object approximation assumes that the scattering angle is very small, such that the paths of the scattered electron can be approximated by a straight line path. Its validity depends, therefore, on the electron energy, the strength of the object potential and also the object thickness. For a given object and electron energy, the phase object approximation is

---

*The diffracted wave is defined as the Fourier spectrum of the transmitted wave function.

expected to be accurate for a limited range of scattering angles. This means that the approximation is valid only for limited image resolution, since for a given electron energy, large angle scattering is associated with the high resolution information of the image. As the specimen thickness increases, more electrons undergo multiple scattering processes. This results in an increasingly significant change in the number of electrons scattered at larger angles. The phase object approximation can then be expected to give progressively more incorrect scattering amplitudes for the large angle reflections. Consequently, its validity will be limited to an increasingly lower resolution. At high energies, electron scattering is confined to a smaller angle, and the phase object approximation can be expected to be reliable for much thicker specimens. There is a domain, therefore, in terms of resolution, electron energy and specimen thickness where the phase object approximation is valid. This chapter intends to describe this validity domain.

In this manuscript, only the elastically scattered electron from a perfect crystal are considered because the inelastic scattering as well as the thermal motion effect complicate rather than dominate the whole treatment of the dynamical scattering.

We use the two organic crystals, *anhydrous cytosine* and *disodium 4-oxypyrimidine 2-sulfanate, hexahydrate* as our test objects for the determination of the validity domain of the phase object approximation. These crystals differ not only in their structures but also differ significantly in their unit cell dimensions. The difference in unit cell dimension means that a larger range in resolution can be used for the determination of the validity of the phase object approximation.

The use of two different crystals can also show that the domain of validity determined here does not depend on the specificity of the crystal structure.

A. The Structures of Crystals Used As Our Test Objects

1. Anhydrous Cytosine Crystal

The structure of the anhydrous cytosine crystal, $C_4H_5N_3O$, has been determined by x-ray crystallography (Barker, D. L., Marsh, R. E., 1964). The unit cell dimensions are a = 13.041 Å, b = 9.404 Å, and c = 3.815 Å. The crystals are orthorhombic with space group $P2_12_12_1$. The model structure of this crystal viewed down the c-axis is given in Fig. 5a.

2. Disodium 4-oxypyrimidine-2-sulfanate hexahydrate ('DISOPS')

The crystal structure of 'DISOPS', $(Na_2C_4H_2N_2OSO_26H_2O)$, has been previously determined by x-ray analysis (Sletten, J., 1969). The crystals are orthorhombic with space group Pcbm. The crystal contents are a = 9.299 Å, b = 20.253 Å, and c = 6.946 Å. The model structure of the crystal projected along the c-axis is given in Fig. 6a.

B. Method of Computation

The computation falls into five major parts:

1) The calculation of the diffracted waves, which emerge from the specimen of any given thickness, following either the phase object or multislice dynamical approximation.
2) The determination of the validity domain for the diffracted beam intensities calculated by either the kinematic approximation or the phase object approximation.

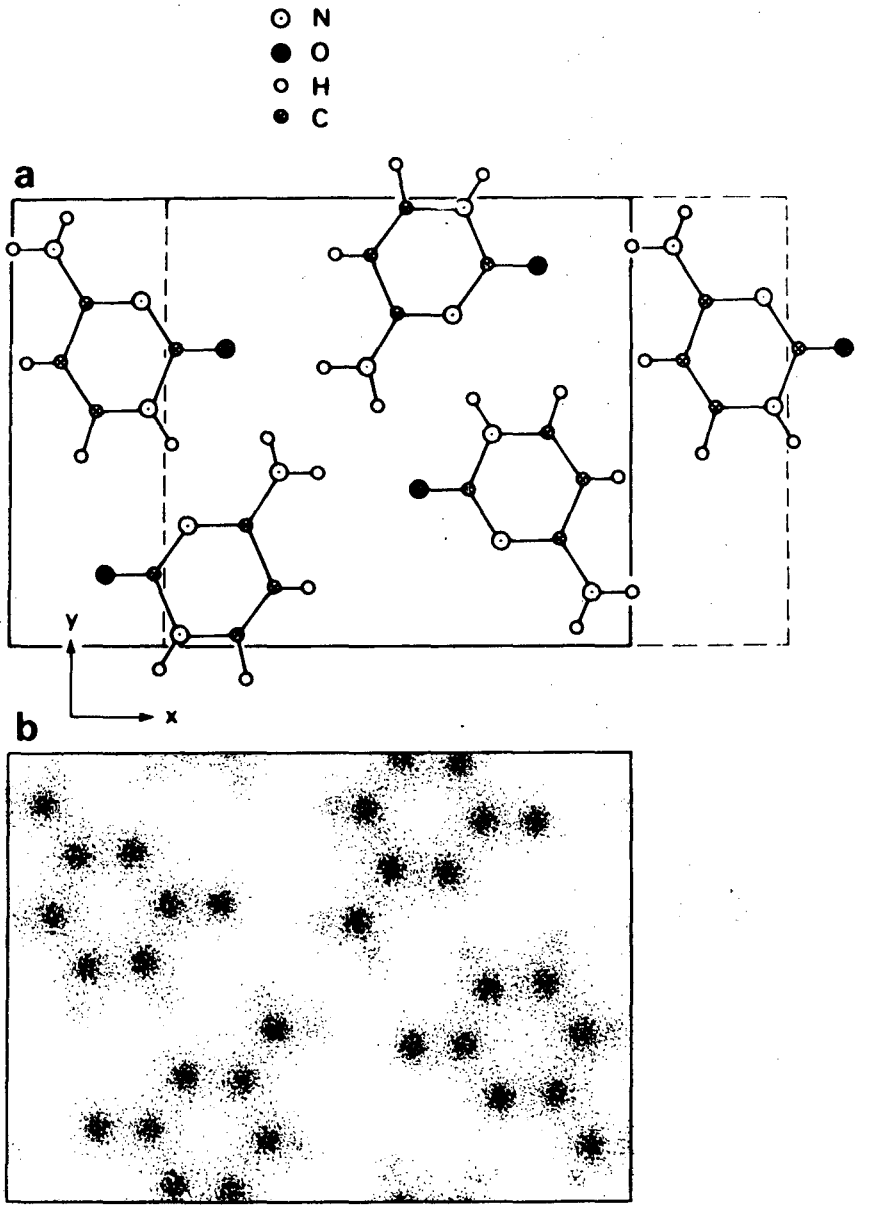

XBL 753-359

Figure 5. a) The model structure of cytosine crystal viewed down the c-axis. The dashed frame indicates the unit cell while the solid frame shows the projected potential being centro-symmetric.

b) The displayed projected potential of cytosine crystal viewed down the c-axis. The information in this is limited to a spatial frequency of less than 2.0 $\mathring{A}^{-1}$.

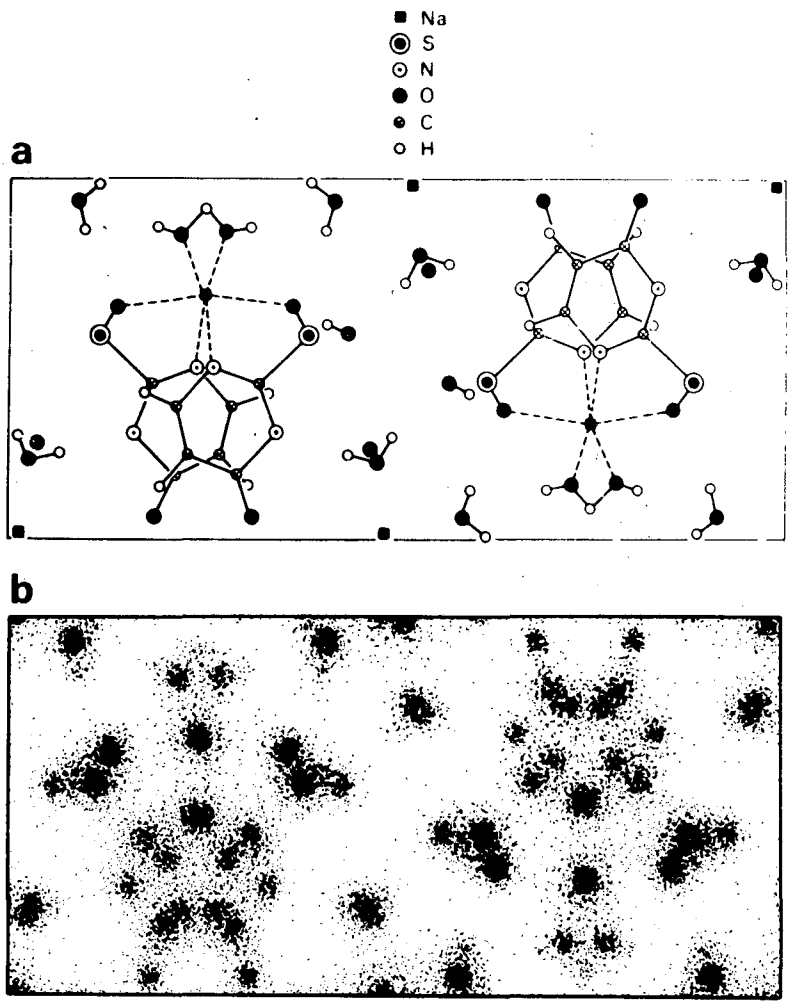

XBL 753-358

Figure 6. a) The model structure of 'DISOPS' viewed down the c-axis.

b) The displayed projected potential of 'DISOPS' viewed down the c-axis. The information in this display is limited to a spatial frequency of less than 2.0 $Å^{-1}$.

3) The computation of the projected potential, retrieved by the phase object approximation from the diffracted wave function, but which is calculated originally by the multislice dynamical approximation.

4) The calculation of the deviation between the retrieved projected potential and the 'true' projected potential.

5) The computation of the dissimilarity factor for the retrieved projected potential.

All of these computations are outlined by the flow diagram (Diagram 1).

1. Diffracted Wave

The first step in the computation of the diffracted wave using either the phase object or multislice dynamical approximation, is to calculate the projected potential of the crystal. This projected potential along the z-axis can be represented by the following equations

$$\begin{aligned} V(x,y) &= \mathcal{F}[F(h,k,0)] \\ F(h,k,0) &= \sum_{j=1}^{n} f_j(h,k) e^{2\pi i(hx_j + ky_j)} \end{aligned} \tag{32}$$

where $F(h,k,0)$ is the Fourier spectrum of the projected potential in the z-direction, f_j and (x_j,y_j) are, respectively, the atomic form factor and the atomic position of the j-atom in the crystal unit cell, n is the number of atoms in a crystal unit cell, and $\mathcal{F}$ is the Fourier transform operator.

The atomic form factors used here, except for the hydrogen atom, were calculated from the analytic function whose parameters were obtained by Doyle and Turner (1968) through curve fitting with the values calculated

using the relativistic Hartree Fock atomic field. The form factor for hydrogen was obtained from values given in the International Table for X-ray Crystallography (1968).

A fast Fourier transform algoirthm (Singleton, R. C., 1969) was used in the computation. It should be noted here, that the Fourier coefficients for the construction of the projected potential are limited to a finite number of reflections. In the calculation of the projected potentials, the Fourier spectrum was truncated at the spatial frequency of 2.0 $\mathring{A}^{-1}$. The projected potentials are displayed by the two dimension 'z-modulation display' (Fig. 5b, 6b).

(a) Kinematic Approximation

The kinematic approximation, because of its simplicity, is the most attractive approximation for structural analysis by diffraction technique. Its validity in electron microscopy still remains however, a controversial topic. In order to obtain some quantitative measure about its validity for the structural investigation of organic crystals, the kinematic approximation is used to compute the diffracted wave which is then compared with the diffracted wave calculated by the most accurate electron scattering approximation. The diffracted wave in the kinematic approximation can be described by equation (12). The shape transform for a finite parallel slab of crystal can be represented by

$$\Sigma(S_z) = \frac{\sin\pi S_z H}{\pi S_z H} \tag{33}$$

where $\Sigma(S_z)$ is the shape transform for crystal thickness H, and S_z corresponds to the z-component of the wave vector. The diffracted wave

can then be described by

$$F_{kin}(h,k) = \begin{cases} 1 & \text{when } h = k = 0 \\ iF(h,k,0)\dfrac{\sin\pi\xi(h.k)H}{\pi\xi(h,k)H} & \text{otherwise} \end{cases} \qquad (34a)$$

and

$$\xi(h,k) = \lambda/2\left(\frac{h^2}{a^2} + \frac{k^2}{b^2}\right) \qquad (34b)$$

where $\xi(h,k)$ is the excitation error for the (h,k) reflection, λ is the electron wavelength, and a,b are crystal unit cell dimensions.

(b) Phase Object Approximation

In the phase object approximation, the diffracted wave for a finite slab of crystal of thickness H can be described by the following equation,

$$F^H_{POA}(h,k) = \mathfrak{F}\left[\exp\left(-i\sigma\int_0^H V(x,y,z')dz'\right)\right] \qquad (35)$$

where $F^H_{POA}(h,k)$ is the diffracted wave, h and k are Miller indices, $\mathfrak{F}$ is the Fourier transform operator, σ $(= \frac{1}{\hbar v})$ is the interaction constant, and V(x,y,z) is the object potential. For large object thickness or strong object potential, the transmitted wave function, $\exp\left(-i\sigma\int_0^H V(x,y,z')dz'\right)$, oscillates very rapidly for a small change in (x,y). Extremely fine sampling intervals must be used in the Fourier integral. To use such an infinitesimal interval is not computationally practical. To overcome this difficulty the propagator function for crystal thickness H is expressed as n-times multiplication of the propagator function for a thin slice, c, which in this manuscript, is taken to be the crystal unit cell dimension in c-axis.

We can write then

$$\exp\left(-i\sigma\int_0^H V(x,y,z)dz\right) = \prod_{i=1}^{n} \exp\left(-i\sigma\int_0^C V(x,y,z')dz'\right)_i \qquad (36)$$

and $H = nc$.

The diffracted wave can then be represented by

$$F^H_{POA}(h,k) = \underbrace{Q(h,k) * Q(h,k) * Q(h,k) * \ldots * Q(h,k)}_{n \text{ time convolutions}} \qquad (37)$$

and

$$Q(h,k) = \mathcal{F}\left[\exp\left(-i\sigma\int_0^C V(x,y,z')dz'\right)\right]$$

where $Q(h,k)$ is the diffracted wave for a thin crystal of thickness c, and $*$ denotes convolution.

Theoretically, the convolution has to be done over all possible diffracted beams. However, the number of diffracted beams is still infinite even after the reduction due to the symmetry of the crystal. Such a computational operation is impractical if not impossible. For practical purposes, the convolution was done in our calculation with the limited number of diffracted beams. To ensure that a sufficient number of beams has been included in the computation, the diffracted beams calculated must approximately fulfill the following unitarity test (Moodie, A. F., 1965).

$$\sum_{h',k'} Q^{+}(h',k')\, Q(h-h', k-k') = \begin{cases} 1 & \text{when } h = k = 0 \\ 0 & \text{otherwise} \end{cases} \qquad (38)$$

and

$$Q^{+}(h,k) = \mathcal{F}\left[\exp\left(i\sigma \int_{0}^{C} V(x,y,z')dz'\right)\right]$$

This unitarity test can indicate whether a sufficient number of beams has been included in the computation. If an insufficient number of beams are used, the large angle diffracted beams which are neglected in the convolution operation would rapidly absorb the total beam intensity as the number of convolution operations in the calculation for the diffracted beams increases, or, in other words, as the crystal thickness increases. In the calculation of the diffracted waves, the number of beams used in the convolution operation is 355 for the case of cytosine and 543 for 'DISOPS'. Inclusion of these numbers of beams means that the electrons, which are scattered at an angle corresponding to frequencies greater than 0.95 $Å^{-1}$, are neglected. With these numbers of beams used, only a small percentage of the total beam intensity is absorbed by the neglected, high frequency diffracted beams. For example, at 100 keV, the unitarity test for a single slice thickness gives 0.03% and 0.02% error, respectively, for cytosine and 'DISOPS' crystals. The total beam intensity, after passing through a 500 Å thick crystal, reduces to 92% of the total beam intensity for both cytosine and 'DISOPS' crystal. The error in the unitarity test as well as the absorption effect decreases as the electron energy increases.

It is worth noting that Lynch (1973) has recently proposed an alternative method for evaluating the scattered wave function for the phase object approximation for the case of thin specimen. This evaluation is made directly from the projected potential, without evaluating the

scattered wave function for each sampling point. The proposed method employed the following equation

$$\exp\left(i\sigma\int V(x,y,z')dz'\right) = \lim_{s\to\infty}\left[1 + \frac{i\sigma}{s}\int V(x,y,z')dz'\right]^s \qquad (39)$$

In comparison with the conventional method, the new method has its advantages together with its disadvantages. As pointed out by Lynch, the new method requires less amount of computer storage, but loses the physical insight attained from the intermediate steps in the conventional method of the calculation.

(c) Multislice Dynamical Approximation

In the multislice dynamical approximation, the diffracted waves for crystals limited by parallel plane surfaces can be described by the following equation

$$F_m(h,k) = {}_n\Big[Q_n(h,k) * \ldots {}_2\Big[Q_2(h,k) * {}_1\Big[Q_1(h,k)\cdot P_1(h,k)\Big] \cdot P_2(h,k)\Big]_2 \ldots P_n(h,k)\Big]_n^{\dagger}$$

$$Q_i(h,k) = \mathfrak{F}\left[\exp\left(-i\sigma\int_{Z_{i-1}}^{Z_i} V(x,y,z')dz'\right)\right] \qquad (40)$$

and

$$P_i(h,k) = \exp\left[i\pi\lambda\,\Delta Z_i(h^2+k^2)\right]$$

---

†Within a given bracket, the operation should be performed from left to right.

where $F_m(h,k)$ is the diffracted wave in the multislice dynamical approximation. $P_i(h,k)$ is the Fresnel propagator for the i^{th} slice, $Q_i(h,k)$ is the i^{th} slice diffracted wave in the phase object approximation, ΔZ_i is the thickness of the i^{th} slice and all other notations have been defined previously. The numerical computation for these diffracted waves is similar to the one for the phase object approximation. The difference is only an additional "gaussian function" or Fresnel propagator: in the multislice dynamical approximation, the diffracted waves emerging from each slice are those of the phase object approximation but multiplied by a "gaussian function". The computation therefore takes approximately the same computing time for these two approximations.

2. A Validity Measure for the Diffracted Beam Intensities

A quantitative measure of the validity of the diffracted beam intensities calculated by either the kinematic approximation or the phase object approximation can be obtained by computing the deviation of these diffracted beam intensities from the 'exact' diffracted beam intensities calculated by the multislice formulation. One can then calculate, for either the phase object approximation or the kinematic approximation, the fraction of diffracted beams whose intensities deviate from the corresponding 'exact' intensities by less than a specified percentage error. This percentage agreement is calculated as a function of crystal thickness. It can give some validity measure of the approximations. This measure of validity, D(H), can be described by

$$D(H) = \frac{\Delta n(H)}{N} \cdot 100\% \qquad (41)$$

where H is the crystal thickness. $\Delta n(H)$ is, at a given crystal thickness, the number of the diffracted beam intensities which deviate, within a given percentage error, from the corresponding 'exact' diffracted beam intensities calculated by the multislice formulation. N is the total number of beams used in the computation of the diffracted waves by the multislice formulation.

3. The Projected Potential Retrieved by the Phase Object Approximation

In the phase object approximation, the retrieved projected potential is related to the transmitted wave function as

$$V^R(x,y) = \frac{hv}{2\pi H}\left(\tan^{-1}\left(\frac{Q^{im}(x,y)}{Q^R(x,y)}\right) \pm n\pi\right) \qquad (42)$$

$$n = 0,1,2,3, \ldots.$$

where $V^R(x,y)$ is the projected potential retrieved, h is Planck's constant, v is the electron velocity, H is the crystal thickness, and $Q^R(x,y)$, $Q^{im}(x,y)$ are, respectively, the real and imaginary part of the transmitted wave function.

For a given transmitted wave function, the projected potential retrieved by the phase object approximation has, at each point (x,y), multiple values. Infinite choices of projected potentials having the same value of the transmitted wave function at this point can therefore be obtained. The true projected potential which possesses this value can often be retrieved if the continuity property of the projected potential is imposed. There is still an infinite number of the true projected potential having the same

transmitted wave function since the projected potential, which differs by a constant value $2\pi h/\sigma H$, will only change the scattered wave function by a constant phase; and such a constant phase factor cannot be determined from the experimental data. However, a unique projected potential can be obtained if the crystal thickness as well as the average projected potential of a unit cell are known parameters. In any event, to retrieve the projected potential of a thick crystal requires, in general, a lengthy and complicated computer program. For a thin organic crystal of less than 100 Å, and for electron voltage of 100 keV, the exponent in the phase object approximation is less than -2π, when the resolution of the projected potential is less than 1 Å. Under these circumstances the projected potential can be easily obtained. Figure 14 shows the retrieved projected potentials for thin crystals.

4. The Dissimilarity Factor for the Retrieved Projected Potential

As already outlined in Section III.B.3, the phase object approximation can be used, in principle, to obtain the projected potential from the scattered wave function, which can theoretically be extracted from the experimental data. Whether this retrieved projected potential is a valid representation of the true projected potential depends on the validity of the phase object approximation. To evaluate the validity of the phase object approximation, a measure of the validity of the retrieved projected potential is needed. That is to say, a measure which can relate quantitatively between the true projected potential and the one retrieved is required in order to determine the validity of the phase object approximation.

Although the reliability factor commonly used in x-ray crystallography can be employed to give a validity measure for the retrieved projected

potential, such a measure is, however, insensitive to structural changes that contribute only to the phase of the Fourier spectrum of the projected potential. Instead of the conventional reliability factor, we use the dissimilarity factor that takes the phase into consideration. This dissimilarity factor can be written as

$$\mu(H,K) = \frac{\sum_{h,k}^{H,K} |F_c(h,k) - F_m(h,k)|^2}{\sum_{h,k}^{H,K} |F_c(h,k)|^2} \qquad (43)$$

where $\mu(H,K)$ is the dissimilarity factor as a function of resolution for the projected potential $V^R(x,y)$. (H,K) is the cut-off spatial frequency corresponding to the resolution which is desired for the dissimilarity test. $F_c(h,k)$ and $F_m(H,K)$ are, respectively, the Fourier spectrum of the true and retrieved projected potentials, and (h,k) represents the Miller indices. This type of dissimilarity factor has been proposed by others, as a measure of the dissimilarity for image analysis, to characterize the processes of the structural changes caused by radiation damage (Frank, J., 1974).

In the evaluation of the dissimilarity factor, the Fourier spectrum of the retrieved projected potential is not needed, instead the difference between this Fourier spectrum and that of the true projected potential is required. Within the validity domain of the phase object approximation, the retrieved projected potential can be expected to be similar to the true projected potential. The difference between these projected potentials can therefore be anticipated to be much smaller than the true projected potential itself. Within the validity domain of the phase object approx-

imation, computation shows that, at 100 keV, the difference between the true projected potential and that of the retrieved one is less than $\pi/\sigma H$. It should be noted that the validity of the phase object approximation, in terms of crystal thickness, is defined such that the dissimilarity factor is less than 0.05. For determination of the validity domain for the phase object approximation, there is no need, therefore, to write a lengthy program which is able to retrieve the projected potential of any given thickness.

The difference between the true and the retrieved projected potential can be calculated from the diffracted wave functions computed by the phase object approximation and those calculated by the multislice dynamical approximation. Both the true and retrieved projected potential bear the same form of relationship with the diffracted wave functions as

$$\begin{aligned} \mathfrak{F}[\exp\, i\sigma V^{R}(x,y)\,] &= F_{m}^{H}(h,k) \\ \mathfrak{F}[\exp\, i\sigma V(x,y)\,] &= F_{POA}^{H}(h,k) \end{aligned} \tag{44}$$

where $V(x,y)$ and $V^{R}(x,y)$ are, respectively, the true and the retrieved projected potential. $\mathfrak{F}$ is the Fourier transform operator, $F_{POA}^{H}(h,k)$ and $F_{m}^{H}(h,k)$ are, respectively, the diffracted wave function for a crystal of thickness H, in the phase object approximation and in the multislice dynamical approximation. The difference between the true and the retrieved projected potential can then be described as follows:

$$\left(V(x,y) - V^{R}(x,y)\right) = \frac{1}{\sigma}\tan\left(\frac{\Delta_{R}^{H}(x,y)}{\Delta_{im}^{H}(x,y)}\right); \quad \Delta^{H}(x,y) = \mathfrak{F}\left[F_{m}^{H}(h,k) * F_{POA}^{H}(-h,-k)\right] \tag{45}$$

where $\Delta^H_{im}(x,y)$ and $\Delta^H_R(x,y)$ are, respectively, the imaginary and real part of the complex function $\Delta^H(x,y)$. The asterisk sign, *, denotes the convolution. The Fourier spectrum of the deviation of the retrieved, from the true projected potential, can be obtained by taking the Fourier transform of equation (45).

The dissimilarity factor calculated from this Fourier spectrum is more accurate than that computed from both the Fourier spectrum of the retrieved projected potential and of the true projected potential. This is because the 'exact' diffracted wave was computed with a limited number of beams and with finite slice thickness. The 'exact' diffracted wave, calculated in such a way, is therefore inaccurate and introduces an error to the retrieved projected potential. The dissimilarity factor calculated from the retrieved projected potential is bound to carry this error. On the other hand, the error contributing to the dissimilarity factor can be expected to reduce when the dissimilarity factor is calculated from the diffracted wave functions computed by the multislice approximation and by the phase object approximation. Since the diffracted wave functions in both the multislice dynamical approximation and the phase object approximation were calculated in the same manner, or, in other words, since the same slice thickness and number of reflections were used, the error resulting from the inaccuracy of the 'exact' wave function is compensated by the similar, systematic inaccuracy of the diffracted wave in the phase object approximation.

C. Results and Discussion

The diffracted beam intensities as a function of crystal thickness were calculated by

1) the kinematic approximation,

2) the phase object approximation,

3) the multislice dynamical approximation.

The calculation was also done for various electron accelerating voltages in order to show the effect of electron energy on the validity domain of the kinematic approximation and of the phase object approximation. Figures 7a-d, and 8a-d show the typical feature of the diffracted beam intensities corresponding to the low and high frequency reflections. The calculation was done only for crystal thickness up to 500 Å.

The diffracted beam intensities computed by the multislice dynamical approximation can be used as the point of reference, for the validity measure of the intensities calculated by either the phase object approximation or the kinematic approximation. The reason is that the multislice dynamical approximation can be expected to be accurate especially when the calculation is done with a large number of reflections and with a very small slice thickness. Qualitative measure of the validity of the diffracted beam intensity can then be obtained by comparing the intensities calculated by either the phase object approximation or the kinematic approximation with the intensities computed by the multislice dynamical approximation.

1. The Validity of the Kinematic Approximation for the Calculation of the Diffracted Beam Intensity

Figures 7a-d, and 8a-d illustrate the diffracted beam intensities as a function of crystal thickness calculated by the kinematic approximation, phase object approximation and multislice dynamical approximation. These graphs indicate that the validity of the kinematic approximation extends, at 100 keV, to a crystal thickness of about 100 Å. At higher energies, the validity for the high frequency reflections increases to a larger crystal thickness, whereas for the low frequency reflections, it remains approximately the same.

A measure of validity for the diffracted beam intensities described by equation (41) was employed to obtain the validity measure of the diffracted beam intensities computed by the kinematic approximation. In calculating this equation, the exact diffracted beam intensities, used as the standard of reference, was computed by the multislice dynamical approximation. Figure 9a,b shows the results of this validity measure for various electron accelerating voltages. For a given voltage or a given graph, the various curves correspond to difference acceptable percentage errors used in the calculation. For example, the solid line corresponds to the case where the diffracted beam intensity in the kinematic approximation does not deviate more than 5% of the exact diffracted beam intensity in the multislice dynamical approximation. The graphs show that for a low acceptable percentage error, the validity of the kinematic approximation decreases very rapidly as crystal thickness increases. As electron energy increases from 100 keV to 1.0 MeV, this validity domain extends to a slightly larger crystal thickness. With further increase in electron energy it decreases

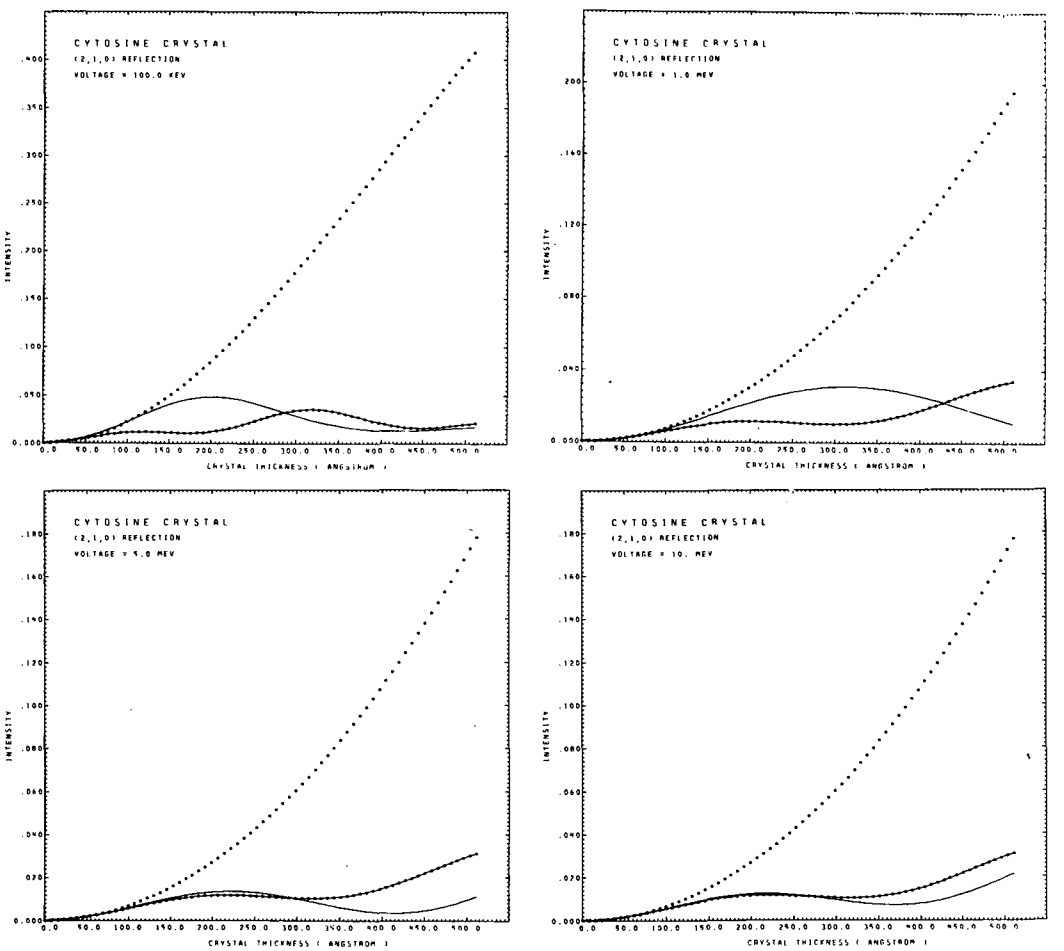

XBL 752-340

Fig. 7a. The diffracted beam intensities for the (2,1,0) reflection are plotted as a function of crystal thickness. Kinematic approximation (• • • • •), phase object approximation (•—•—•—•) and the multislice dynamical approximation (————). The crystal is cytosine and accelerating voltage is indicated on each graph.

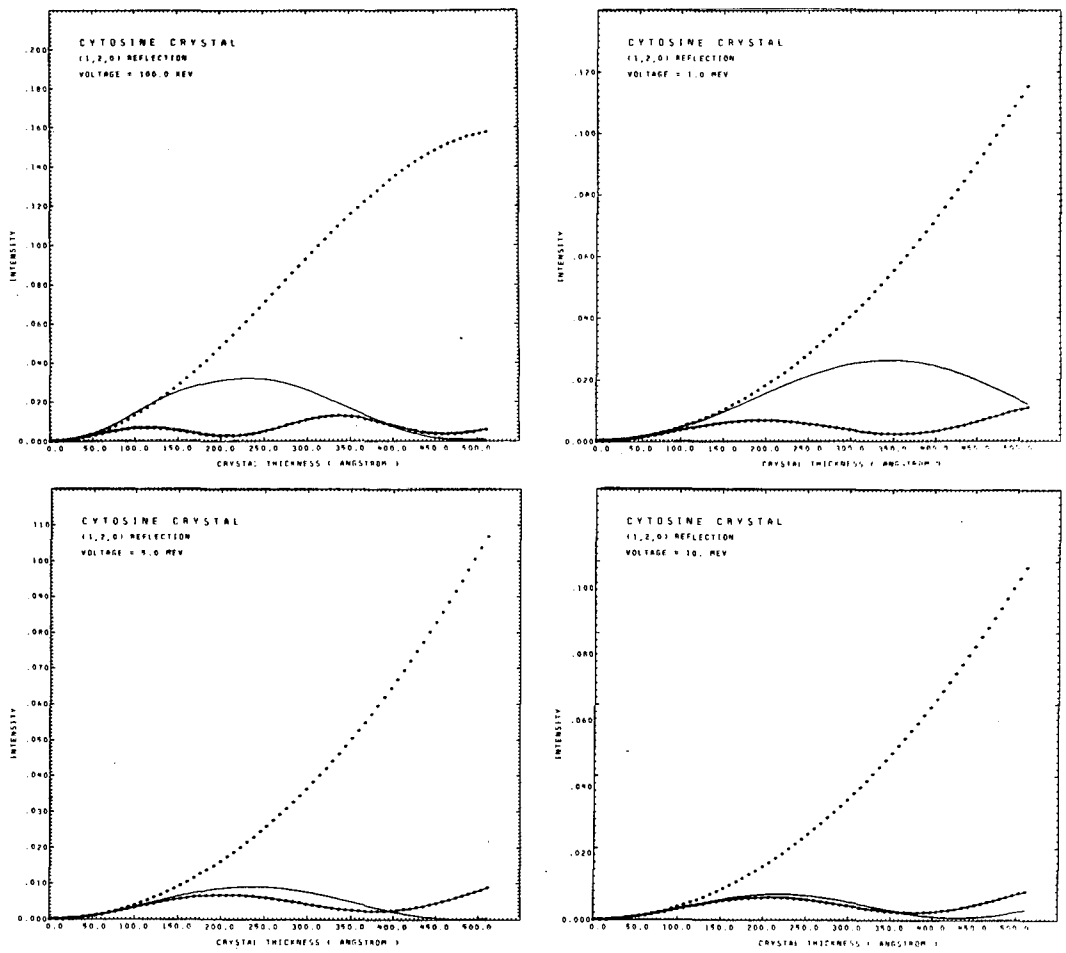

XBL 752-341

Fig. 7b. The diffracted beam intensities for the (1,2,0) reflection are plotted as a function of crystal thickness. Kinematic approximation (• • • • •), phase object approximation (•—•—•—•) and the multislice dynamical approximation (————). The crystal is cytosine and accelerating voltage is indicated on each graph.

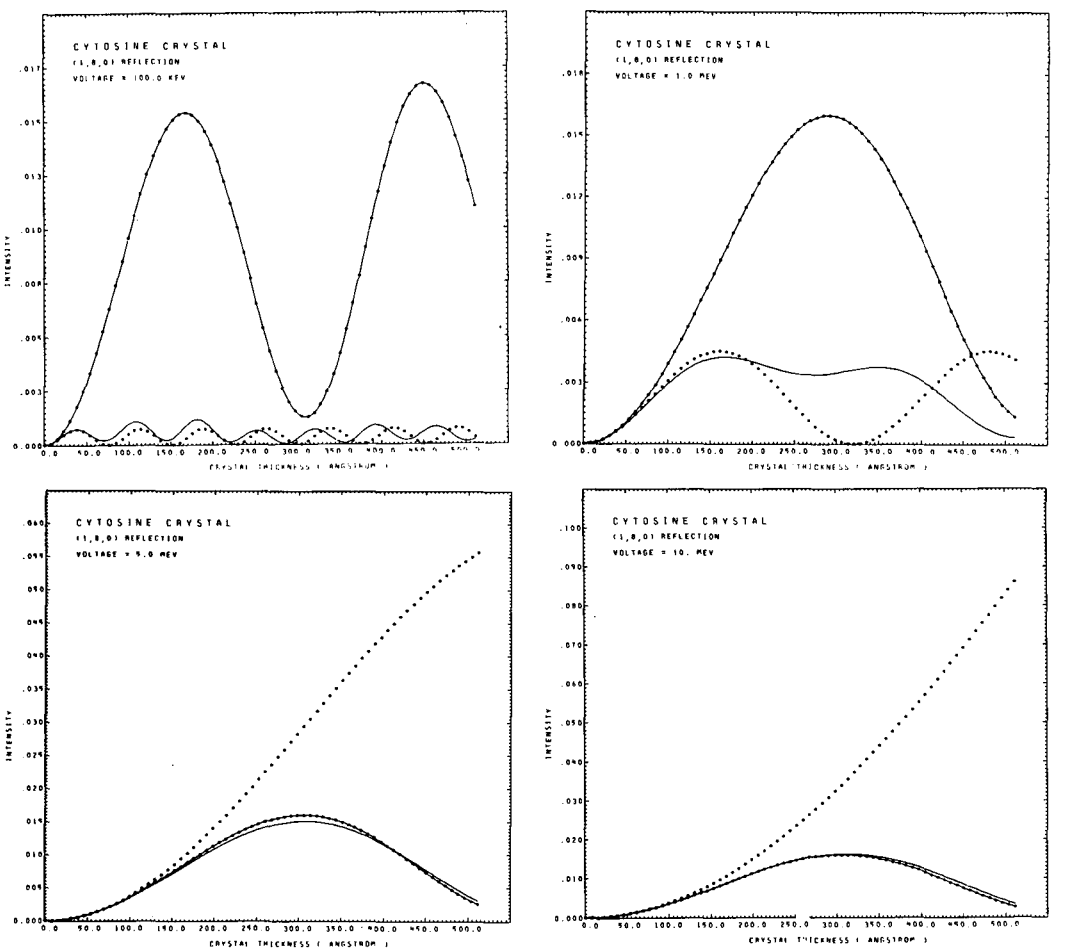

XBL 752-342

Fig. 7c. The diffracted beam intensities for the (1,8,0) reflection are plotted as a function of crystal thickness. Kinematic approximation (• • • • •), phase object approximation (•—•—•—•) and the multislice dynamical approximation (————). The crystal is cytosine and accelerating voltage is indicated on each graph.

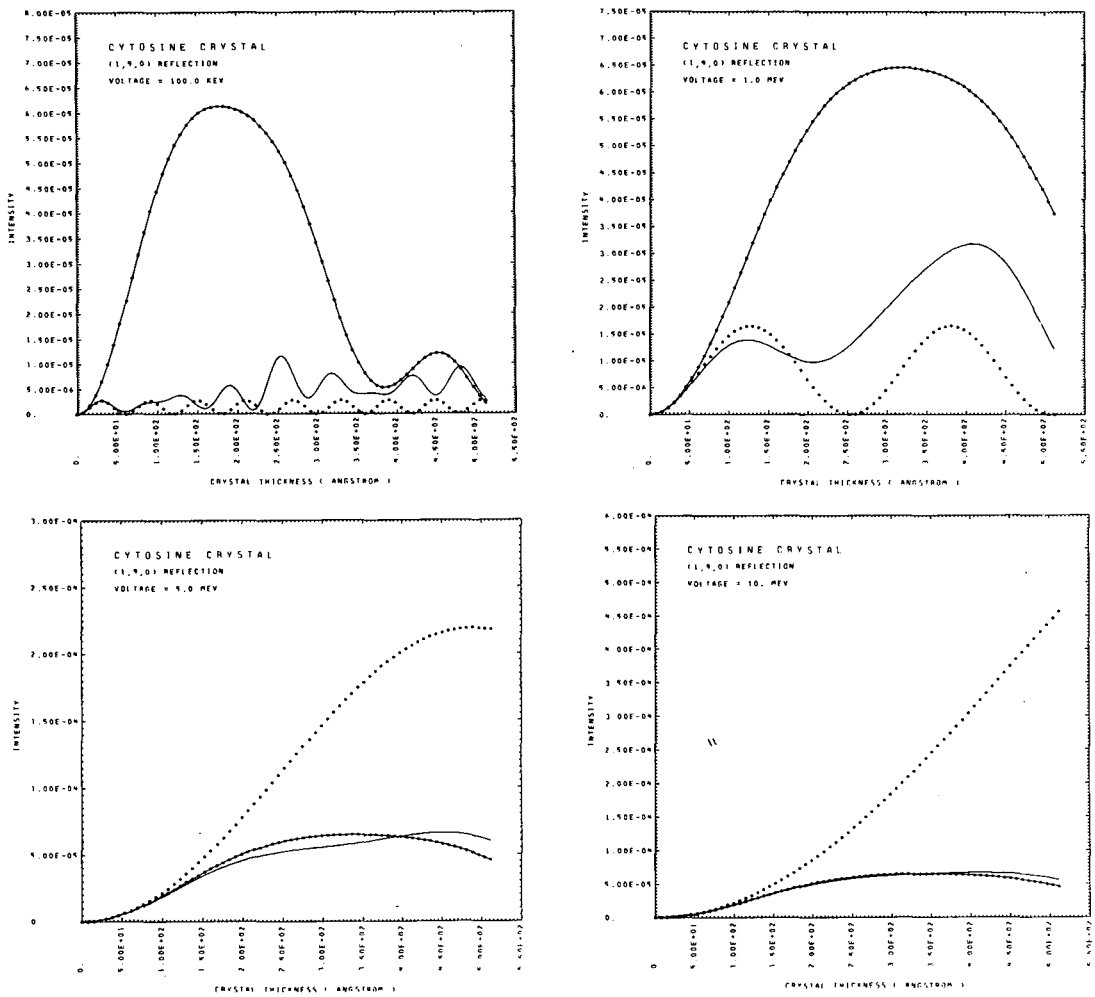

XBL 752-343

Fig. 7d. The diffracted beam intensities for the (1,9,0) reflection are plotted as a function of crystal thickness. Kinematic approximation (• • • • •), phase object approximation (•—•—•—•) and the multislice dynamical approximation (————). The crystal is cytosine and accelerating voltage is indicated on each graph.

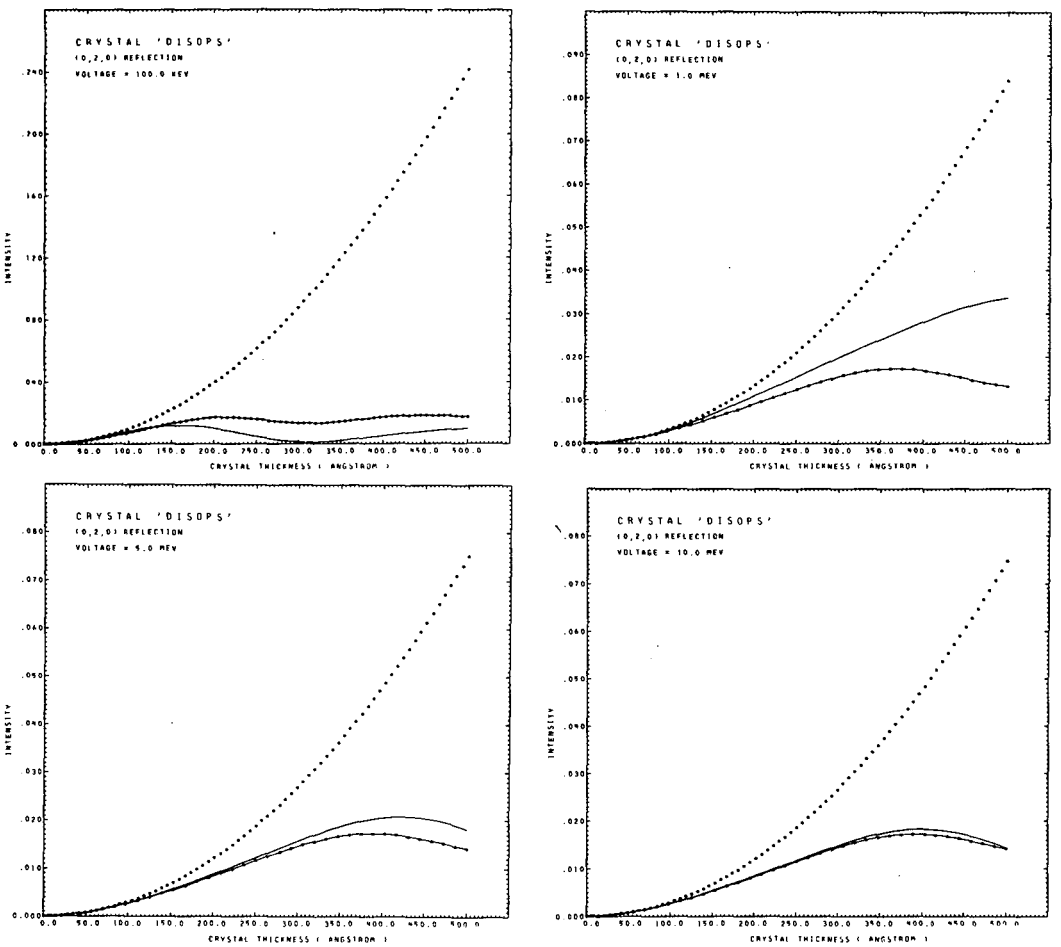

XBL 752-333

Fig. 8a. The diffracted beam intensities for the (0,2,0) reflection are plotted as a function of crystal thickness. Kinematic approximation (• • • • •), phase object approximation (•—•—•—•) and multislice dynamical approximation (————). The crystal is 'DISOPS' and accelerating voltage is indicated on each graph.

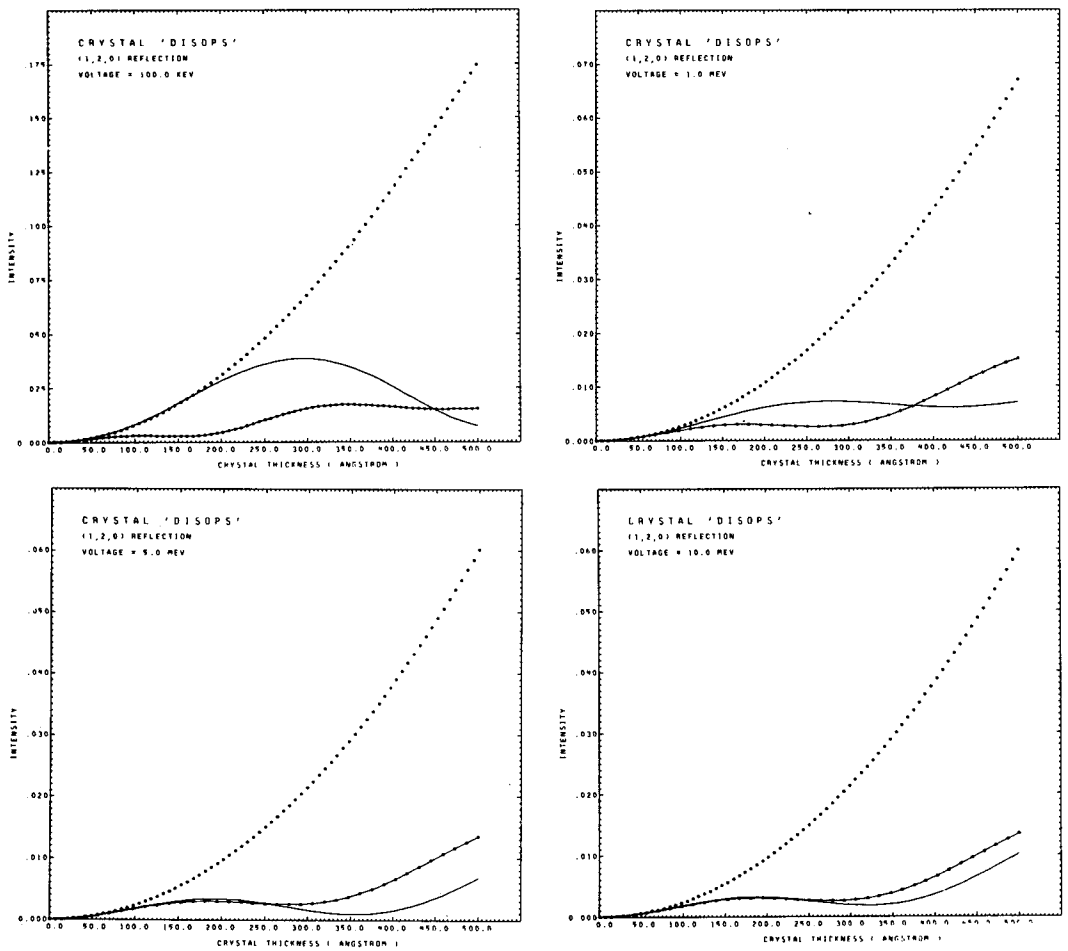

XBL 752-334

Fig. 8b. The diffracted beam intensities for the (1,2,0) reflection are plotted as a function of crystal thickness. Kinematic approximation (• • • • •), phase object approximation (•—•—•—•) and multislice dynamical approximation (————). The crystal is 'DISOPS' and accelerating voltage is indicated on each graph.

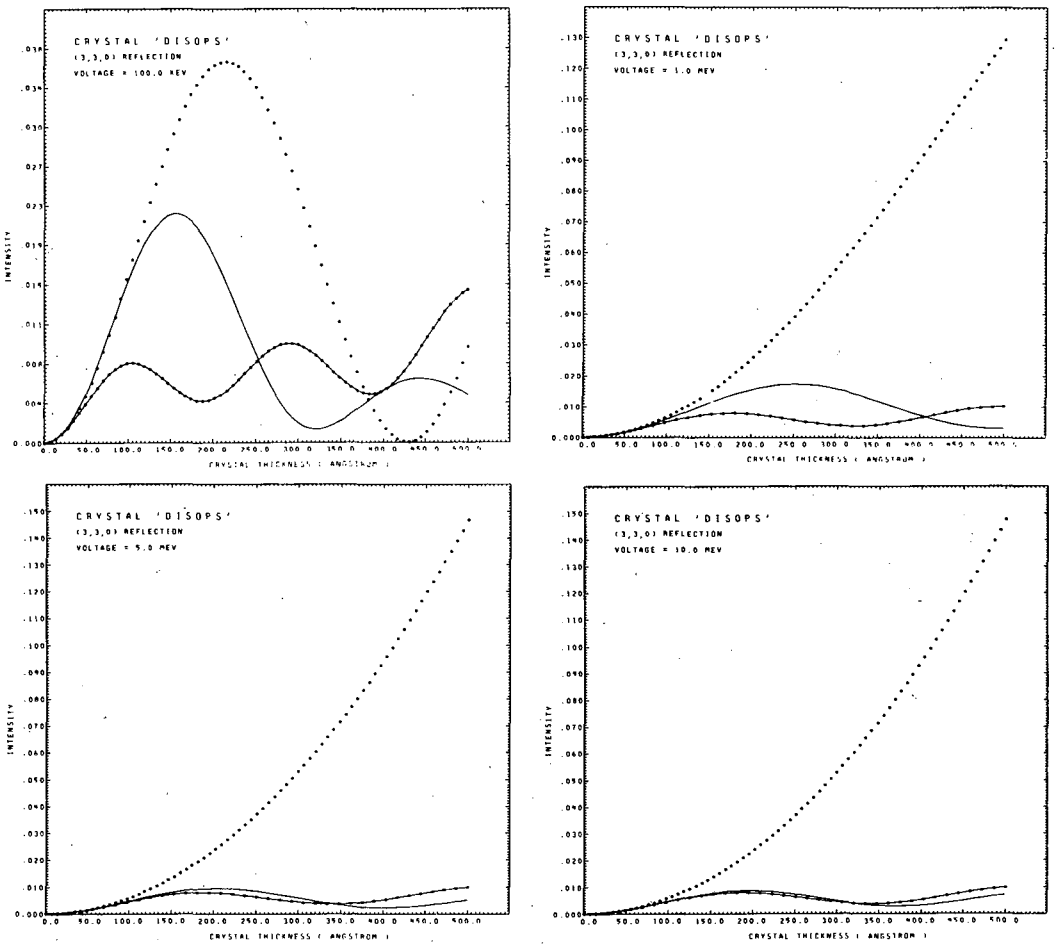

XBL 752-335

Fig. 8c. The diffracted beam intensities for the (3,3,0) reflection are plotted as a function of crystal thickness. Kinematic approximation (• • • • •), phase object approximation (•—•—•—•) and multislice dynamical approximation (————). The crystal is 'DISOPS' and accelerating voltage is indicated on each graph.

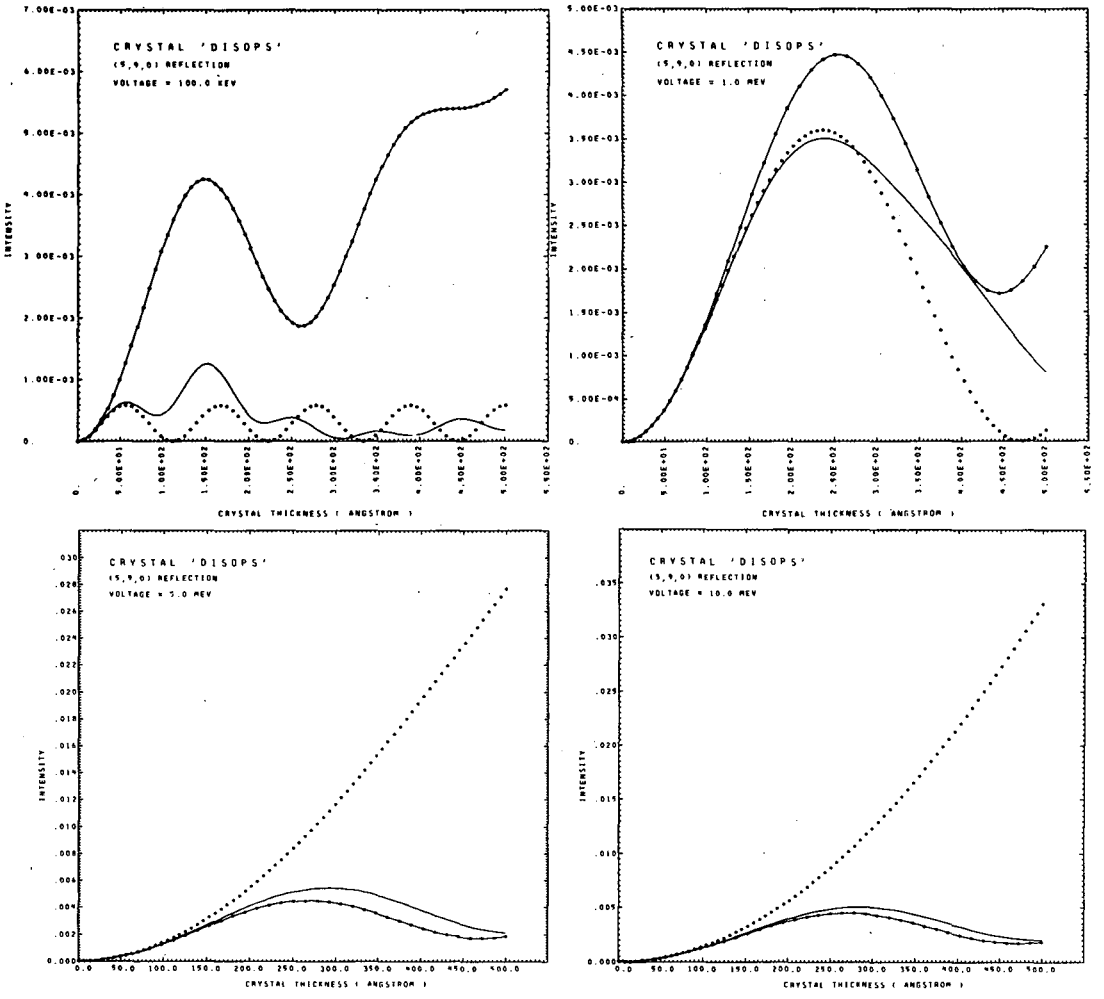

XBL 752-332

Fig. 8d. The diffracted beam intensities for the (5,9,0) reflection are plotted as a function of crystal thickness. Kinematic approximation (• • • • •), phase object approximation (• • • • • •) and multislice dynamical approximation (————). The crystal is 'DISOPS' and accelerating voltage is indicated on each graph.

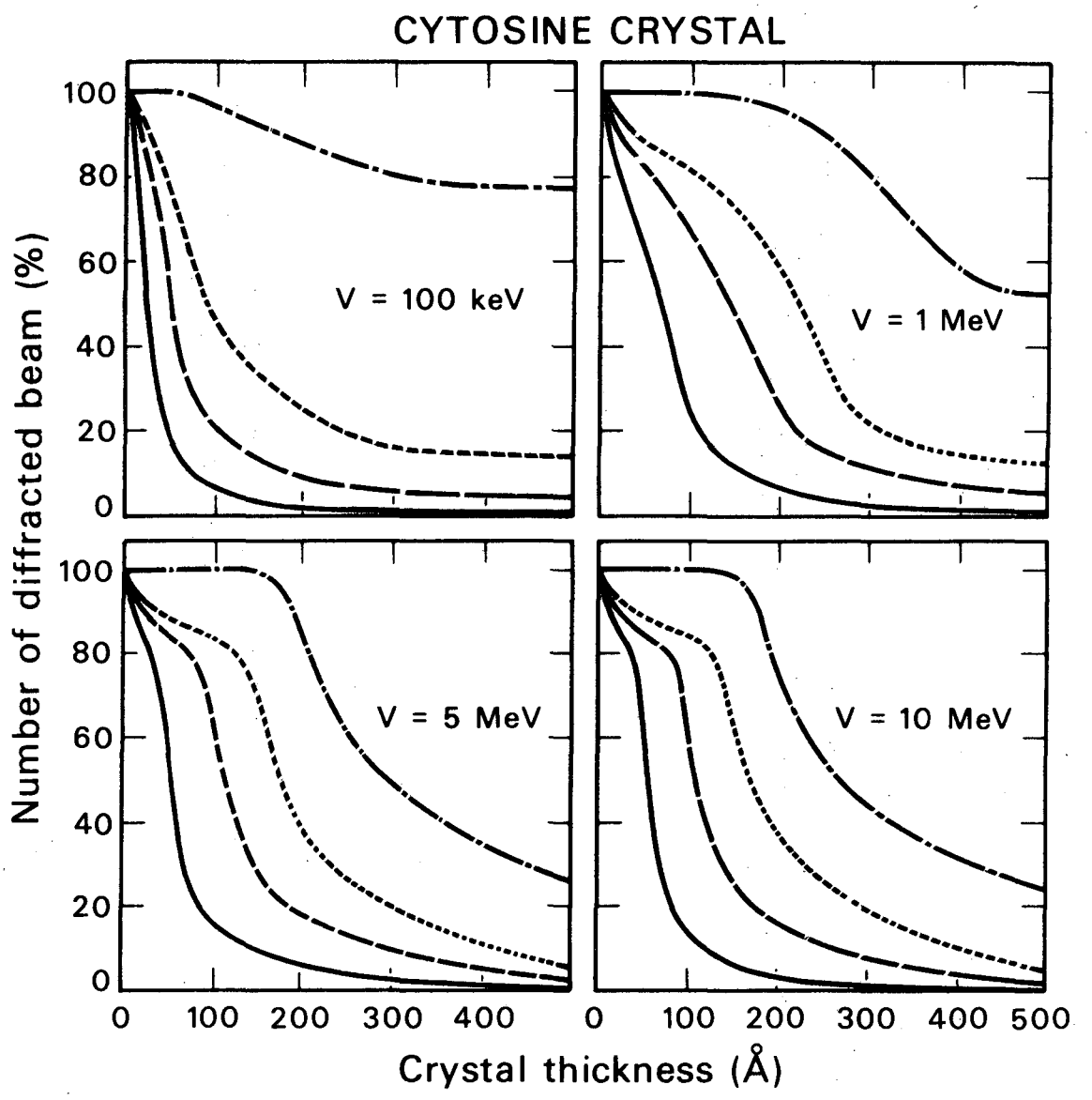

XBL 751-4654

Fig. 9a. The fraction of diffracted beams whose intensities in the kinematic approximation deviate less than a given percentage error from the exact diffracted beam intensities calculated by the multislice dynamical approximation, is plotted as a function of crystal thickness. The crystal is cytosine. The electron accelerating voltage used is indicated on each graph. (———) 5%, (— — — —) 20%, (------) 50%, and (— • — • — • —) 100%.

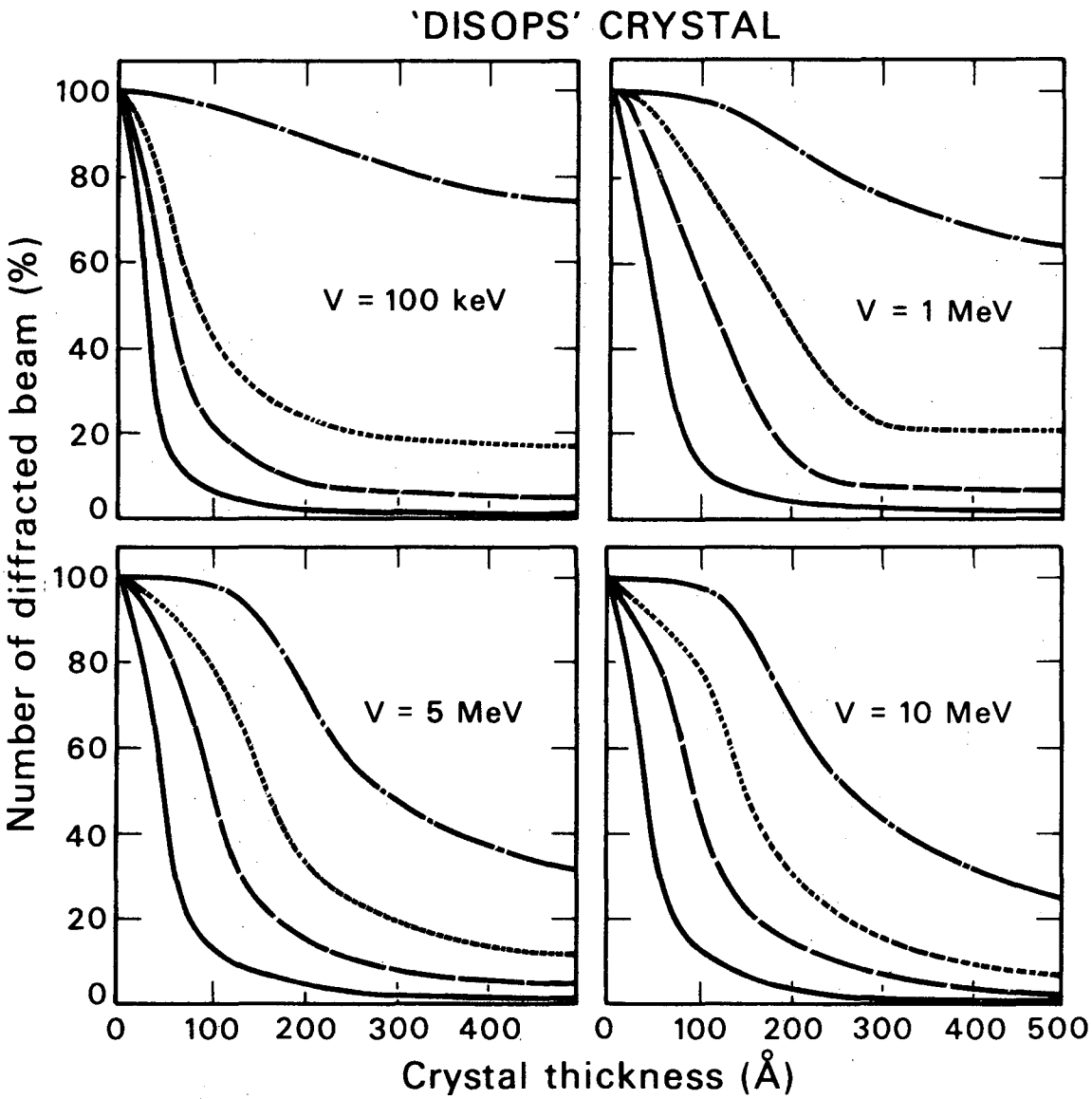

Fig. 9b. The fraction of diffracted beams whose intensities in the kinematic approximation deviate less than a given percentage error from the exact diffracted beam intensities calculated by the multislice dynamical approximation, is plotted as a function of crystal thickness. The crystal is 'DISOPS'. The electron accelerating voltage used is indicated on each graph. (———) 5%, (— — — —) 20%, (------) 50%, and (— • — • — • —) 100%.

to a small crystal thickness. The graphs also show that for a large acceptable percentage error, the validity domain of the kinematic approximation decreases with electron energy.

We can conclude that the validity domain of the kinematic approximation does not always increase with increasing electron energy. Although the cross section of the electron scattering decreases with increasing energy, the dynamical scattering effect may yet play an important role at high energy.

2. The Validity of the Phase Object Approximation for the Calculation of the Diffracted Beam Intensity

Figures 7a-d and 8a-d show qualitatively that at 100 keV the validity of the diffracted beam intensities in the phase object approximation is limited to a smaller crystal thickness than that in the kinematic approximation. As electron accelerating energy increases, the validity domain of the phase object approximation in terms of crystal thickness increases, and gradually surpasses the validity domain of the kinematic approximation. The graphs also show that as crystal thickness increases the validity of the phase object approximation is increasingly confined to a lower frequency reflection and as electron energy increases it extends to an increasingly higher frequency. This is expected since a given reflection is associated with a smaller scattering as electron energy increases and the phase object approximation is anticipated to be increasingly valid as the scattering angle becomes very small. The graphs further indicate that the diffracted beam intensities of the high frequency reflections in the phase object approximation are larger than the corresponding exact diffracted beam intensities computed by the multislice dynamical approximation.

A measure of validity of the diffracted beam intensity described by equation (41) and used for the case of the kinematic approximation was also applied to the case of the phase object approximation to obtain its validity domain. Figure 10a,b displays, for various acceptable percentage errors, the validity of the diffracted beam intensities in the phase object approximation as a function of crystal thickness at different electron accelerating voltages. These graphs indicate that the validity domain of the phase object approximation increases to a larger crystal thickness as electron energy increases. Compared to the kinematic approximation, the phase object approximation has at 100 keV, a smaller domain of validity. Already at 1.0 MeV, the validity domain of the phase object approximation exceeds, however, that of the kinematic approximation.

3. The Diffracted Wave

The phase of the diffracted waves may play an important role in the structural determination of the crystal. Experience in x-ray crystallography has indicated that a recognizable molecular structure can be obtained from the strongest 10% of the large number of diffracted beam amplitudes with correct phases (Stout, G. H. and Jensen, L. H., 1968). On the other hand, the amplitudes of only the complete diffracted beams give an infinite number of possible structures. Therefore it is clear, if one wants to determine the validity of any given approximation for the structural analysis, that the amplitudes together with the phases should be used in the evaluation of the validity.

The phases of the diffracted beams as a function of crystal thickness have been calculated for various electron accelerating voltages by the kinematic approximation, the phase object approximation and the

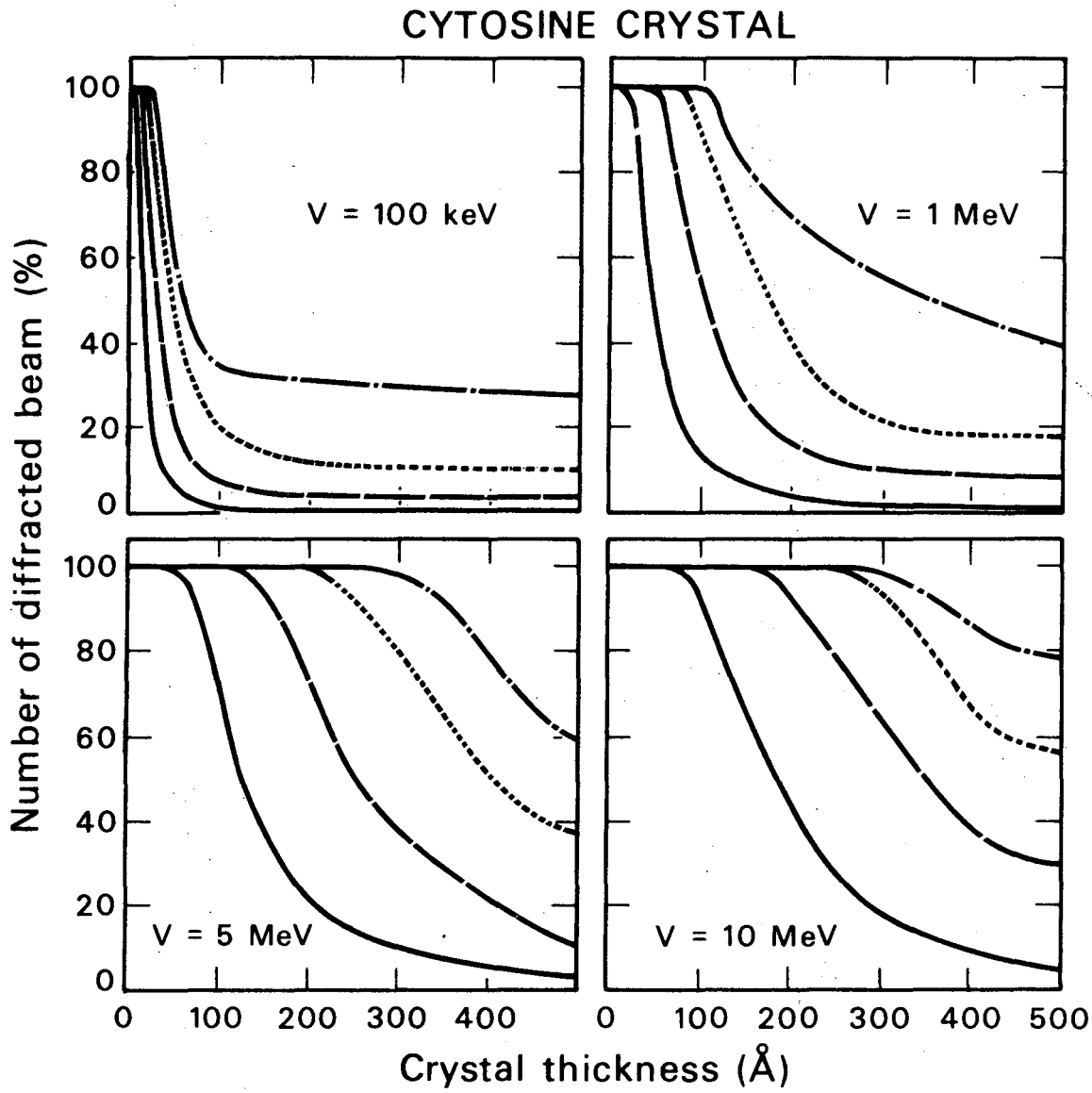

XBL 751-4653

Fig. 10a. The fraction of diffracted beams whose intensities in the phase object approximation deviate less than a given percentage error from the exact diffracted beam intensities calculated by the multislice dynamical approximation is plotted as a function of crystal thickness. The crystal is cytosine and the electron accelerating voltage used is indicated on each graph. (———) 5%, (— — — —) 20%, (-------) 50%, and (—•—•—•—) 100%.

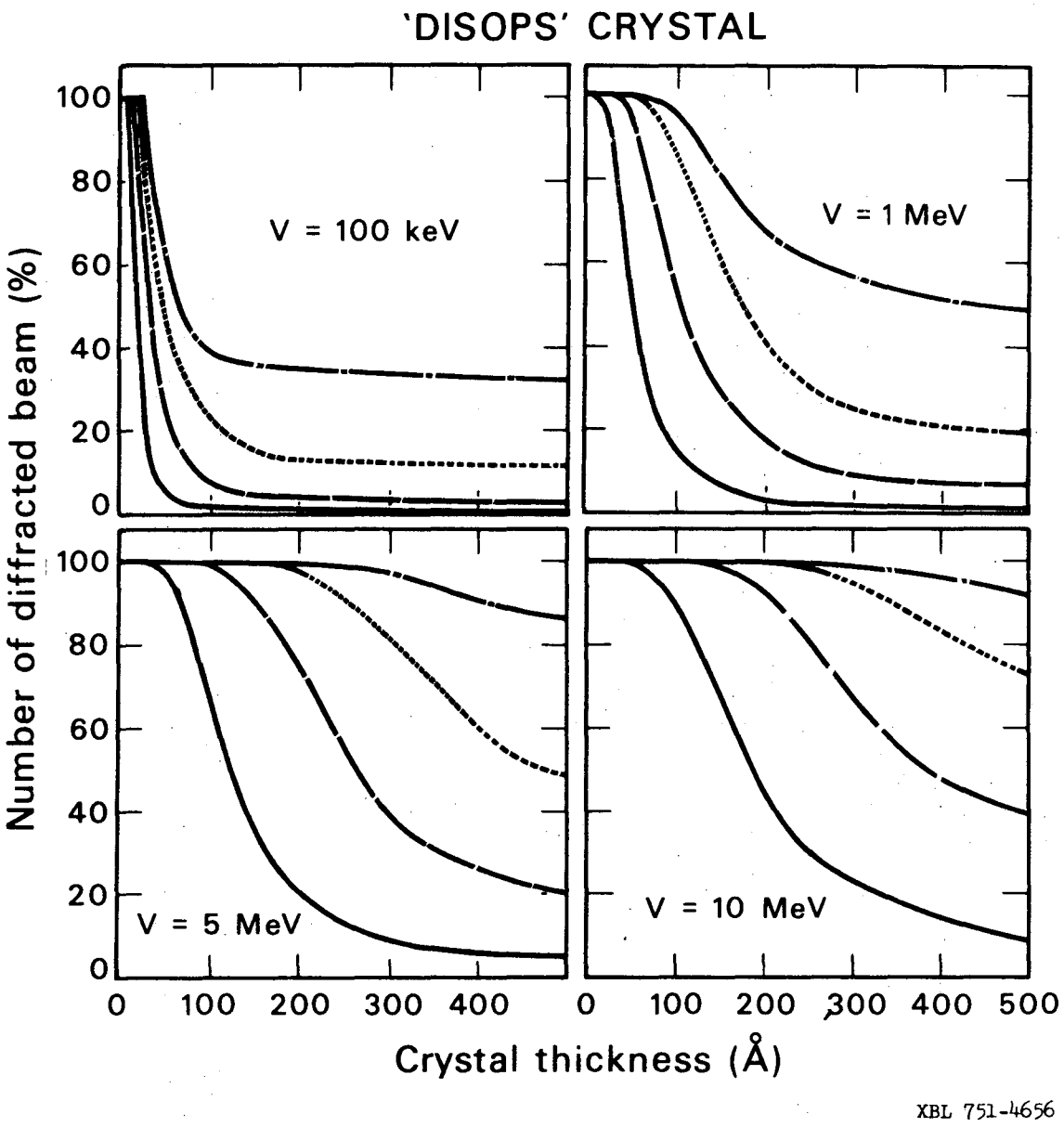

Fig. 10b. The fraction of diffracted beams whose intensities in the phase object approximation deviate less than a given percentage error from the exact diffracted beam intensities calculated by the multislice dynamical approximation is plotted as a function of crystal thickness. The crystal is 'DISOPS' and the electron accelerating voltage used is indicated on each graph. (———) 5%, (– – – –) 20%, (-------) 50%, and (—•—•—•—) 100%.

multislice dynamical approximation. Figures 11a-d and 12a-d display the phases of the low and high frequency reflections as a function of crystal thickness. The graphs show that, at 100 keV, the validity domain of the phases in the kinematic approximation is limited to a very small crystal thickness, whereas in the phase object approximation it extends to a greater crystal thickness. As electron energy increases, the validity domain in the kinematic approximation remains approximately the same while in the phase object approximation it increases to a larger crystal thickness.

The validity of the diffracted beam intensities evaluated in the previous section can be used to give a quantitative picture of the validity of the diffracted beam amplitudes. Compared to that in the kinematic approximation, the validity of the diffracted beam amplitude in the phase object approximation can be expected to possess at 100 keV, therefore, a slightly smaller domain. The validity of the diffracted beam amplitude in the phase object approximation can also be expected to increase with increasing electron accelerating voltage, whereas in the kinematic approximation, it increases only slightly as electron energy increases from 100 keV to 1.0 MeV. With further increase in electron energy, this validity domain in the kinematic approximation decreases to a small crystal thickness.

Qualitatively, we can conclude,

1) That the validity domain of the phase object approximation is larger than that of the kinematic approximation,
2) That the validity domain of the phase object approximation increases with increasing electron energy,

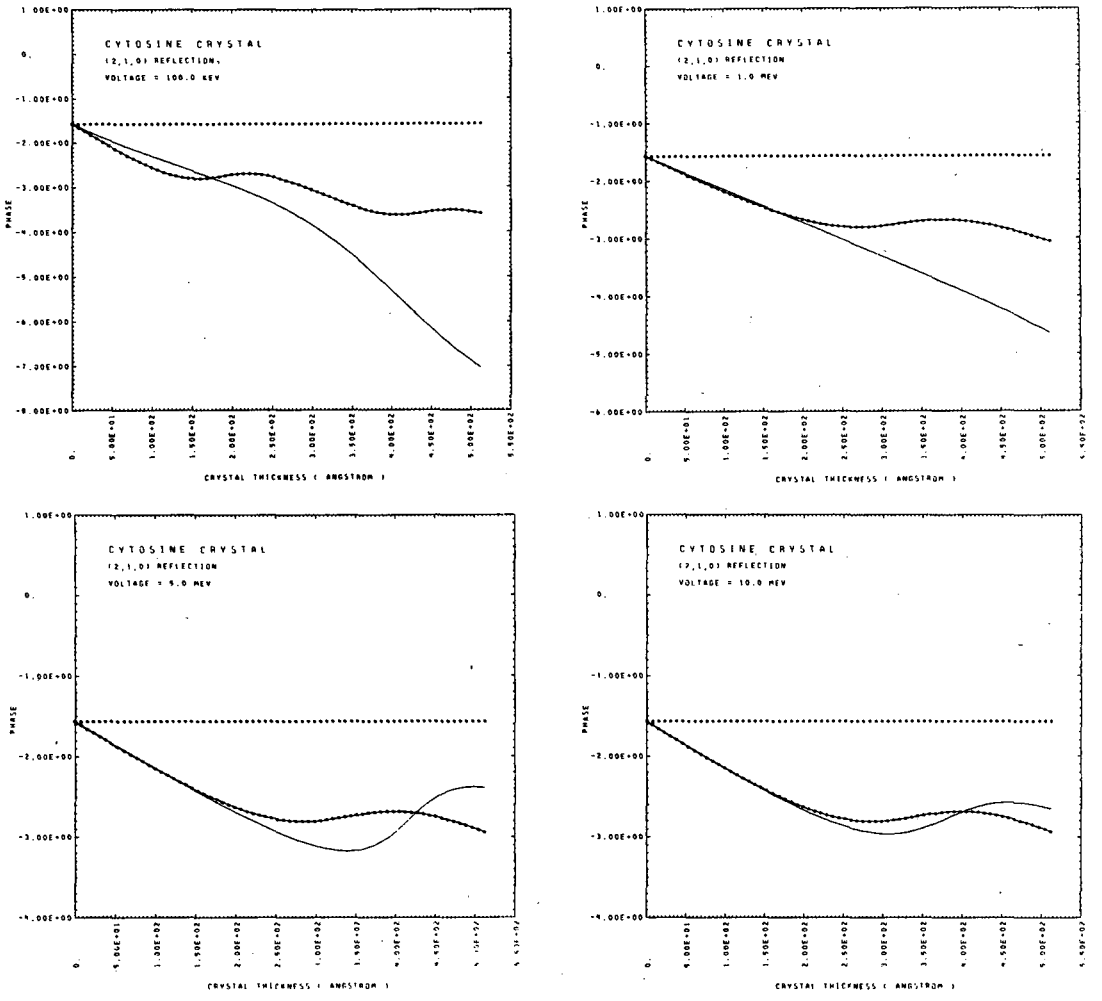

XBL 752-336

Fig. 11a. The phases of the diffracted beams for the (2,1,0) reflection are plotted as a function of crystal thickness. Kinematic approximation (••••••), phase object approximation (–•–•–•–) and multislice dynamical approximation (————). The crystal is cytosine. The electron accelerating voltage is indicated on each graph.

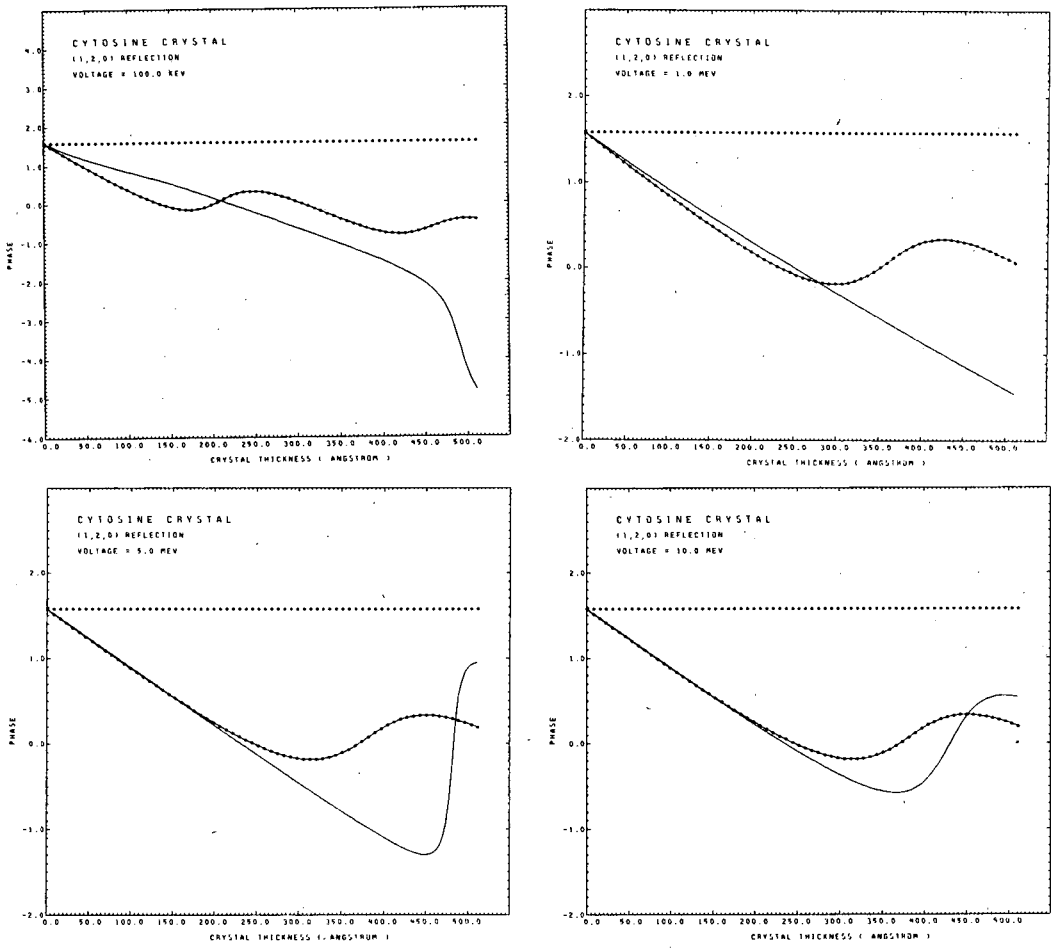

XBL 752-337

Fig. 11b. The phases of the diffracted beams for the (1,2,0) reflection are plotted as a function of crystal thickness. Kinematic approximation (••••••), phase object approximation (•••••••) and multislice dynamical approximation (———). The crystal is cytosine. The electron accelerating voltage is indicated on each graph.

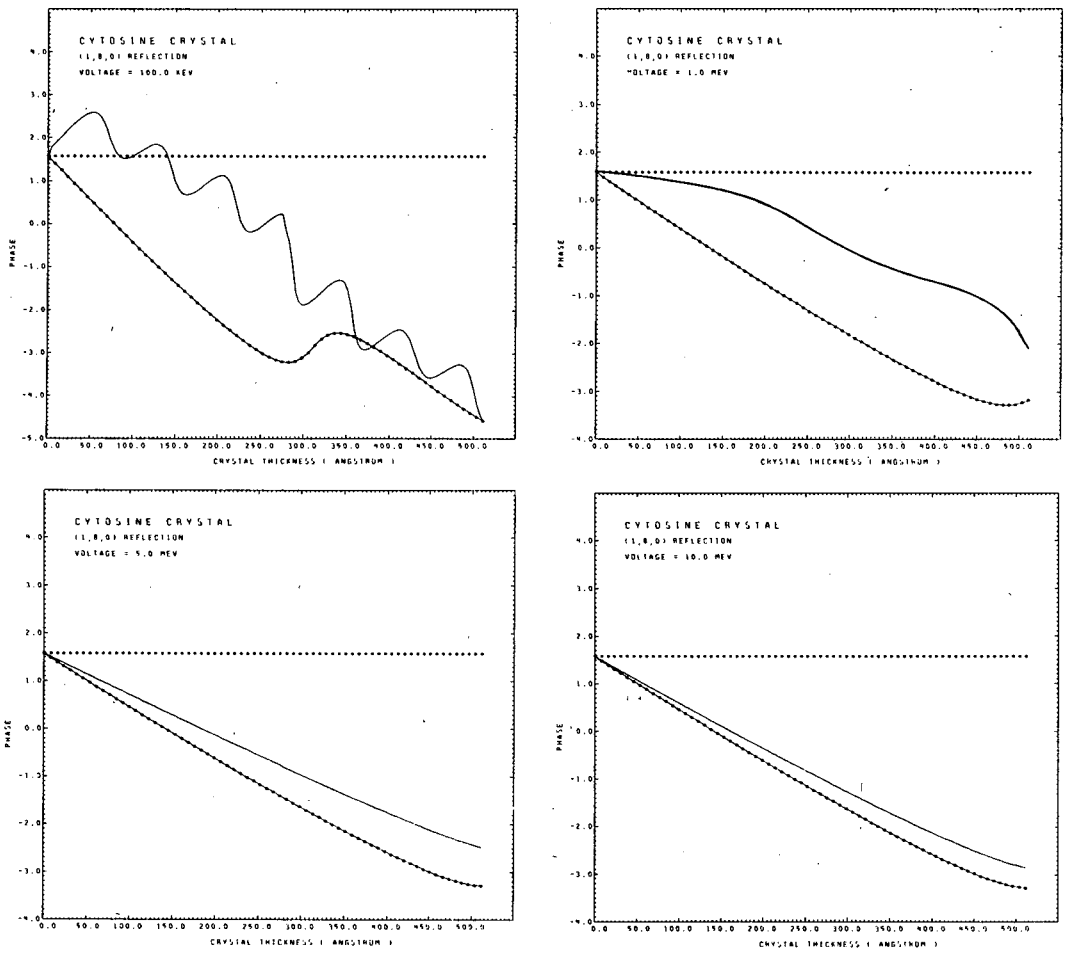

XBL 752-338

Fig. 11c. The phases of the diffracted beams for the (1,8,0) reflection are plotted as a function of crystal thickness. Kinematic approximation (••••••), phase object approximation (•-•-•-•-•) and multislice dynamical approximation (————). The crystal is cytosine. The electron accelerating voltage is indicated on each graph.

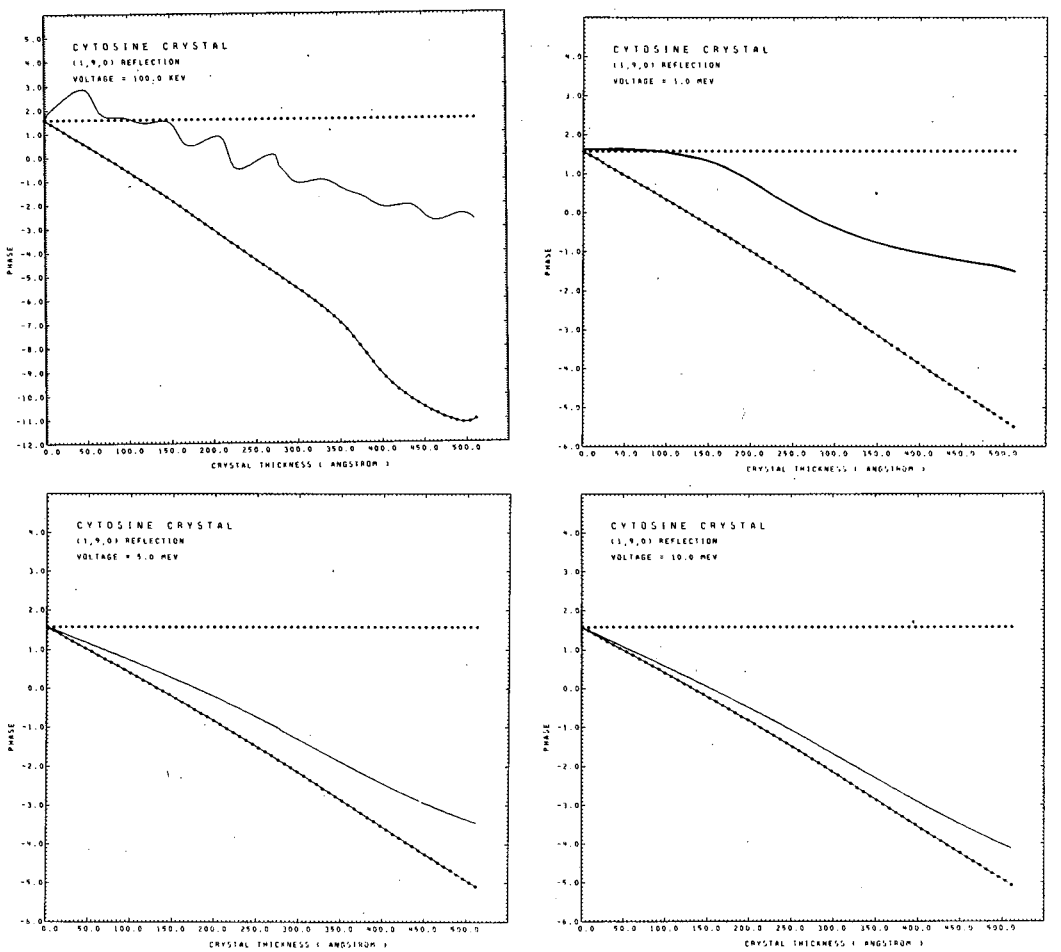

XBL 752-339

Fig. 11d. The phases of the diffracted beams for the (1,9,0) reflection are plotted as a function of crystal thickness. Kinematic approximation (••••••), phase object approximation (••••••••) and multislice dynamical approximation (————). The crystal is cytosine. The electron accelerating voltage is indicated on each graph.

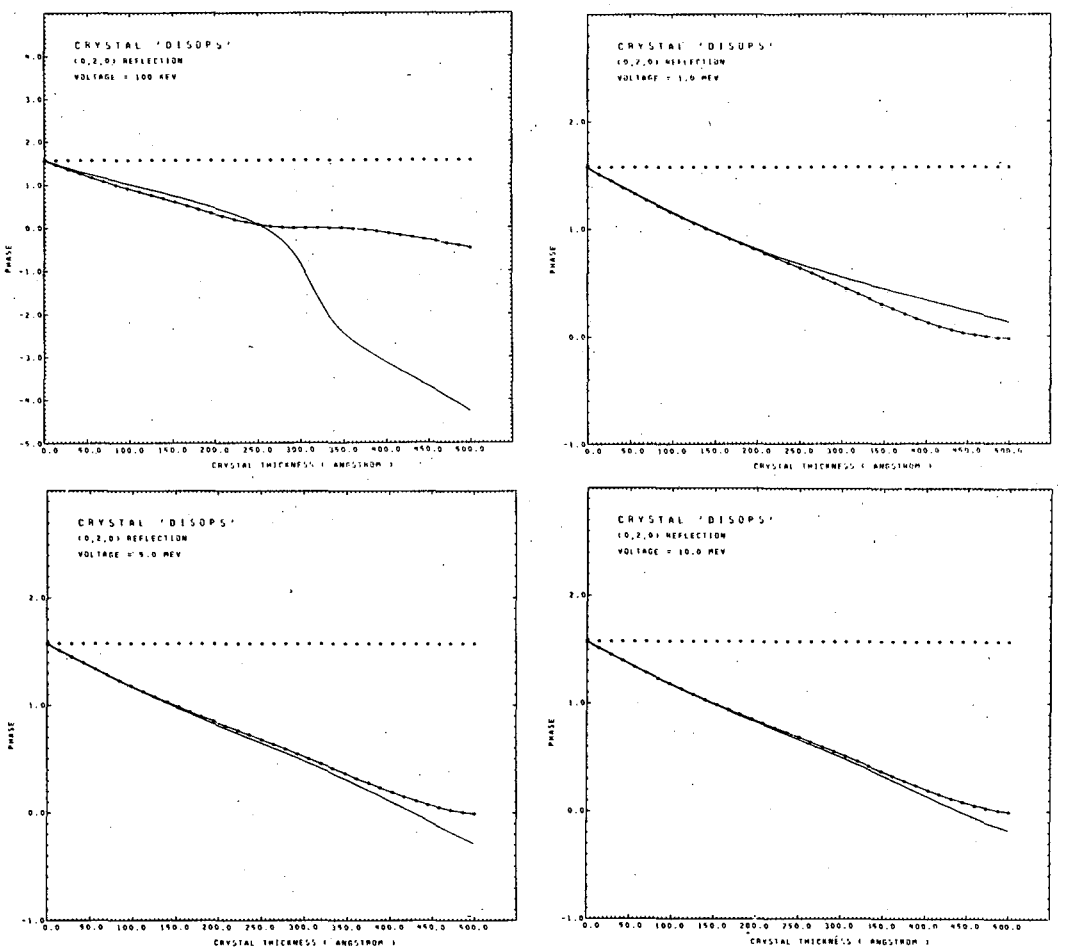

XBL 752-329

Fig. 12a. The phases of the diffracted beams for the (0,2,0) reflection are plotted as a function of crystal thickness. Kinematic approximation (·····), phase object approximation (·-·-·-·) and multislice dynamical approximation (————). The crystal is 'DISOPS'. The electron accelerating voltage is indicated on each graph.

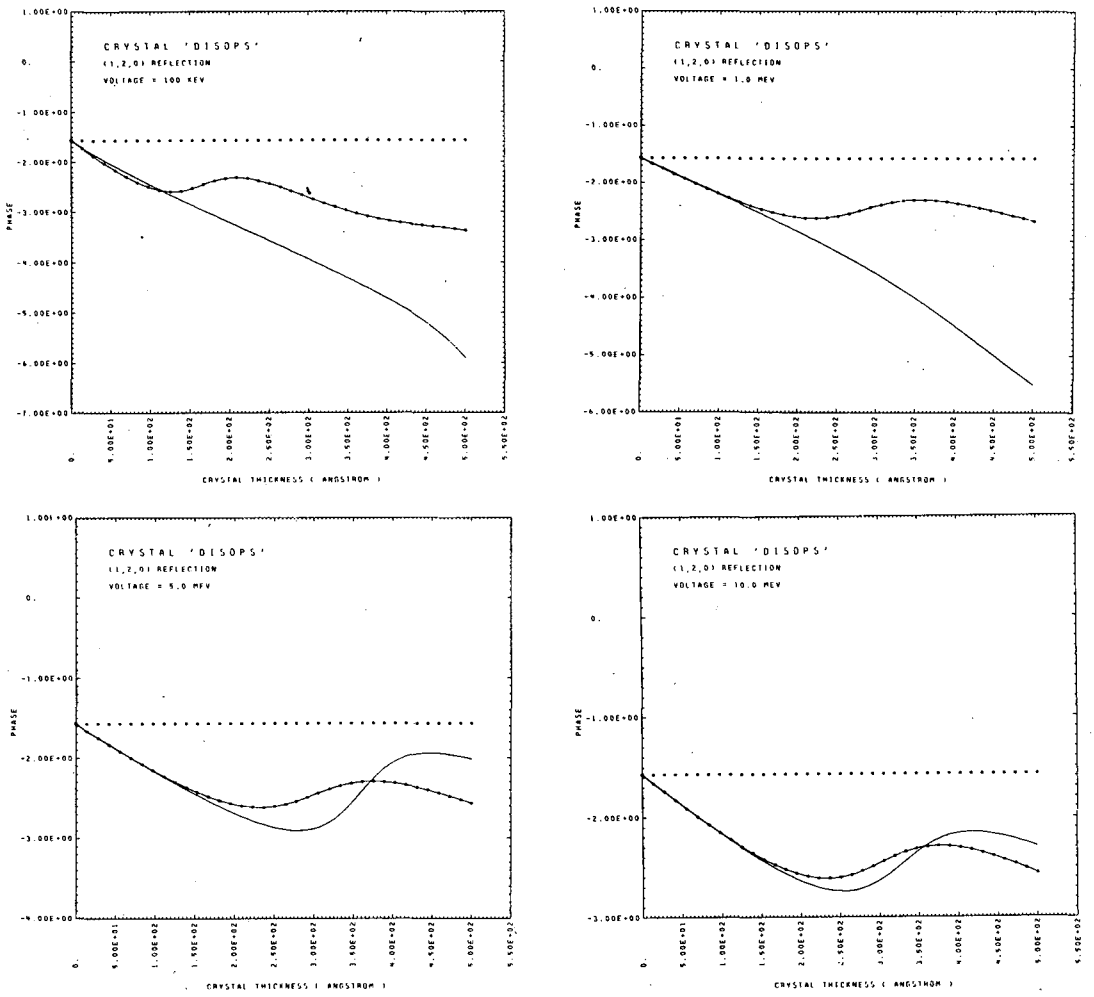

XBL 752-331

Fig. 12b. The phases of the diffracted beams for the (1,2,0) reflection are plotted as a function of crystal thickness. Kinematic approximation (•••••••), phase object approximation (–•–•–•–•–) and multislice dynamical approximation (————). The crystal is 'DISOPS'. The electron accelerating voltage is indicated on each graph.

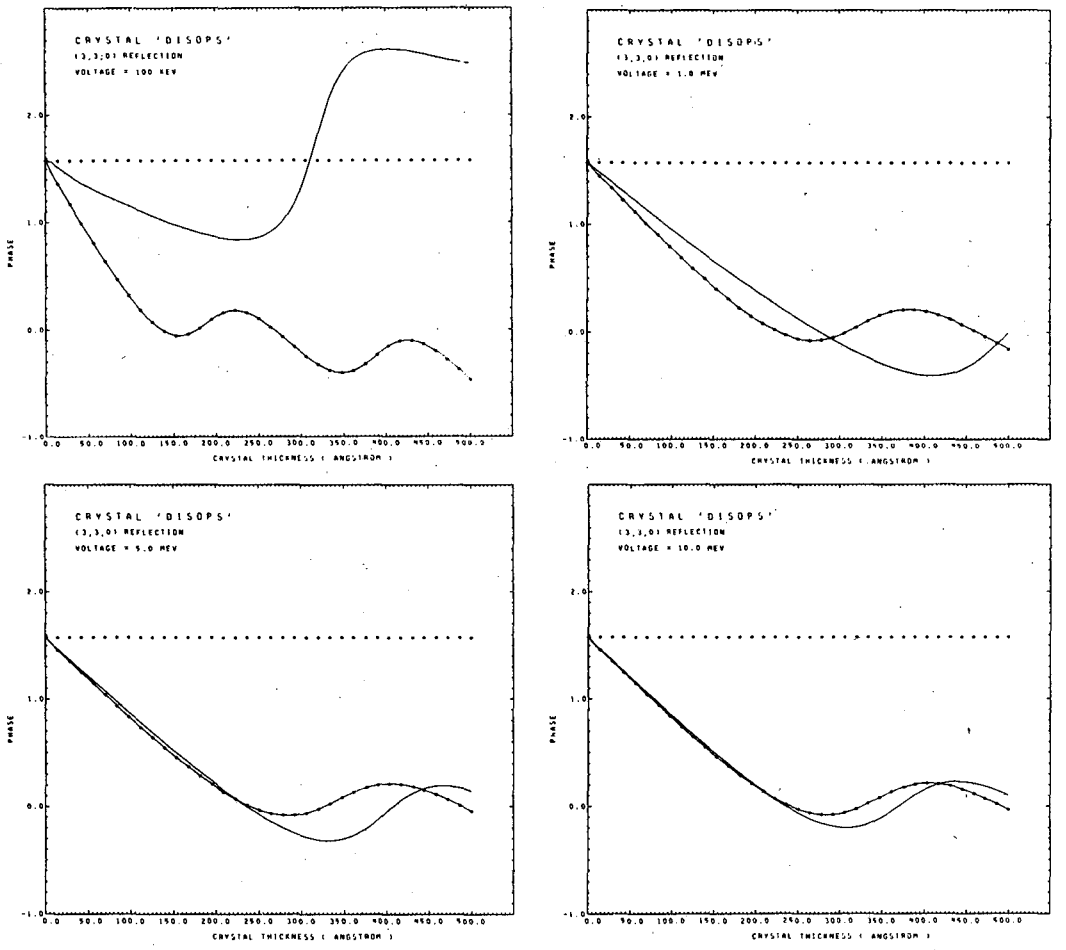

XBL 752-330

Fig. 12c. The phases of the diffracted beams for the (3,3,0) reflection are plotted as a function of crystal thickness. Kinematic approximation (•••••••), phase object approximation (-•-•-•-•) and multislice dynamical approximation (————). The crystal is 'DISOPS'. The electron accelerating voltage is indicated on each graph.

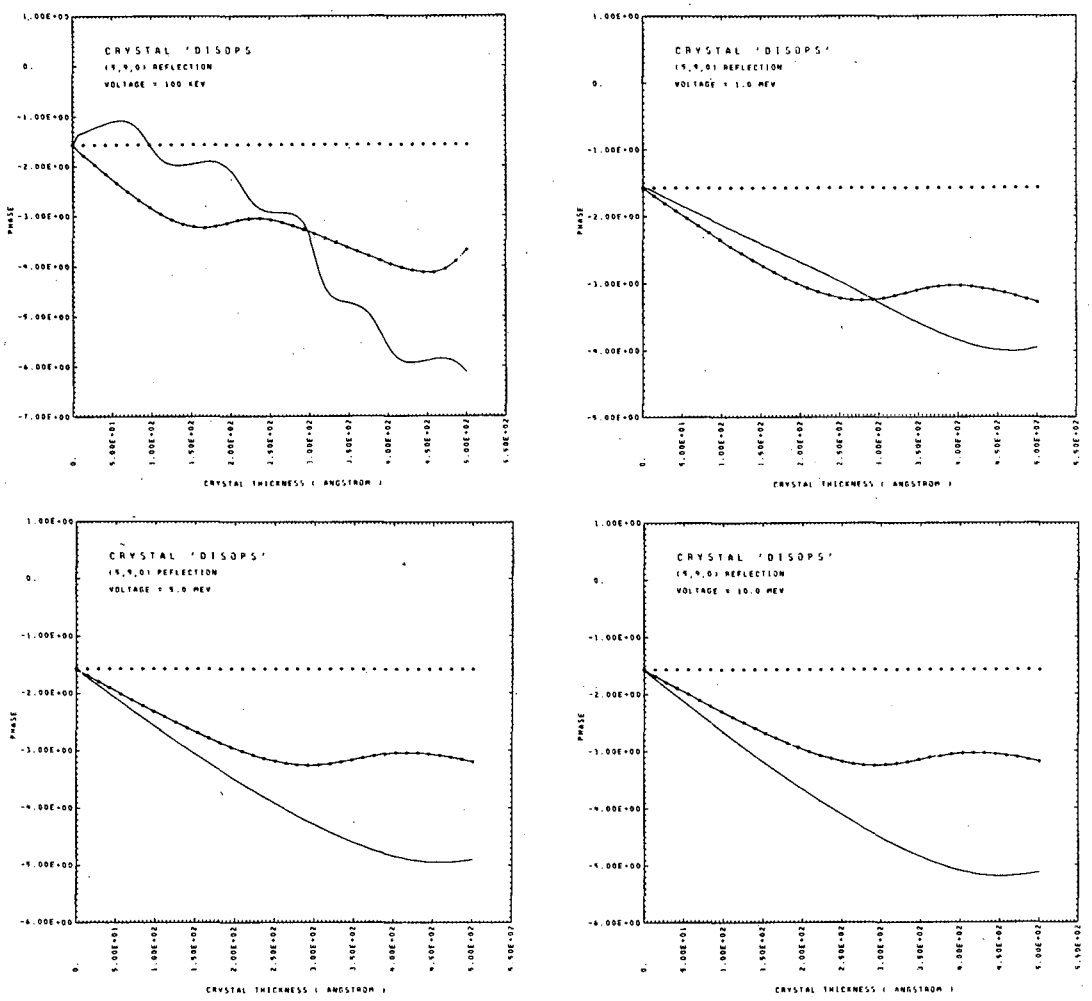

XBL 752-328

Fig. 12d. The phases of the diffracted beams for the (5,9,0) reflection are plotted as a function of crystal thickness. Kinematic approximation (·····), phase object approximation (-·-·-·-·) and multislice dynamical approximation (————). The crystal is 'DISOPS'. The electron accelerating voltage is indicated on each graph.

3) That the validity domain of the kinematic approximation increases slightly when electron energy increases from 100 keV to 1.0 MeV, but then decreases with further increases in electron accelerating voltage.

4. The Validity of the Phase Object Approximation for the Retrieval of the Projected Potential

The dissimilarity factor defined in Section III.B.4 can be used to give a measure of the validity of the phase object approximation. The validity of the diffracted wave in the dynamical approximations does not, however, relate linearly to the validity of the projected potential. This means that an acceptable value of the dissimilarity factor for the diffracted waves cannot always ensure the validity of the projected potential retrieved. It is therefore necessary to measure the validity of the phase object approximation on the basis of the projected potential, since, after all, our interest is to obtain the correct projected potential retrieved, not the scattered wave function.

The dissimilarity factor, as a function of spatial frequency, for the projected potential retrieved by the phase object approximation was evaluated as a function of crystal thickness and for various electron energies. Figure 13a-d shows the typical features of the dissimilarity factor as a function of spatial frequency. The graphs indicate that for a given crystal thickness the value of the dissimilarity factor of the phase object approximation increases as spatial frequency increases, whereas at high energies the value of the dissimilarity factor decreases with spatial frequency. As crystal thickness increases, on the other hand, the dissimilarity factor increases.

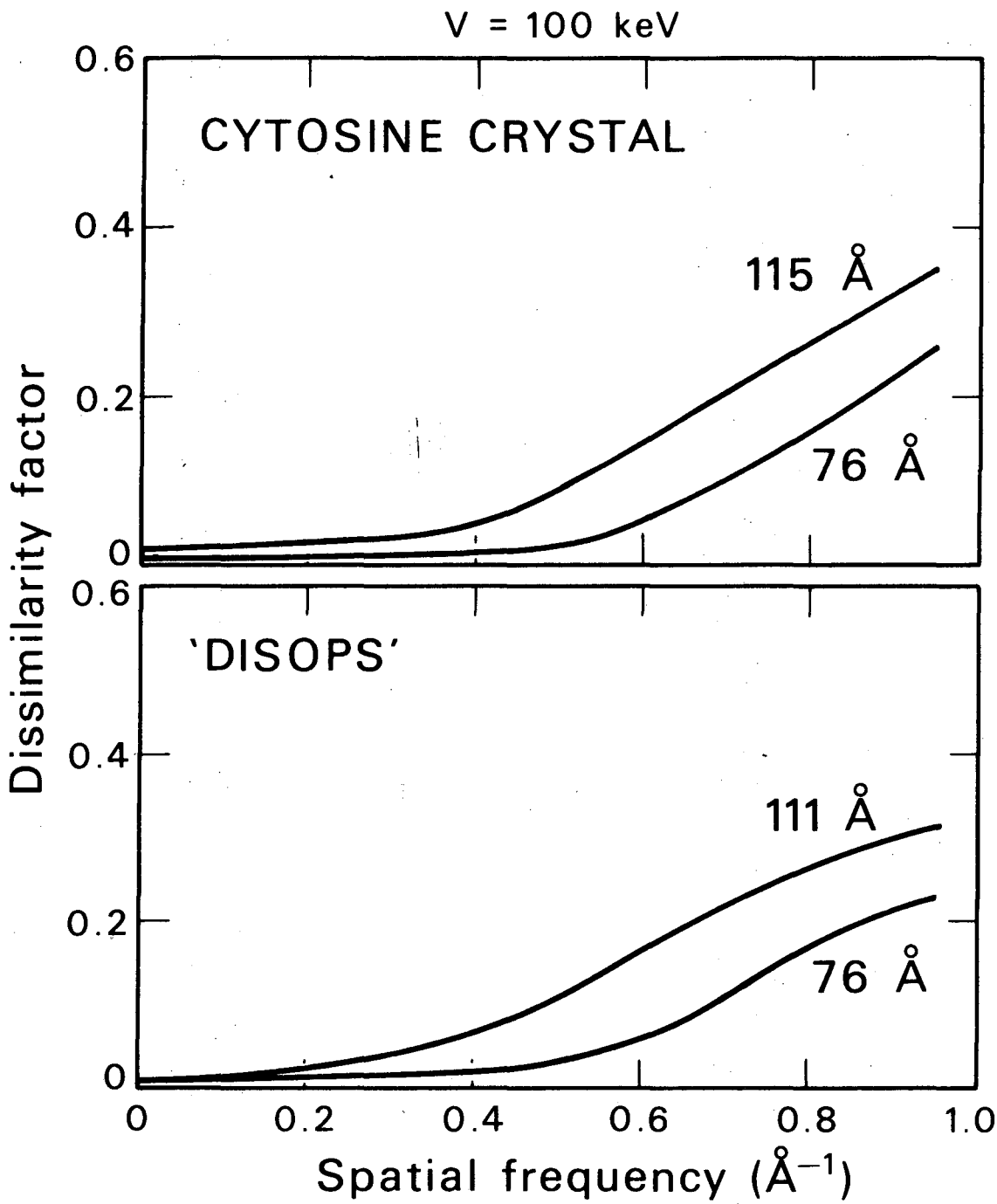

XBL 752-4689

Fig. 13a. For a given crystal thickness, the dissimilarity factor for the projected potential retrieved by the phase object approximation at 100 keV is plotted as a function of spatial frequency. The type of crystal and the crystal thickness used are indicated on the graph.

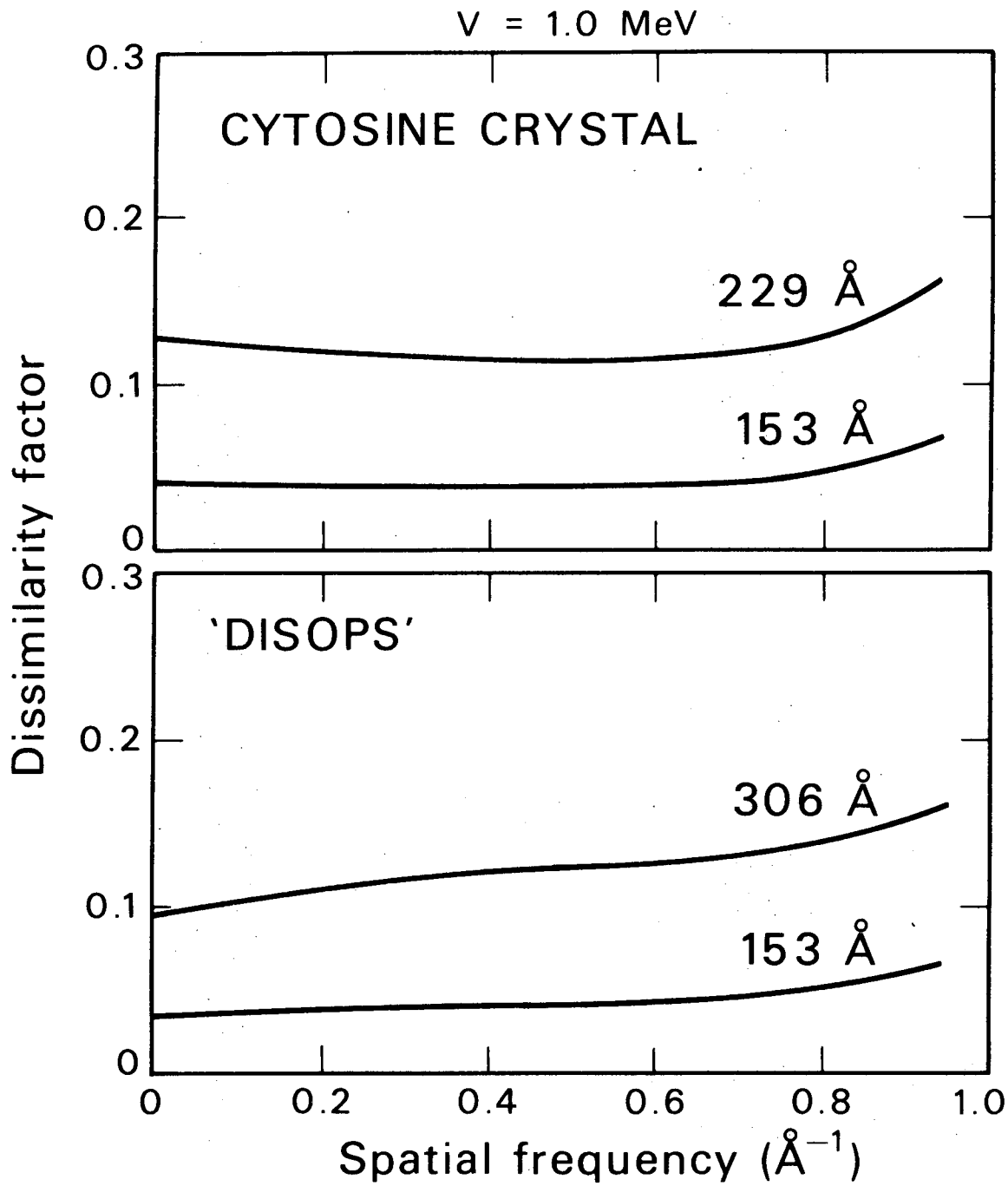

XBL 752-4690

Fig. 13b. For a given crystal thickness, the dissimilarity factor for the projected potential retrieved by the phase object approximation at 1.0 MeV is plotted as a function of spatial frequency. The type of crystal and the crystal thickness used are indicated on the graph.

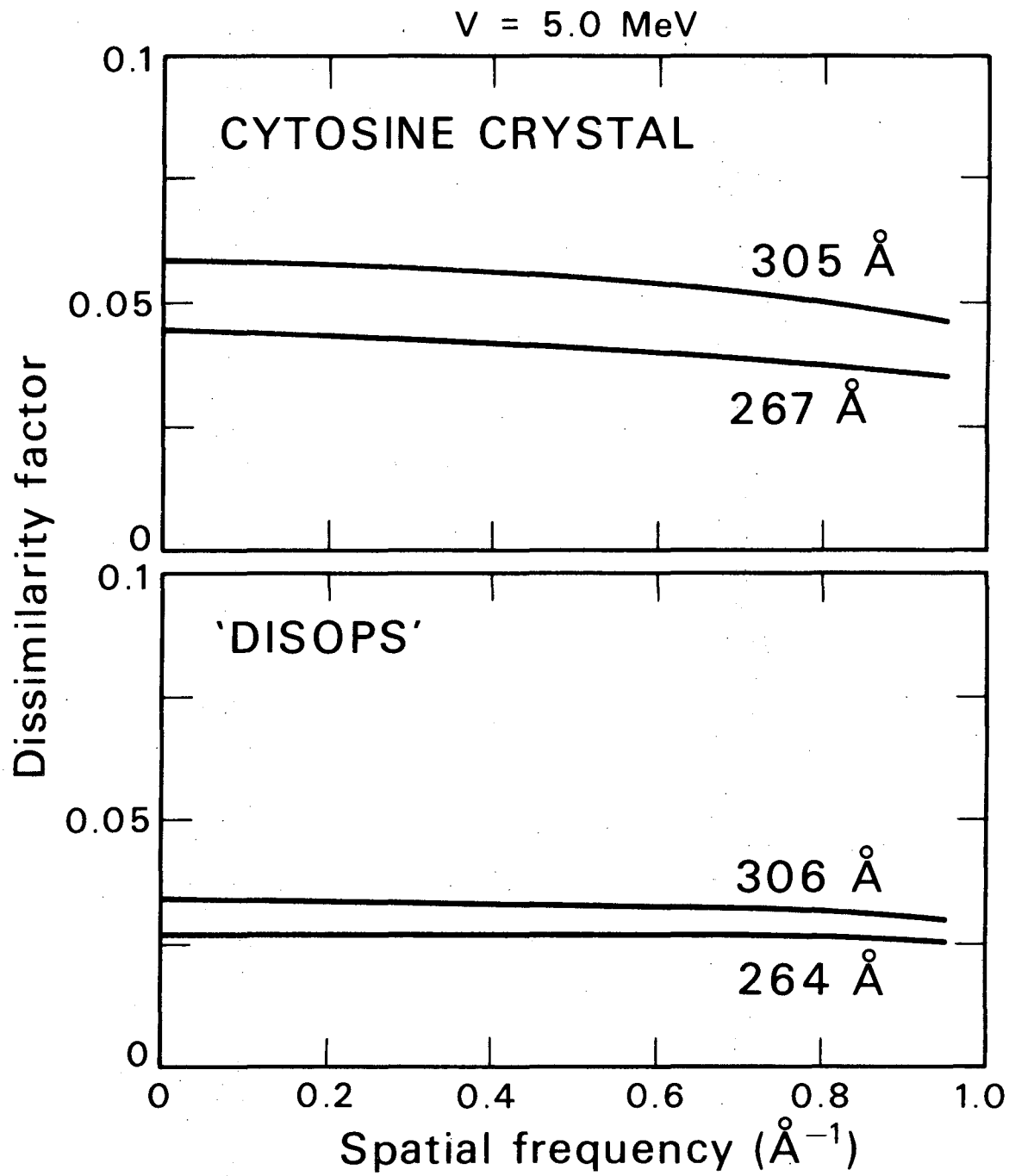

XBL 752-4691

Fig. 13c. For a given crystal thickness, the dissimilarity factor for the projected potential retrieved by the phase object approximation at 5.0 MeV is plotted as a function of spatial frequency. The type of crystal and the crystal thickness used are indicated on the graph.

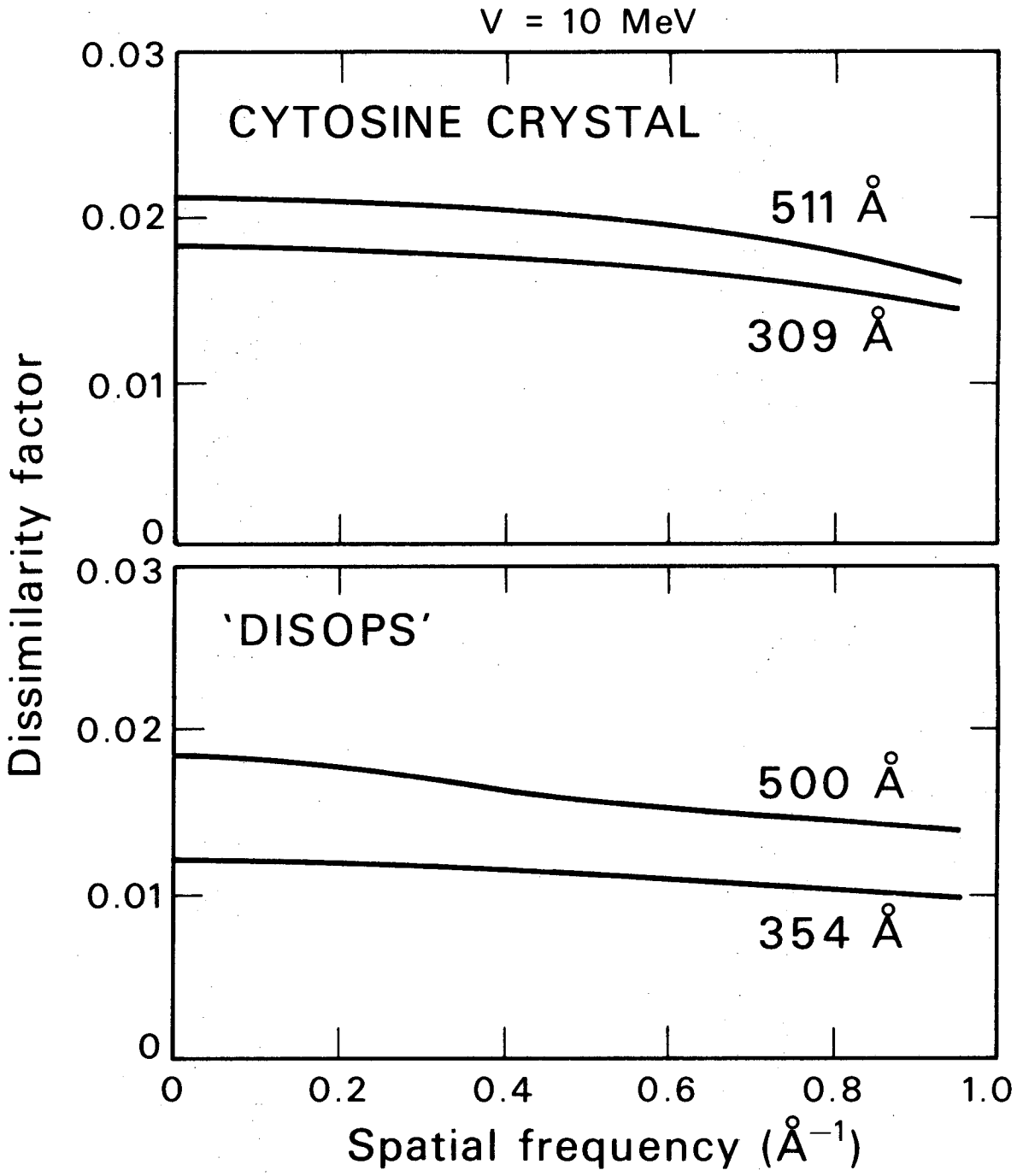

XBL 752-4692

Fig. 13d. For a given crystal thickness, the dissimilarity factor for the projected potential retrieved by the phase object approximation at 10 MeV is plotted as a function of spatial frequency. The type of crystal and the crystal thickness used are indicated on the graph.

The dissimilarity factor gives a validity measure for the projected potential retrieved by the phase object approximation. A large value of the dissimilarity factor indicates that the phase object approximation is invalid. In this manuscript, the phase object approximation is considered valid when the dissimilarity factor is less than 0.05. This value is based on the visual appearance of the displayed projected potentials which possess various values of the dissimilarity factor (Fig. 14). Furthermore, experience in x-ray crystallography has shown that the structure determined is considered valid when the reliability factor is smaller than 0.05. It should be noted here that for a given projected potential retrieved the value of the dissimilarity factor is always less than that of the reliability factor.

Figure 14b-d shows the appearance of the retrieved projected potential for different values of the dissimilarity factor. These figures illustrate that as the value of the dissimilarity factor increases the appearance of the retrieved projected potential becomes gradually dissimilar to the true projected potential. A four to fifteen percent value of the dissimilarity factor shows only a small difference in the overall appearance of the retrieved projected potential. There is, however, a significant change in the high resolution detail. This is because all of the retrieved projected potentials displayed are dominated by the low resolution information; and this low resolution detail possesses a very low value of the dissimilarity factor.

Figure 15 shows the results of the calculation for the validity domain of the phase object approximation. The graphs show that at 100 keV the validity domain of the phase object approximation for the retrieval

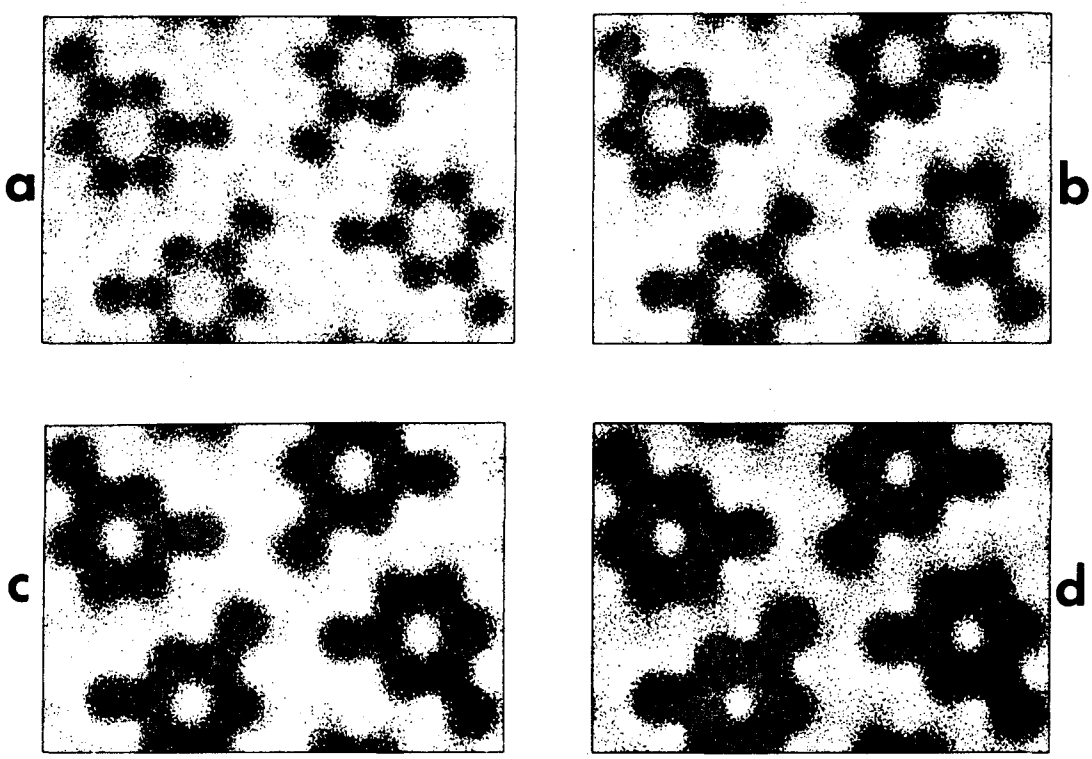

XBL 753-4762

Figure 14. a) The projected potential of the cytosine crystal.

b), c) and d) are the projected potentials calculated by the phase object approximation from the diffracted beams which have been computed on the basis of the multislice dynamical approximation and which have, respectively, the thickness of 5, 9 and 10 unit cells. The number of beams used for retrieving these projected potentials is 355 reflections (resolution: 1.05 Å), and the electron voltage is 100 keV. The dissimilarity factors for b), c) and d) are 4%, 10% and 15% respectively.

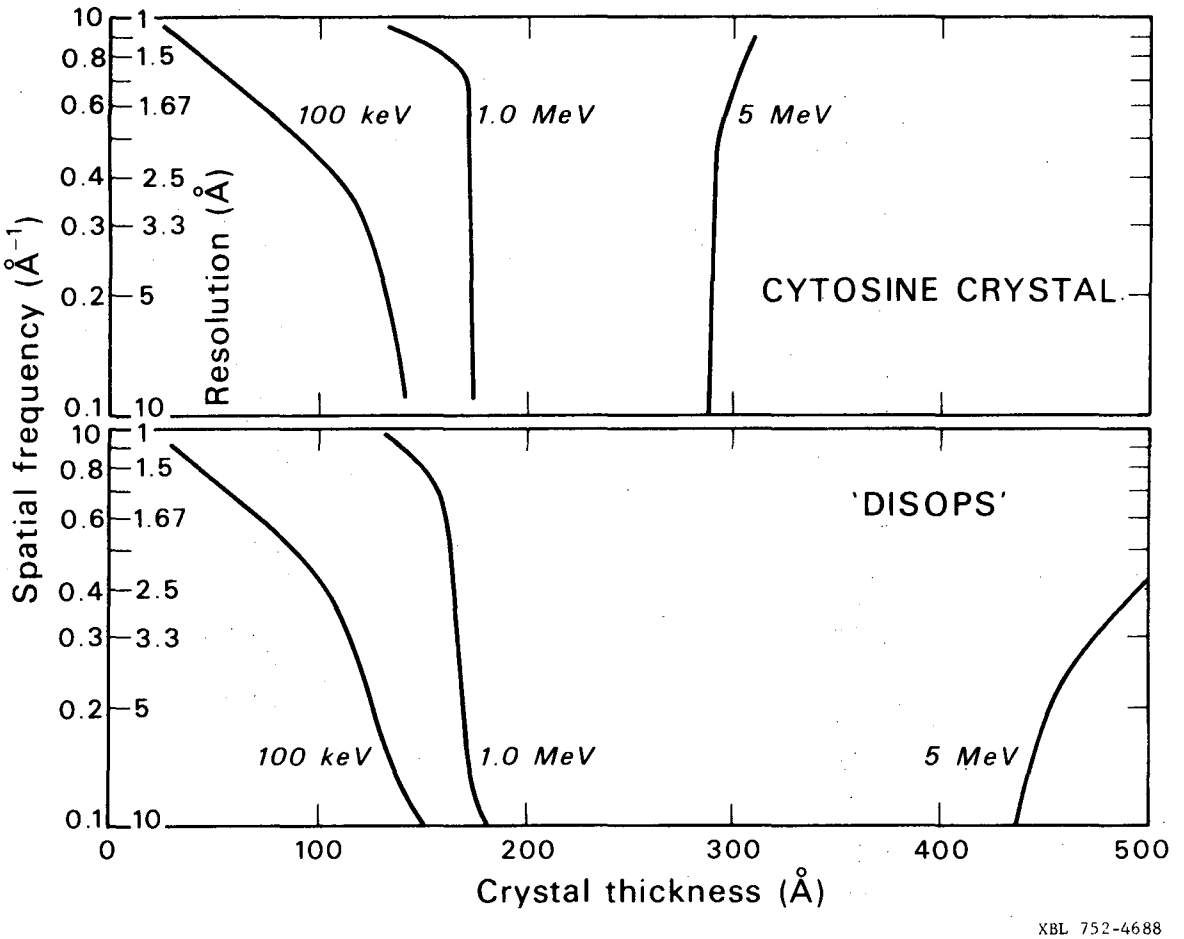

Figure 15. The validity domain of the phase object approximation for the retrieval of the projected potential. The curves correspond to the dissimilarity factor of 0.05.

of the projected potential decreases to the low resolution information as crystal thickness increases. At 5.0 MeV, the validity domain for the high frequency Fourier coefficients or for the high resolution information extends to a larger crystal thickness compared to that for the low resolution information. For a crystal thickness of 40 Å and an accelerating voltage of 100 keV, the phase object approximation is justified for a resolution lower than 1.5 Å. But for an electron energy of 1.0 MeV and the same resolution, the approximation is valid to a crystal thickness of 150 Å. With further increase in electron energy the validity also increases. It should be noted here that the validity domain for the 'DISOPS' at 5.0 MeV is larger than that for the cytosine crystal. This is because the number of beams and the slice thickness used in the calculation of the diffracted waves of these crystals are different. This difference can be expected to contribute a difference in the amount of percentage error to the value of the dissimilarity factor. The difference in the amount of error is expected to increase as the number of slices increases, or in other words, as crystal thickness increases. Since the validity domain at 5.0 MeV extends to a large crystal thickness, it is then clear why the validity domains for the two different crystals are different at this energy.

It is important to note here that the validity domain shown in Fig. 15 was calculated for the case where the diffracted beams extend only to a spatial frequency of 0.95 Å. For the case where the diffracted beams extend to either a larger or a smaller spatial frequency, the validity domain can be anticipated to be different from the one obtained in Fig. 15. This is because the diffracted wave in the phase object

approximation is not related linearly to the projected potential. We can expect that the validity domain will increase as the diffracted beams used are limited to an increasingly low frequency, since the diffracted wave is shown to be increasingly valid as the spatial frequency decreases, or in other words, as the scattering angle becomes very small.

IV. THE VALIDITY DOMAIN OF THE HIGHER ORDER PHASE OBJECT APPROXIMATION

The phase object approximation has been shown in the previous chapter to possess a small domain of validity for the retrieval of the projected potential especially at 100 keV. There is a need, therefore, to develop a new approximation which has a larger domain of validity and which still retains the invertible relationship between the transmitted wave function and the projected potential. The higher phase object approximation was developed in Chapter II under these considerations. It was derived by taking not only the straight line path resulting in the phase object approximation, but also some specific non-straight line paths. Compared to the phase object approximation, the higher phase object approximation can therefore be expected to possess a larger domain of validity. In this chapter we will evaluate quantitatively the expected larger domains of validity for the retrieval of the projected potential in the higher order phase object approximation at 100 keV.

A. Approximation

The diffracted wave function in the higher order phase object approximation can be described by the product of the Fourier transform of the transmitted wave function and the Fourier transform of "the function" characterized by the higher order phase object approximation. The diffracted wave can be represented by equation (25). In order to obtain this diffracted wave function, the Fourier transforms of both functions have to be evaluated. The computer time required for the calculation of the diffracted wave function can be substantially reduced

when "the function" can be approximated by a function whose Fourier transform can be expressed in an analytical form. For small angle scattering we can approximate "the function" in such a manner. To show this, let us first expand "the function" in power series as

$$\left[\frac{\exp(-ik\rho^2/2\tilde{Z}_o) - \exp(-ik\rho^2/2Z_{POA})}{-ik\rho^2\left(\frac{1}{\tilde{Z}_o} - \frac{1}{Z_{POA}}\right)/2}\right] = 1 - \frac{1}{2!}\left(\frac{ik\rho^2}{2}\right)\left(\frac{1}{\tilde{Z}_o} + \frac{1}{Z_{POA}}\right)$$

$$+ \frac{1}{3!}\left(\frac{ik\rho^2}{2}\right)^2\left(\frac{1}{\tilde{Z}_o^2} + \frac{1}{\tilde{Z}_o Z_{POA}} + \frac{1}{Z_{POA}^2}\right) + \ldots\ldots \qquad (46)$$

We can rewrite this series as

$$\left[\frac{\exp(-ik\rho^2/2\tilde{Z}_o) - \exp(-ik\rho^2/2Z_{POA})}{-ik\rho^2\left(\frac{1}{\tilde{Z}_o} - \frac{1}{Z_{POA}}\right)/2}\right] = \exp\left(\frac{-ik\rho^2}{4}\left(\frac{1}{\tilde{Z}_o} + \frac{1}{Z_{POA}}\right)\right)$$

$$+ \frac{1}{24}\left(\frac{ik\rho^2}{2}\right)^2\left(\frac{1}{\tilde{Z}_o} - \frac{1}{Z_{POA}}\right)^2 + \ldots\ldots \qquad (47)$$

For a small angle, such that the sum of the series in $\frac{k\rho^2}{Z_{POA}}$ is small compared to the exponential function or "gaussian function", we can then neglect the series; and then write the diffracted wave function as

$$F(\vec{k},\vec{k}_o) = \exp(-ik\tilde{Z}_o)\ \mathcal{F}\left[\exp\left(-\frac{i}{\hbar v}\int_{Z_o}^{Z} V(\rho,Z')dZ'\right)\right]$$

$$\cdot \exp\left(\frac{i2\pi\lambda\tilde{Z}_o(h^2 + k^2)}{\left(1 + \frac{\tilde{Z}_o}{Z_{POA}}\right)}\right), \quad \text{for } \tilde{Z}_o > Z_{POA} \qquad (48)$$

where (h,k) are Miller indices. It may be helpful to note that the Fourier transform of a "gaussian function" can be expressed in the analytical form.

The error from such an approximation is of second and higher order terms in nature and can be expected to be quite small when the series converges very rapidly. For instance, the error of the leading term is less than one quarter of the true second order term. We will use such an approximation in the calculation of the diffracted wave function.

B. Calculation Method

The calculation method for the determination of the validity of the higher order phase object approximation follows in a very similar manner as in the case for the phase object approximation described in the previous chapter. The diffracted wave in the higher order phase object approximation differs from that of the phase object approximation by an additional "gaussian function". Detailed calculation methods for the diffracted wave will therefore not be described again here.

The value of Z_{POA} used in the calculation of the diffracted wave function at 100 keV is taken to be 5 unit cells ($\sim$ 19 Å) for cytosine crystal and 3 unit cells ($\sim$ 21 Å) for 'DISOPS'.

C. Results and Discussion

Since the diffracted wave in the higher order phase object approximation differs from that of the phase object approximation by a phase factor, the diffracted beam intensity in both cases is therefore

the same. Thus, the validity of the diffracted beam intensity in the higher order phase object approximation is the same as that of the phase object approximation described in the previous chapter and will therefore not be discussed.

1. The Phase of the Diffracted Wave

The phases of the diffracted beams as a function of crystal thickness at 100 keV have been computed by the higher phase object approximation. Figure 16a,b displays the phases of the high and the low frequency reflection for both cytosine crystal and 'DISOPS'. In these graphs, the phases computed by the phase object approximatoin and by the multislice dynamical approximation are also displayed for comparison. The graphs indicate that the phases in the higher order phase object approximation, when compared to that in the phase object approximation, show an improved agreement with the 'exact' phases computed by the multislice dynamical approximation. At very large crystal thickness, both the higher order phase object approximation and the phase object approximation fail to describe the phase of the diffracted waves.

2. The Image Intensity

The image intensity can be used to give some qualitative measure of the validity of the higher order phase object approximation. Figure 17 shows the image intensities of cytosine crystal (∿ 38 Å thick) calculated by the multislice dynamical approximation, phase object approximation and the higher order phase object approximation. The display indicates that the image intensity of the higher order phase object approximation closely resembles the 'exact' image intensity

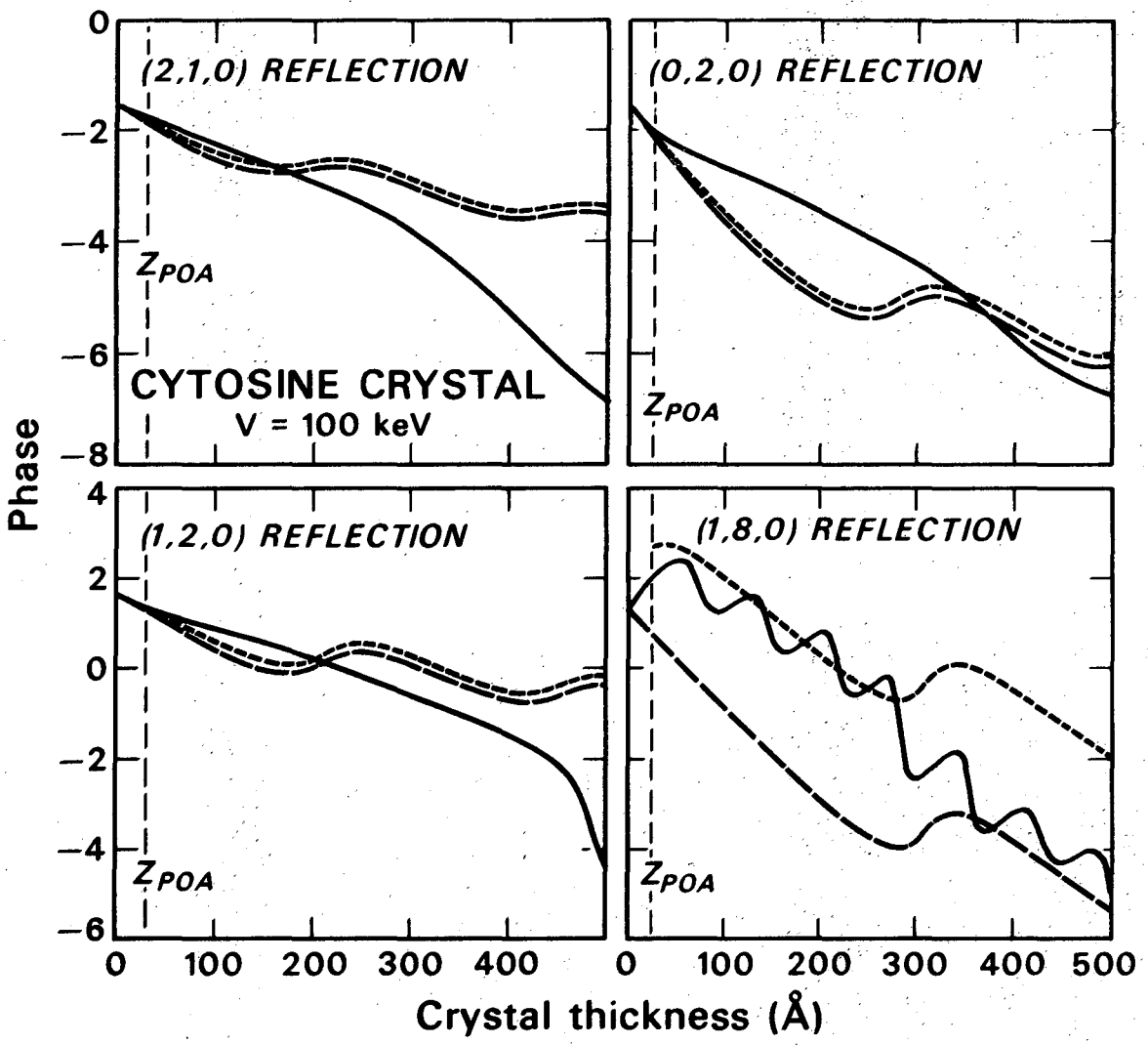

Fig. 16a. The phases of the low and high frequency diffracted beams at 100 keV are plotted as a function of crystal thickness. The crystal is cytosine. Phase object approximation (– – – –), multislice dynamical approximation (———) and higher order phase object approximation (------). The Miller indices of the diffracted beams are indicated on the graph.

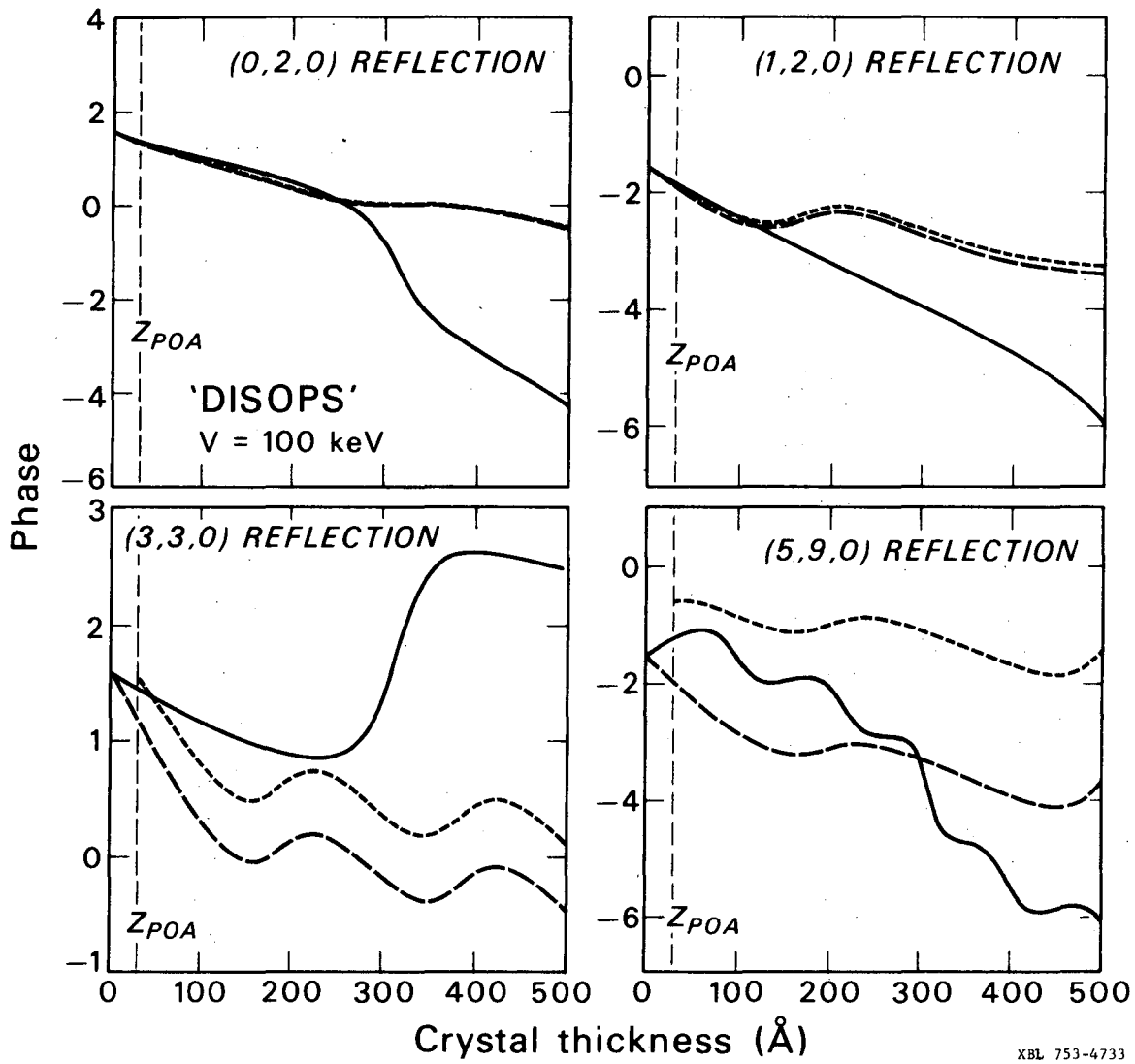

Fig. 16b. The phases of the low and high frequency diffracted beams at 100 keV are plotted as a function of crystal thickness. The crystal is 'DISOPS'. Phase object approximation (– – – –), multislice dynamical approximation (————) and higher order phase object approximation (-------). The Miller indices of the diffracted beams are indicated on the graph.

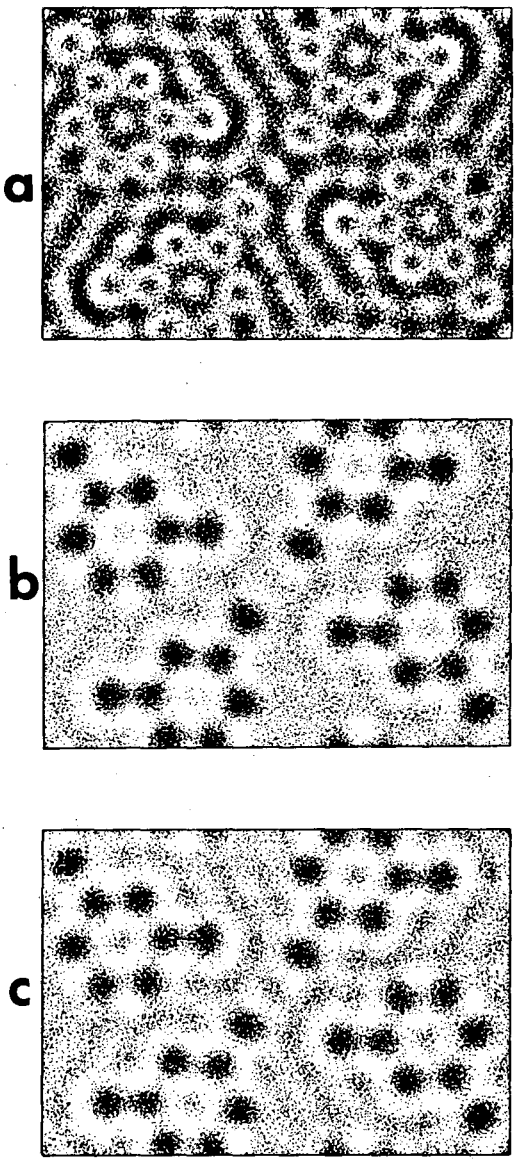

XBL 753-4761

Figure 17. The image intensity of cytosine crystal (38 Å) at 100 keV calculated by a) phase object approximation, b) multislice dynamical approximation, and c) higher order phase object approximation.

calculated by the multislice dynamical approximation, whereas the image intensity in the phase object approximation differs significantly. It is clear then that the higher order phase object approximation is superior in accuracy when compared to the phase object approximation.

3. The Validity of the Higher Order Phase Object Approximation for the Retrieval of the Projected Potential

The dissimilarity factor as a function of spatial frequency for the projected potential retrieved by the higher order phase object approximation was evaluated as a function of crystal thickness. Figure 18 shows at 100 keV the typical features of the dissimilarity factor as a function of crystal thickness. The graphs indicate that the dissimilarity factor, for a given crystal thickness, increases slowly with spatial frequency. Compared to that of the phase object approximation (Fig. 13a) the dissimilarity factor of the higher order phase object approximation for the same crystal thickness decreases. One can conclude that the higher order phase object approximation, when compared to the phase object approximation, gives an improvement in accuracy.

As in the case of the phase object approximation, the higher order phase object approximation is considered valid when the dissimilarity factor of the retrieved projected potential is less than 0.05. The results of the higher order phase object approximation at 100 keV are displayed in Fig. 19. The graphs show that as crystal thickness increases, the validity of the projected potential retrieved by the higher order phase object approximation decreases very rapidly to low resolution information. However, when compared to the phase object approximation the higher order phase object approximation possesses a larger domain

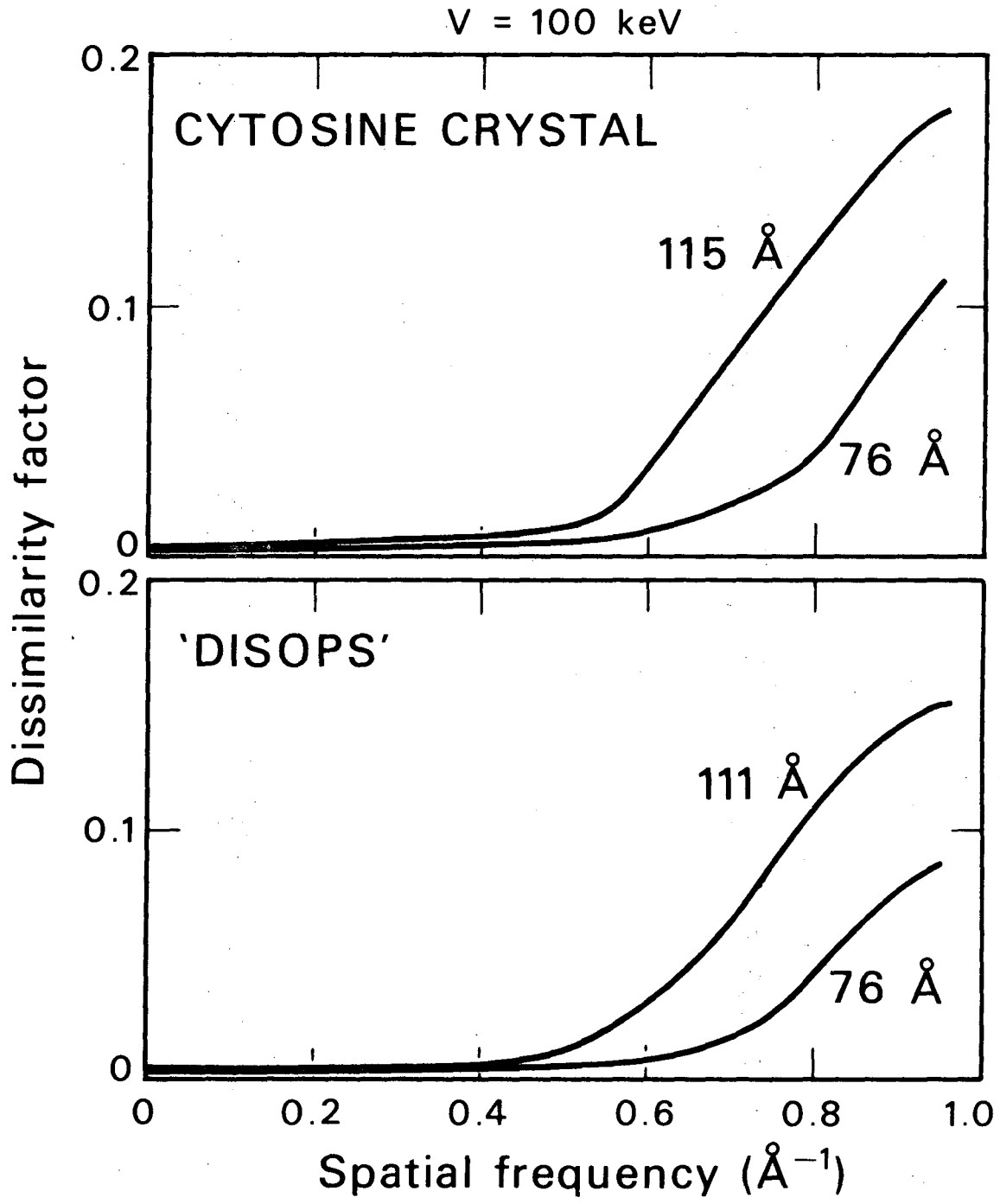

XBL 753-4731

Figure 18. For a given crystal thickness the dissimilarity factor for the projected potential retrieved by the higher order phase object approximation is plotted as a function of spatial frequency. The crystal thickness and the type of crystal used are indicated on the graph.

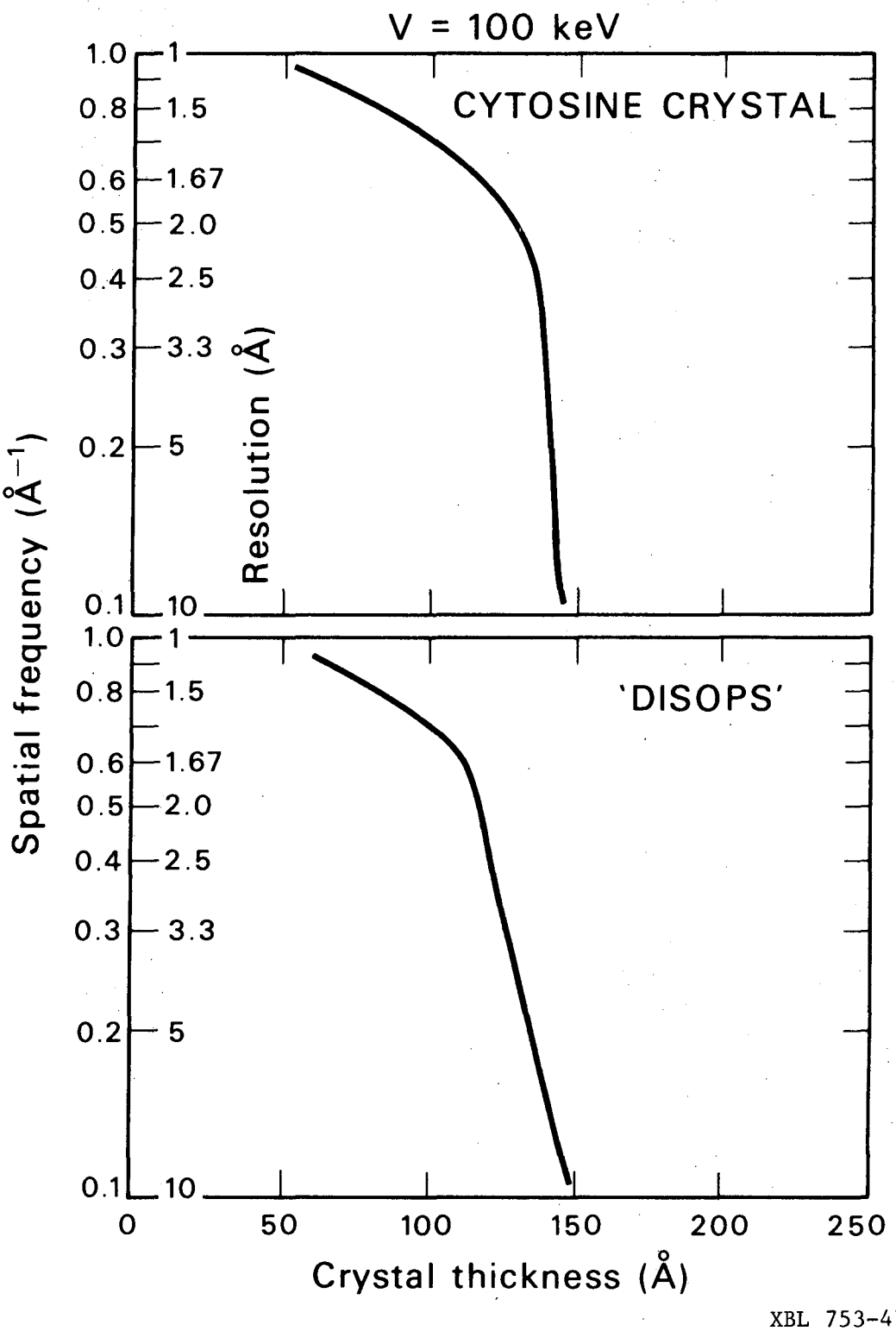

Figure 19. The validity domain of the higher order phase object approximation for the retrieval of the projected potential. The curves correspond to the dissimilarity factor of 0.05.

of validity. For crystal thickness of 30 Å, the higher order phase object approximation is valid up to a resolution of 2 Å, whereas the phase object approximation is limited to resolution of less than 5 Å. With further increases in crystal thickness the validity of both approximations gradually coincide. This is expected since the amplitudes of the diffracted waves for both approximations are the same and since the validity of these amplitudes can effect the limit of the validity domain. It can be concluded that the higher order phase object approximation indeed possesses a larger domain of validity for the retrieval of the projected potential.

V. VOLTAGE DEPENDENT CONTRAST IN ORGANIC CRYSTAL IMAGES

One of the factors limiting the interpretation of the crystal image is the contrast. Image contrast in electron microscopy depends on the amount of aberration which is due to the imperfection of the lens and also on the character of the scattered electrons forming the image. Inelastically scattered electrons, for instance, can reduce the image contrast and therefore are undesirable for high resolution imaging. The reason for this reduction in contrast is that because of the chromatic aberration, the inelastic scattered electron waves suffer various amounts of phase distortion depending on the energy loss. The contribution of these electron waves results in an increase of the background intensity of the image. The lens aberrations, other than chromatic aberration, can also affect the contrast of the image. However, this effect can be optimized by suitable choice of defocus and aperture size.

High voltage electron microscopy is an attractive tool for high resolution structural investigation of biological specimens. In previous chapters, we have demonstrated that the simple invertible dynamical approximations possess a larger domain of validity as the electron energy increases. High voltage electron microscopy, therefore, is the practical way to solve the dynamical scattering effect problem. Furthermore, experiments in radiation damage have shown that the critical exposure of biological specimens increases as the electron voltage increases. This is advantageous for structural studies of biological specimens where radiation damage limits the possibility of imaging the high resolution structure. Calculations for single atom images have indicated that except for a carbon atom, contrast increases for high voltage

microscopy (Siegel, B.M., 1971). The high contrast can definitely lower the electron exposure needed to obtain an acceptable signal-to-noise ratio and allows the beneficial reduction in radiation damage. This reduction gives in turn an increase in image contrast. It is therefore essential to study theoretically the effect of dynamical scattering at different electron energies, with respect to the contrast of organic crystal images.

Image contrast of inorganic crystals has been calculated previously by others for different object thicknesses at 100 keV, in order to interpret the observed high resolution images. Using the phase object approximation, Fejes (1971) has computed the contrast of high resolution image of $Ti_2Nb_{10}O_{29}$ crystal employing the "optimum defocus condition" proposed originally by Scherzer. His result showed that contrast increases with object thickness up to 100 Å and then levels off. On the basis of the large phase change occurring in the phase object approximation, Cowley and Iijima (1972) have also made the same prediction which is in agreement with the observed high resolution crystal image. However, the effect of dynamical scattering at different electron energies on crystal image contrast has not previously been considered.

The purpose of this chapter is to study theoretically the effect of dynamical scattering at different electron energies on the contrast of high resolution images of organic crystals. In the calculation, images of the known structure were computed using the multislice dynamical theory and inelastically scattered electrons have been ignored. The calculated diffracted wave is given a phase distortion in order to consider the effect of both the spherical aberration and defocus of the lens. The phase distortion is optimized by suitable choice of defocus and aperture size.

A. "Optimum Defocus Condition"

Because of the imperfection of the lens in the electron microscope the image quality is mainly complicated by the spherical aberration of the lens. In order to minimize this the image is given a defocus to compensate the spherical abberation. Even if the electron optical lens is perfect it is very difficult, in practice, to obtain an in-focus image. Lens aberration as well as defocusing produce an artifact on the electron image. The phase distortion function accounts for this aberration. The effect of spherical aberration and defocusing causes a phase shift in the diffracted waves. This phase shift depends on the scattering angle of the electrons, or in other words, depends on the spatial frequency. This phase distortion function, H(s), is given by

$$H(s) = e^{i\gamma(s)}, \quad \text{and} \quad \gamma(s) = \pi s^2\lambda(C_s s^2\lambda^2/2 - \Delta f) \qquad (49)$$

where C_s is the spherical aberration coefficient of the lens, Δf is the amount of defocus, λ is the electron wavelength, and s is the spatial frequency. The defocus is positive when the image is observed below the plane of the in-focus image.

In order to get a faithful propagation of the phase detail of the diffracted wave, the exponent in the phase distortion function should be kept close to constant or zero for the largest domain of spatial frequency. For a given spherical aberration coefficient and electron accelerating energy, this exponent can be optimized over a limited domain of the diffraction angle by varying the defocus of the lens. The "optimum defocus condition" introduced first by Scherzer designates the optimum

value of the defocus as well as of the aperture size. It can be shown that the "optimum defocus condition", or the Scherzer criteria, fulfills the following relations (Eisenhandler, G.B. and Siegel, B.M., 1966):

$$(C_s\lambda)^{\frac{1}{2}} \leq \Delta f \leq (2C_s\lambda)^{\frac{1}{2}}$$
$$s_{AP} = (2\Delta f/C_s\lambda^2)^{\frac{1}{2}} \tag{50}$$

where λ is the electron wavelength, s_{AP} is the aperture limit, and $\Delta f, C_s$ are, respectively, the defocus and spherical aberration coefficient of the lens.

B. Image Contrast of Crystals

Image contrast is a measure of the image quality and gives some quantitative measurement about the discrimination of the image from the background intensity. It has been conventionally defined as

$$C = \frac{I_{max} - I_{min}}{(I_{max} + I_{min})/2} \tag{51}$$

where I_{max} and I_{min} are, respectively, the maximum and minimum image intensity in the given area of the image where this contrast is measured. This type of contrast is useful for single atom imaging where the interest has been to differentiate the single atom imaging from the background intensity due to the substrate. For crystalline objects, such defined contrast can neither give a measure for the average image contrast, nor can it discriminate between the average contrast from low and high resolution information of the structure. Some measure of resolution-

dependent contrast could therefore be informative.

For crystalline objects the amplitude of the Fourier spectrum at a given frequency is related to the image intensity which possesses the information of the resolution corresponding to that frequency. The resolution-dependent contrast for a periodic image can then be calculated by measuring each coefficient of the Fourier spectrum of the image intensity. This type of contrast can be represented by the following equation

$$C(h,k) = \frac{4|F(h,k)|}{F(0,0)} \tag{52}$$

where $F(h,k)$ is the Fourier coefficient of the image intensity and h,k are integer numbers corresponding to the Miller indices in the crystal lattice.

For comparison of crystal image contrasts at different electron accelerating energies, the resolution-dependent contrast gives too detailed an amount of information, whereas we need a simple measure of the contrast that is being contributed by all of the spatial frequencies together. Integration of the resolution-dependent contrast over the possible frequencies can give some measure of the average quality of the crystal image. This contrast can be described by the following equation

$$C' = \frac{\sum_{h,k}' |F(h,k)|}{|F(0,0)|} \tag{53}$$

where C' is the contrast and $F(h,k)$ is the Fourier coefficient of the image intensity with the spatial frequency (h,k). The prime in the summation means that the zero frequency coefficient has been omitted.

C. Image Wave and the Fourier Spectrum of the Image Intensity

The image wave can be computed by the inverse Fourier transform of the product of the diffracted wave, the phase distortion function, and aperture function. This image wave can be represented by the following equation

$$\psi_{image}(x,y) = \mathfrak{F}^{-1}[\phi(s) \cdot H(s) \cdot A(s)] \tag{54}$$

where $\psi_{image}(x,y)$ is the image wave, $\phi(s)$ is the diffracted wave, $H(s)$ is the phase distortion and $A(s)$ is the aperture function. The value of the aperture function is unity when the spatial frequency is smaller than that of the 'aperture limit', and is zero elsewhere.

The image intensity is the product of the image wave and its complex conjugate:

$$I(x,y) = \psi_{image}(x,y) \cdot \psi^{+}_{image}(x,y) \tag{55}$$

The Fourier spectrum of the image intensity is defined as the Fourier transform of the image intensity and for central symmetric image can be described as the convolution between the diffracted wave, modified by the phase distortion function, and its complex conjugate as

$$F(h,k) = \mathfrak{F}^{-1}[I(x,y)] = [\phi(s)H(s)A(s)] * [\phi^{+}(-s)H^{+}(-s)A(-s) \tag{56}$$

For crystalline objects, doing this convolution directly is less time consuming than calculating first the image intensity and then obtaining the Fourier spectrum, since the number of the diffracted beams after the reduction afforded by symmetry is quite small.

D. Calculation Method

The diffracted wave function of a given crystal can be calculated using the multislice dynamical approximation. Detailed calculation methods for the diffracted wave function of a crystal of any given thickness has already been discussed in Chapter III. As in Chapter III, two different organic crystals, cytosine and 'DISOPS', were used as test objects in order to show that the results obtained here do not depend specifically on the crystal structure. In the calculation of the diffracted wave function, the number of beams used is 355 and 543 respectively for cytosine and 'DISOPS'. The slice thickness was taken to be the unit cell in the c-axis.

The lens aberrations were introduced by multiplying the diffracted wave function with the phase distortion function. The spherical aberration coefficient of the electron microscope was assumed to be C_s = 0.7 mm at 100 keV. Such a small value in the spherical aberration is practical and also commercially available in today's high resolution electron microscope. The spherical aberration coefficients at high electron energies were obtained by keeping $C_s\lambda$ constant, or in other words, without changing the strength of the magnetic lenses of the microscope. The amount of defocus is calculated according to the Scherzer criteria. The values for the lens parameters are listed in Table 1 for different electron energies.

The Fourier spectrum of the image intensity can be obtained from the diffracted wave following equation (56). The image contrast can then be calculated from the Fourier spectrum of the image intensity.

TABLE 1

Electron microscopical parameters used in the calculation of contrast.

Electron energy (MeV)	Electron wave length (Å)	Spherical Aberration Coefficient Cs (mm)	Defocus (Å)	Aperture limit (Å)	Resolution* (Å)
0.1	3.70×10^{-2}	0.70	620	0.38	2.63
1.0	8.72×10^{-3}	2.97	620	0.74	1.35
5.0	2.26×10^{-3}	11.47	620	1.45	1.05†
10.0	1.18×10^{-3}	21.94	620	2.00	1.05†

*The resolution defined as the reciprocal of the largest spatial frequency reflection is included.

†The diffracted beam used in the calculation of the diffracted wave is limited to the spatial frequency of less than 0.95 $Å^{-1}$ which is smaller than the aperture size used at 5.0 or 10.0 MeV.

E. Results and Discussion

Resolution-dependent contrast as well as integrated contrast for the image intensity of organic crystals have been calculated for various thicknesses and for different electron accelerating energies. For a given resolution, the resolution-dependent contrast fluctuates with crystal thickness without any obvious periodicity, and is not linearly proportional to the amplitude of the diffracted wave (i.e., the larger the amplitude of the diffracted wave the greater the resolution-dependent contrast) as would be expected when the kinematic approximation is valid. This contrast, in most cases decreases in average amplitude as the electron energy increases (Figs. 21a-d, 22a-d). This decrease is expected because the total cross section for the elastic electron scattering decreases also with increasing electron energy.

For a given electron energy, the integrated contrast increases linearly with crystal thickness and then levels off (Fig. 23a,b). For example, at 100 keV, the integrated contrast, for either cytosine or 'DISOPS', increases linearly up to a thickness of about 100 Å and then fluctuates irregularly with its average amplitude remaining constant. As electron energy increases to 1.0 MeV, there is a net increase in the integrated contrast. The integrated contrast increases by about 100% as the voltage increases from 100 keV to 1.0 MeV. Beyond 1.0 MeV the integrated contrast remains almost the same. This is because for 5.0 MeV and 10.0 MeV, the number of beams used in the computation of the diffracted waves is smaller than that which is actually needed: the number of beams employed in the calculation was limited to the resolution of about 1.05 Å, while the aperture limit extends to higher resolution.

It should be noted that the number of beams used at 10.0 MeV was taken to be the same as that at 5.0 MeV. Since the integrated constant at 10.0 MeV is slightly less than that at 5.0 MeV, it is clear then that the integrated contrast of the images possessing the same information decreases with an increase of electron energy. We can conclude that the increase in integrated contrast at high energy cases is due to the increase in the number of beams allowed to pass through the aperture. That is to say, the increase at high energies is due to the increase in information of the image.

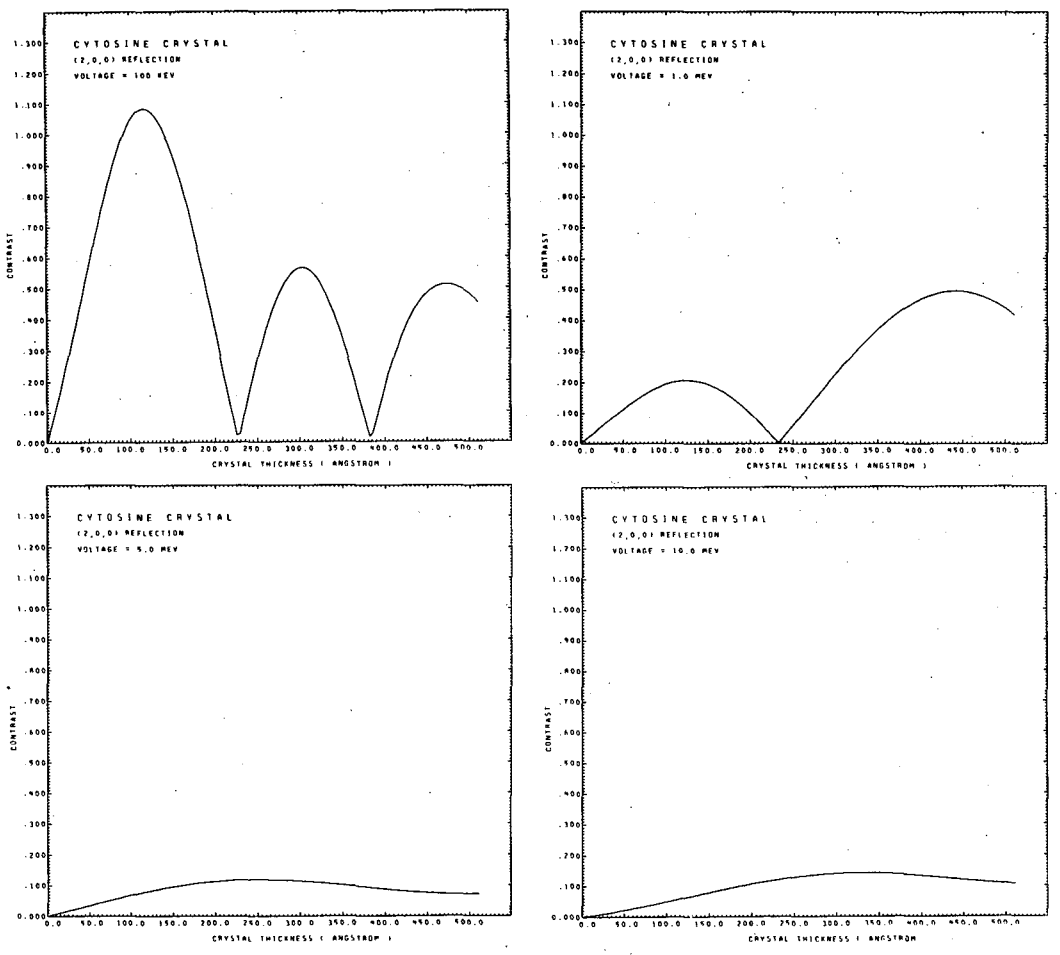

XBL 752-344

Fig. 21a. Resolution dependent contrast for the (2,0,0) reflection is plotted as a function of crystal thickness. The electron accelerating voltage used is indicated on the graph. The crystal is cytosine.

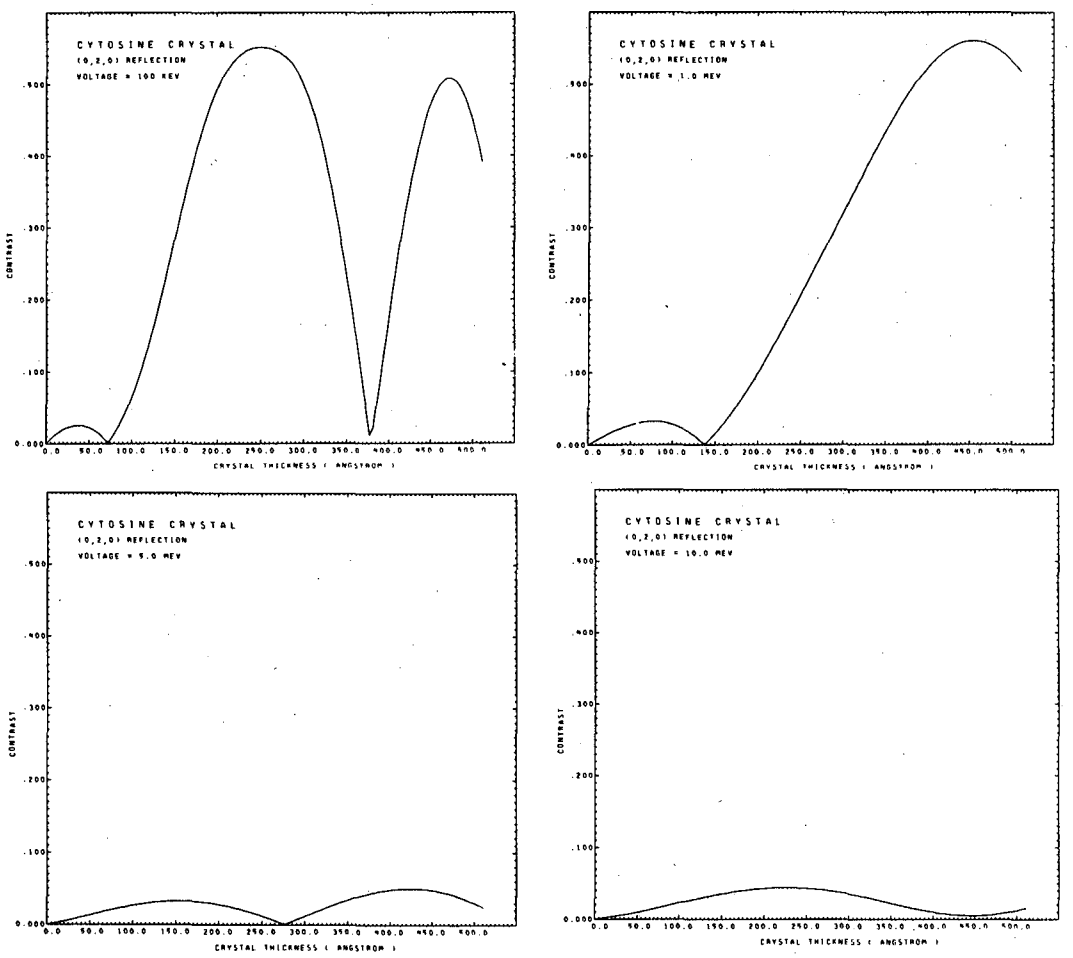

XBL 752-345

Fig. 21b. Resolution dependent contrast for the (0,2,0) reflection is plotted as a function of crystal thickness. The electron accelerating voltage used is indicated on the graph. The crystal is cytosine.

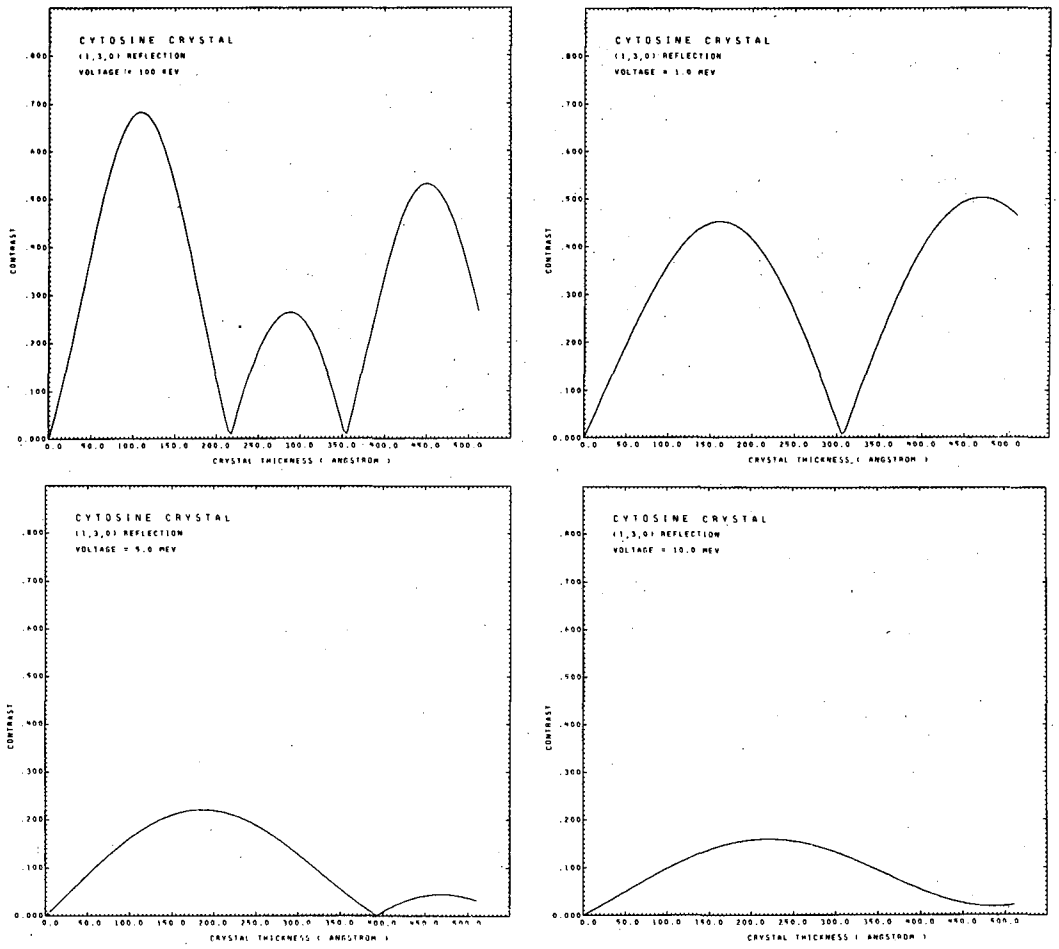

XBL 752-347

Fig. 21c. Resolution dependent contrast for the (1,3,0) reflection is plotted as a function of crystal thickness. The crystal is cytosine. The electron accelerating voltage used is indicated on the graph.

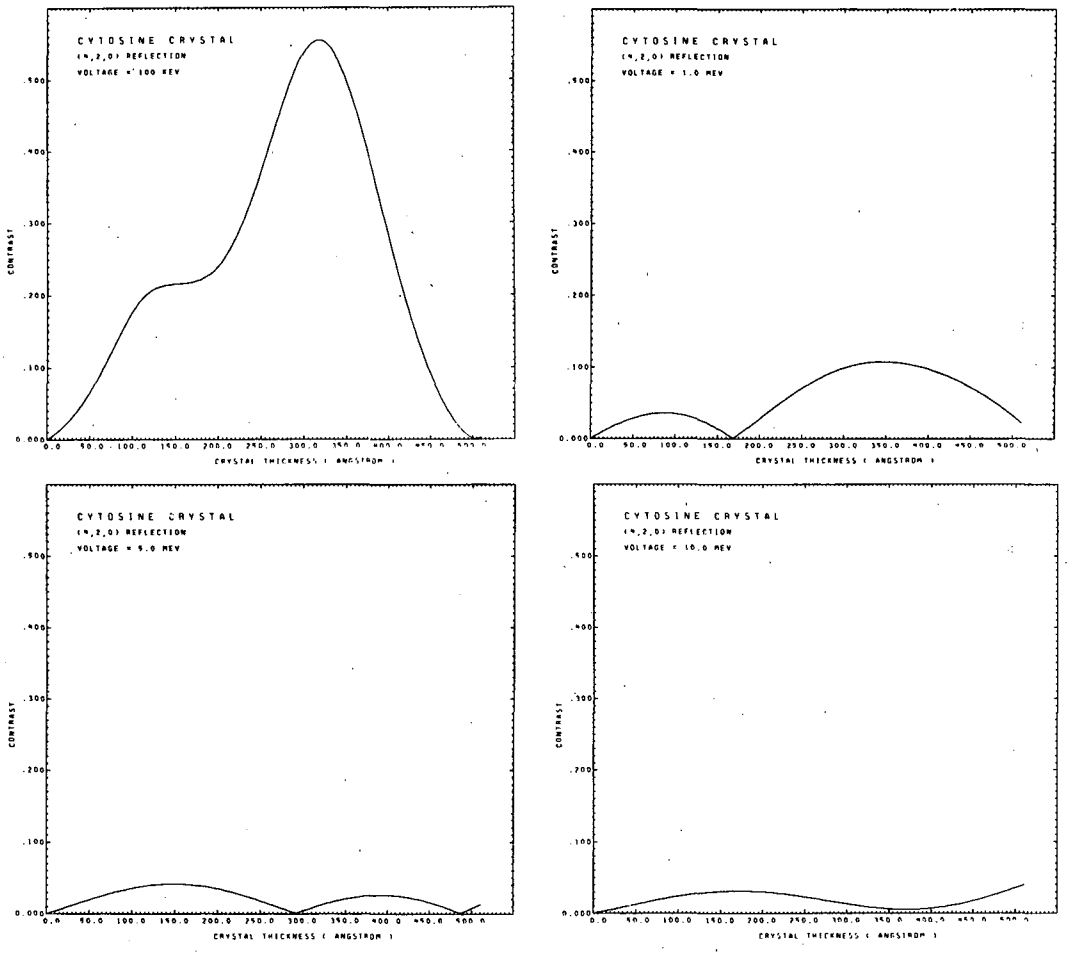

XBL 752-348

Fig. 21d. Resolution dependent contrast for the (4,2,0) reflection is plotted as a function of crystal thickness. The crystal is cytosine. The electron accelerating voltage used is indicated on the graph.

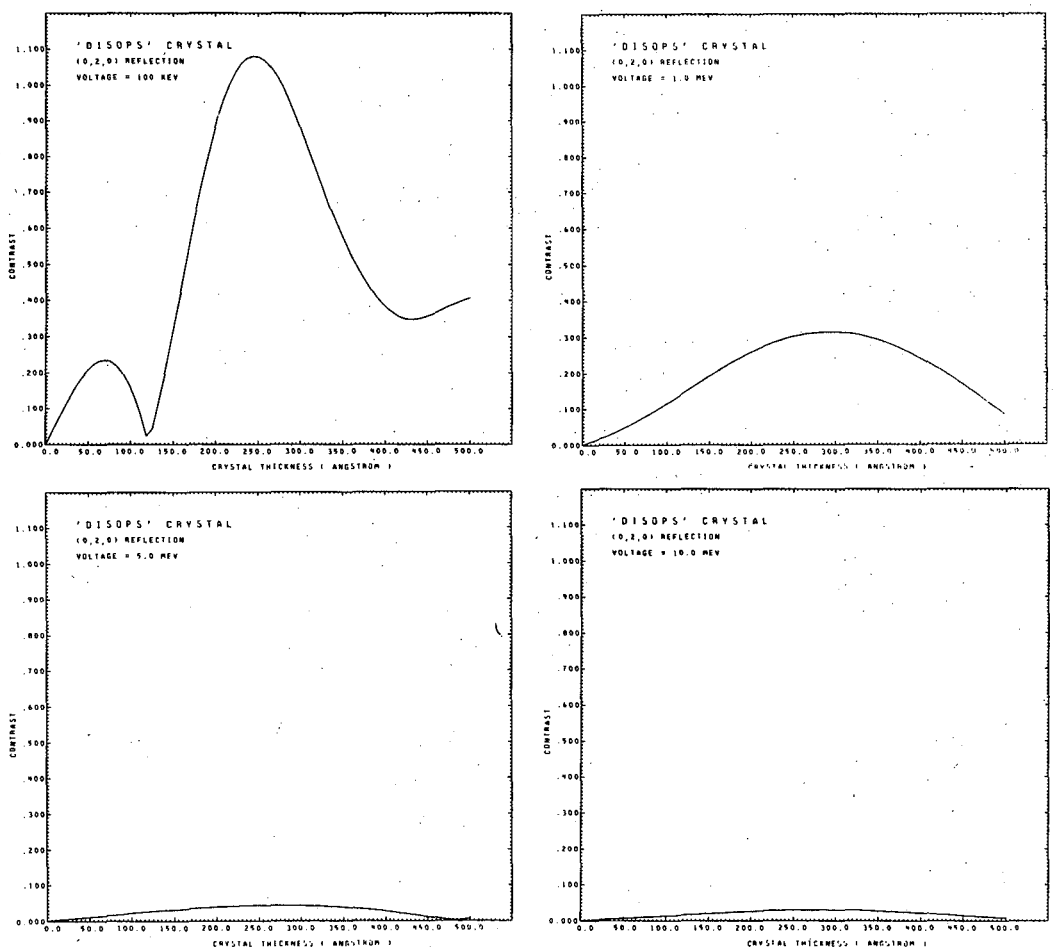

XBL 752-354

Fig. 22a. Resolution dependent contrast for the (0,2,0) reflection is plotted as a function of crystal thickness. The crystal is 'DISOPS'. The electron accelerating voltage used is indicated on the graph.

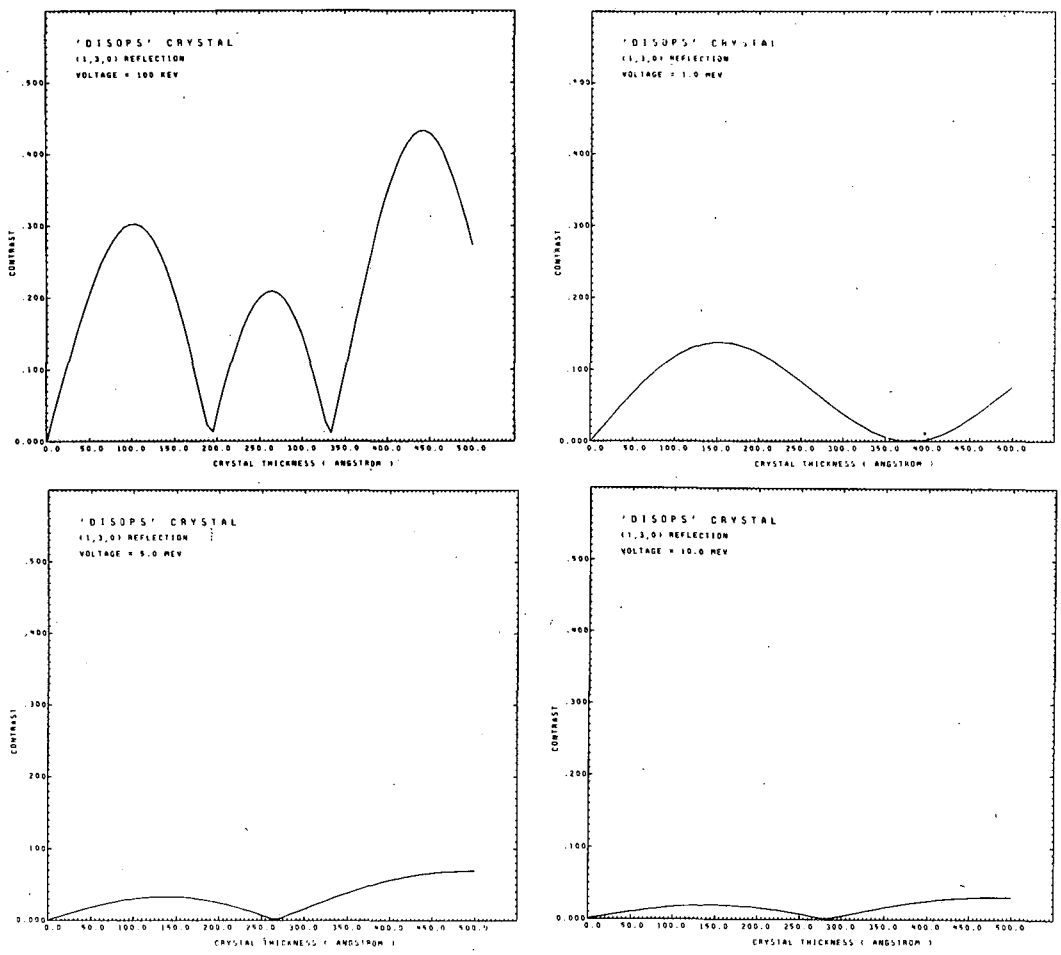

XBL 752-351

Fig. 22b. Resolution dependent contrast for the (1,3,0) resolution is plotted as a function of crystal thickness. The crystal is 'DISOPS'. The electron accelerating voltage used is indicated on the graph.

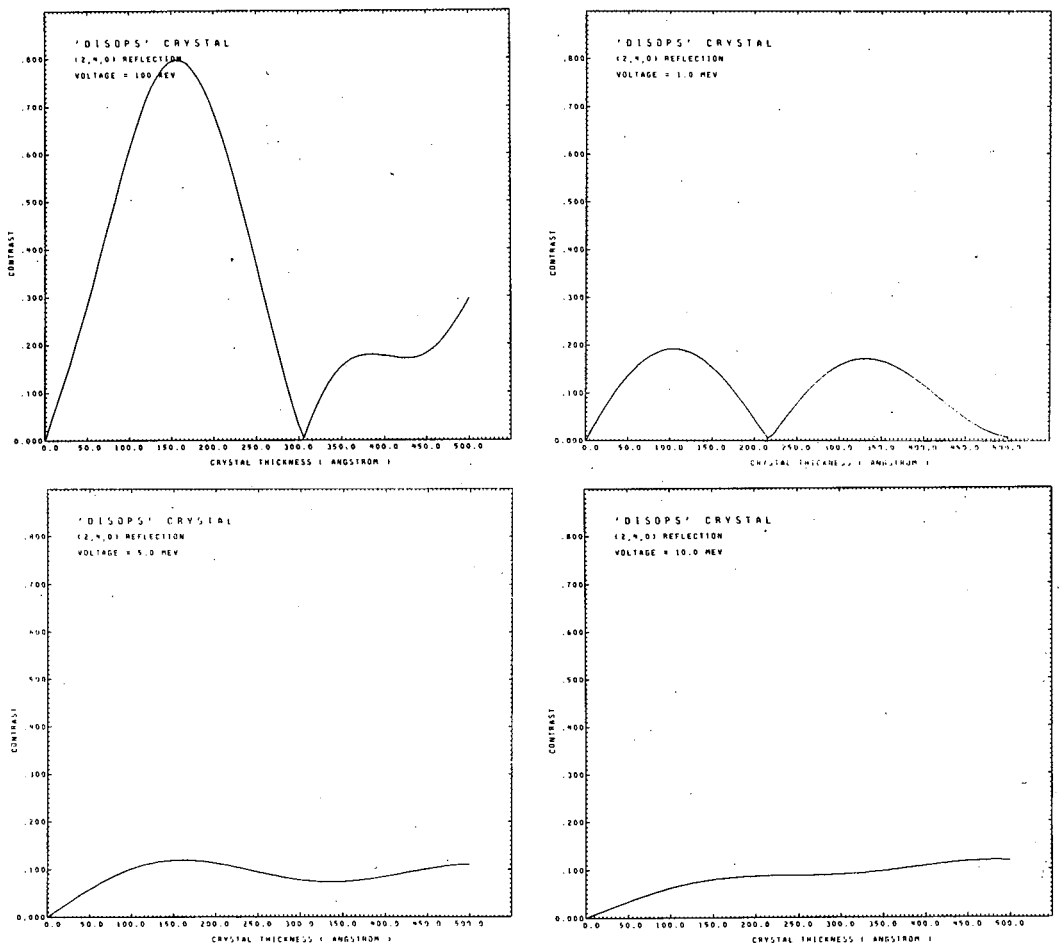

XBL 753-356

Fig. 22c. Resolution dependent contrast for the (2,4,0) reflection is plotted as a function of crystal thickness. The crystal is 'DISOPS'. The electron accelerating voltage used is indicated on the graph.

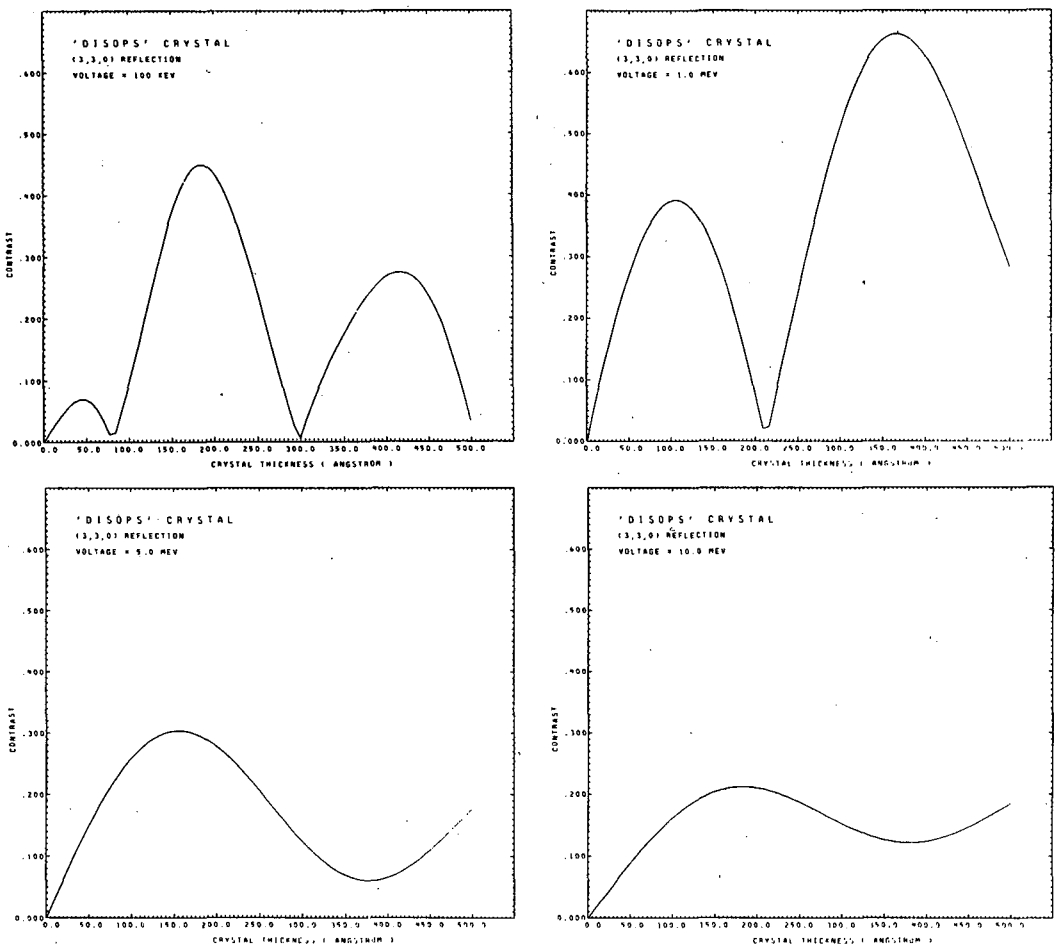

XBL 752-353

Fig. 22d. Resolution dependent contrast for the (3,3,0) reflection is plotted as a function of crystal thickness. The crystal is 'DISOPS'. The electron accelerating voltage used is indicated on the graph.

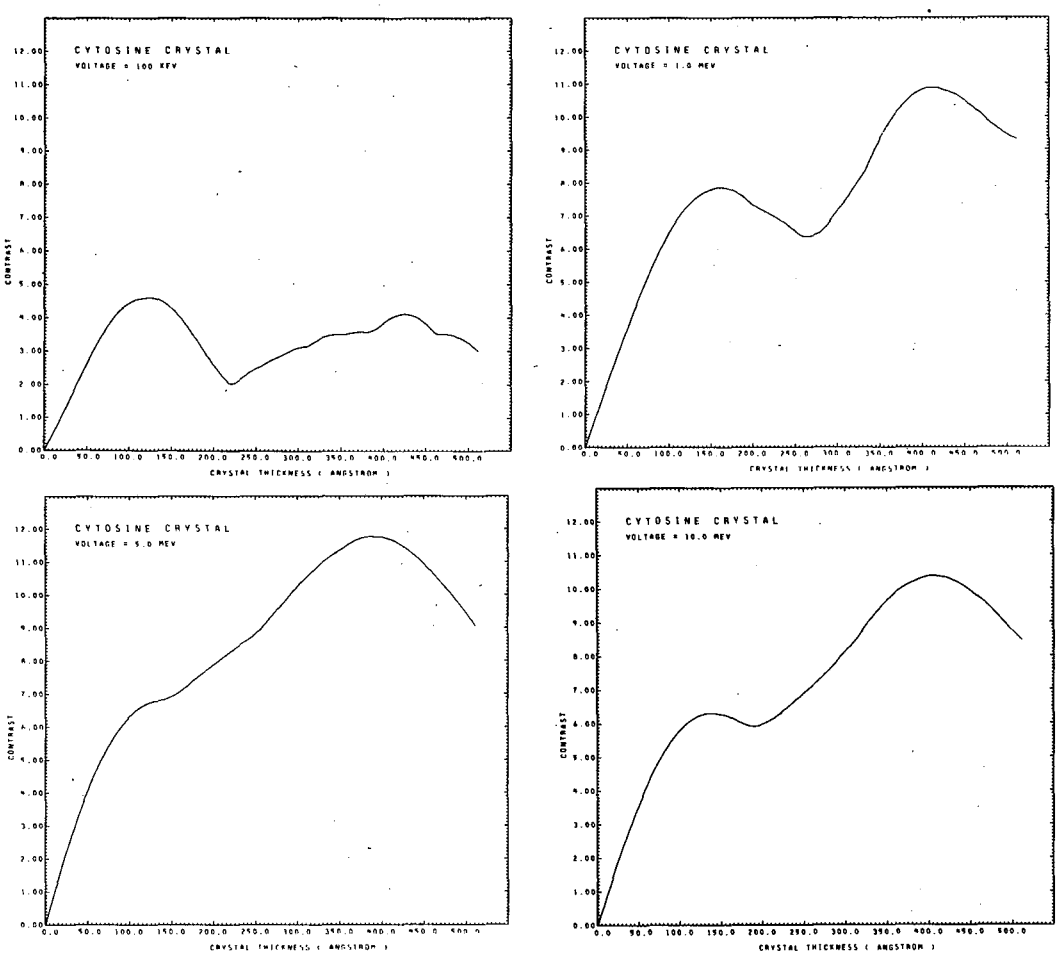

XBL 752-349

Fig. 23a. Integrated contrast as a function of crystal thickness. The crystal is cytosine. The accelerating voltage used is indicated on the graph.

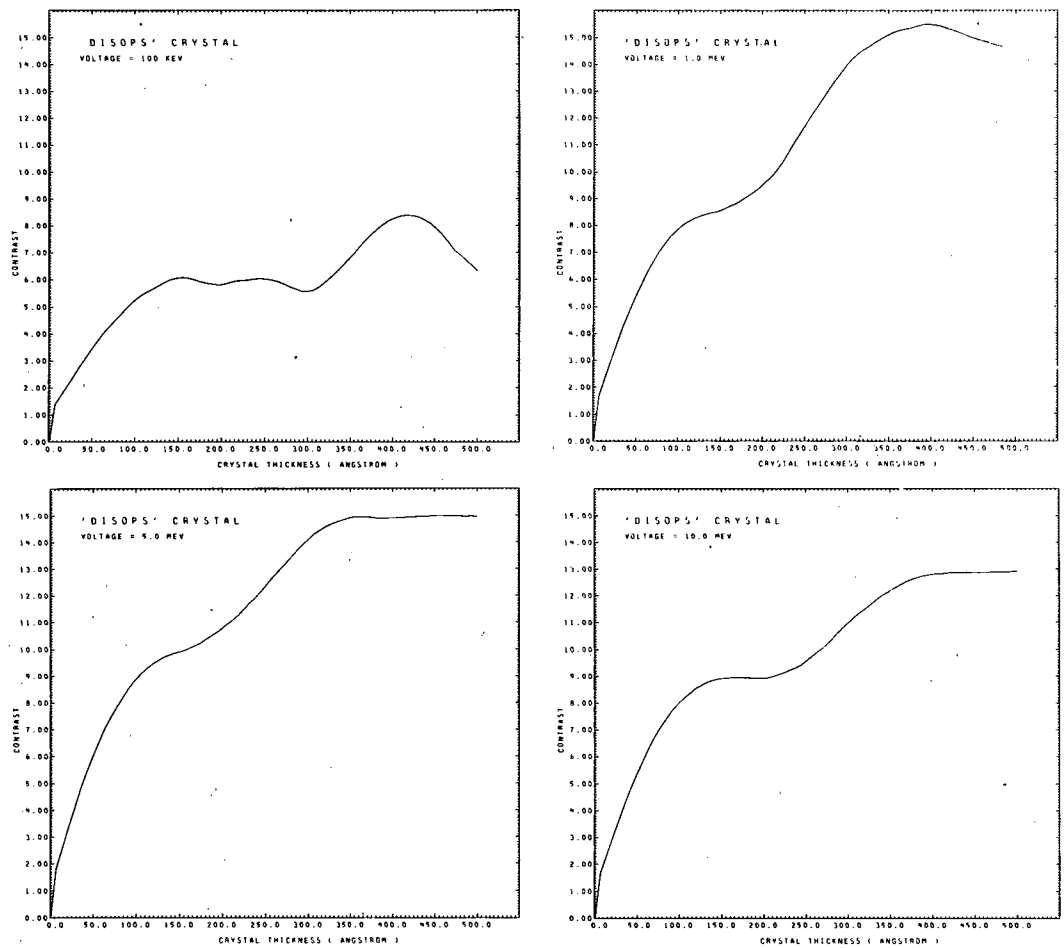

XBL 753-357

Fig. 23b. Integrated contrast as a function of crystal thickness. The crystal is 'DISOPS'. The electron accelerating voltage used is indicated on the graph.

VI. CONCLUSION AND SUMMARY

The kinematic approximation, the phase object approximation and the multislice dynamical approximation have been derived following Feynman's path integral formulation of quantum mechanics. The higher order phase object approximation has, for the first time, been developed in order to extend the validity domain of the phase object approximation and still preserve the invertible relationship between the projected potential and the transmitted wave function. The validity of these approximations was discussed and their validity domains were evaluated.

Kinematic Approximation

The validity domain of the diffracted beam intensities in the kinematic approximation is limited at 100 keV to a crystal thickness of less than 100 Å, whereas the validity of their phases is confined to a much smaller crystal thickness. These domains stay approximately the same as electron energy increases. It can be said then that the validity of the kinematic approximation for the structural investigation of organic crystal is confined to a very small crystal thickness.

Phase Object Approximation

The validity of the diffracted beam intensity in the phase object approximation at 100 keV is confined to a smaller crystal thickness than that in the kinematic approximation. The validity of the phases of the diffracted beams extends, however, to a larger crystal thickness. The validity of the phases together with the amplitudes in the phase object approximation decreases either with increasing spatial frequency or with

increasing crystal thickness; but this validity increases as electron energy increases.

Higher Order Phase Object Approximation

The validity domain of the higher order phase object approximation at 100 keV was evaluated. It was demonstrated that the higher phase object approximation, when compared to the phase object approximation, possesses a larger domain of validity for the retrieval of the projected potential.

The effect of high voltage to the contrast of organic crystal images under "optimum defocus condition" has also been studied. It was shown that the contrast increases with increasing electron energy. The increase in contrast will definitely lower the electron exposure needed to obtain an acceptable signal-to-noise ratio and allows the beneficial reduction in radiation damage.

One can conclude that high voltage electron microscopy not only gives a larger domain for the retrieval of the projected potential by the phase object approximation, but also gives an increase in contrast. This increase can be beneficial for reduction in radiation damage.

Future Applications to Biological Specimens

Within their validity domains, both the phase object approximation and the higher order phase object approximation can be properly used to obtain the true structural information when the phases and amplitudes of the diffracted beams are known. Several attractive techniques such as half aperture holography have been proposed in the literature for the recovery of the diffracted waves. Future research will be to retrieve

the correct object structure from the high resolution object image and the diffracted beam intensities. This method will be applied to obtain the true projected potential of biological specimens such as gap junction membranes which are believed to be the site of cell to cell communication, catalase crystal and tabacco mosaic virus. The three dimensional reconstruction of these objects at high resolution will be our ultimate goal.

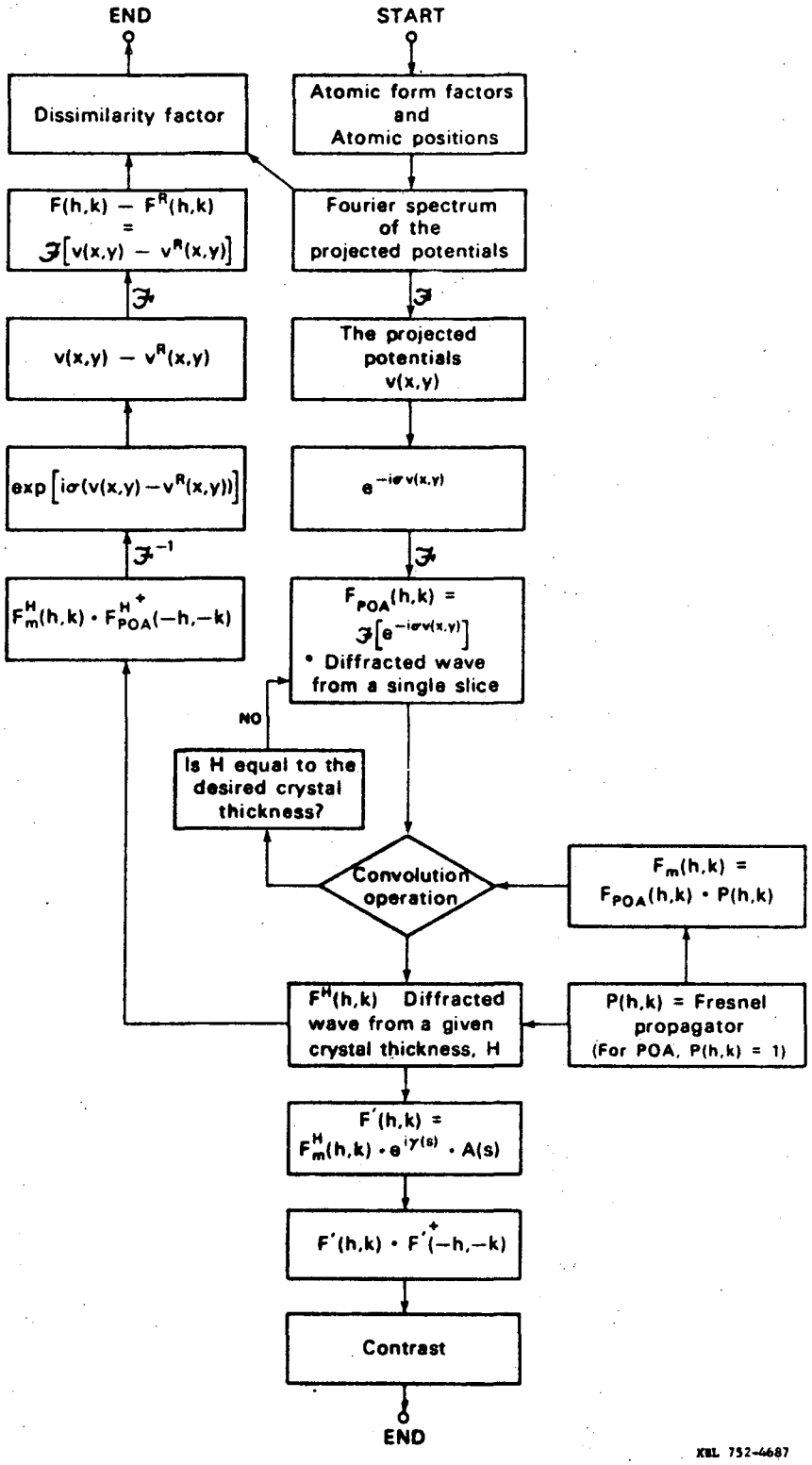

Diagram 1. The flow diagram.

APPENDIX A

The Validity of the Kinematic Approximation for the Structural Determination of Biological Structures by Electron Microscopy

The scattering of electrons by a three dimensional potential field must, in principle, involve multiple scattering processes. An electron wave is perturbed several times as it passes through the three dimensional potential field. In other words, an electron which is scattered from one part of the potential field has the probability to be scattered again and again as it passes through the other parts of the three dimensional potential. When the multiple scattered electron waves are related to one another in a systematic way, this type of multiple scattering is referred to as dynamical scattering. It can be expected, therefore, that the dynamical scattering effect is especially important in the structural investigation of crystalline materials by electron microscopical imaging technique. This is because the potential field of one part of the crystalline object can be related systematically to the other part. Furthermore, the electron waves used for imaging must possess an appreciable degree of coherency. Thus it is clear that the dynamical scattering effect may play an important role in the image of an appreciably thick crystal.

For a thin biological object, the number of electrons which undergo multiple scattering processes can be expected to be quite small compared to that of the single scattered electrons at small angles. This number can, however, be quite significant when compared to the number of single scattered electrons at large angles. This means that even for a thin specimen, the dynamical scattering effect may play an important role in the high resolution information of the image. In fact, study from electron

diffraction by gas molecules of high atomic number has shown that the single scattering approximation (kinematic approximation) is inadequate for the structural determination of the molecule (Glauber, R. and Schomaker, V., 1953). For an increasingly thick specimen, the contribution of the multiple scattered electrons to the number of scattered electrons at a small angle becomes increasingly significant. The dynamical scattering effect for a thick crystal can be anticipated to be important even for the low resolution image.

Erickson and Klug (1971) have studied experimentally the image formation using a thin ($\sim$ 200 Å) negatively stained catalase crystal and have shown that the medium resolution ($\sim$ 20 Å) image followed the linear theory of image formation. This indicates that the dynamical scattering effect plays an insignificant role in the medium resolution image of a thin, negatively stained crystal. It should be pointed out, however, that their determination of the defocus value, based on the radius of the rings of the maximum and minimum noise intensity of the optical transform of the image, is not appropriate since the stained material does effect the radius of the rings. Furthermore, the contribution of the dynamical scattering effect cannot be separated from the contribution of the amplitude contrast in the first order theory of image formation.

Following the same technique used in the case of the thin specimen, Erickson and his collaborator (Voter and Erickson, 1974) have recently shown that, for a thick negatively stained catalase crystal, the low resolution information of the image followed the first order theory while the medium resolution information deviated significantly. It is clear that for a thick crystal, the dynamical scattering effect plays a

dominant role in the medium resolution information.

Dorset and Parsons have reported that the total diffracted beam intensities for a fully hydrated catalase crystal is, for crystal thickness up to $\sim$ 3000 Å, small relative to the incident beam intensity. Based on this fact, they indicated that the kinematic diffraction theory is a valid approximation for treating the intensity data. This criterion is, however, not a sufficient condition for assuming the validity of the kinematic approximation. Calculations (Chapter III) have shown that although the total diffracted beam intensities become smaller relative to the incident beam intensity as electron energy increases, the validity for the kinematic approximation does not increase. Furthermore, the validity of the kinematic approximation for treating the diffracted beam intensities does not warrant the applicability of the kinematic approximation for the structural determination of the crystal since calculations have also shown that the phases of the diffracted waves have a smaller validity domain when compared to the validity domain of the diffracted beam intensities. Phase retrieval techniques in x-ray crystallography, such as isomorphous replacement technique, may therefore, not be used to obtain the correct phase information in electron diffraction study.

APPENDIX B

Evaluation of the Integral [in Equation (8)]

For the far field region, [equation (8)], for the case where the potential $V(\vec{r},t)$ is independent of t, can be written as

$$\psi(\vec{r},t) \underset{r\to\infty}{=} \exp\left(-i\vec{k}_o \cdot \vec{r} + \left(\frac{i}{\hbar}\right) E_o t\right) + \left(\frac{i}{\hbar}\right)\int F(|\vec{r}-\vec{r}'|,t')V(\vec{r}') \exp(-i\vec{k}_o \cdot \vec{r}')d\vec{r}' \qquad [a]$$

and

$$F(|\vec{r}-\vec{r}'|,t) \underset{r\to\infty}{=} \int_0^t \left[\frac{m}{2\pi\hbar t'}\right]^{3/2} \exp\left(\frac{-im|\vec{r}-\vec{r}'|^2}{2\hbar t'}\right) \cdot \exp\left(\frac{i}{\hbar} E_o t'\right)dt' \qquad [b]$$

where t is the time required for the electron to travel from the initial point $\vec{r}_o$ to the final position $\vec{r}$. For a limited potential field $|\vec{r}| \to \infty$ means that $t \to \infty$. We can then write equation [b] as

$$F(|\vec{r}-\vec{r}'|,t) \underset{t\to\infty}{=} \int_0^\infty \left[\frac{m}{2\pi\hbar t'}\right]^{3/2} \exp\left(\frac{-im|\vec{r}-\vec{r}'|^2}{2\hbar t'}\right) \cdot \exp\left(\frac{i}{\hbar} E_o t'\right)dt' \qquad [c]$$

To simplify the integral, we substitute $\left(-\frac{im|\vec{r}-\vec{r}'|^2}{2\hbar t}\right)^{\frac{1}{2}}$ by the variable μ. We have then

$$F(|\vec{r}-\vec{r}'|,t) = -\left[\frac{-im}{\pi^{3/2}\hbar}\right] \frac{1}{|\vec{r}-\vec{r}'|} \int e^{-\mu^2 - a^2/\mu^2} d\mu \qquad [d]$$

and

$$a = -\frac{m|\vec{r}-\vec{r}'|^2}{2\hbar^2} E_o$$

The definite integral can be integrated in close form as (Standard Mathematical Tables, 1965)

$$\int_0^\infty e^{-x^2 - a^2/x^2} \cdot dx = \frac{e^{-2a}\sqrt{\pi}}{2} \qquad [e]$$

Thus, equation [d] can be rewritten as

$$F(|\vec{r} - \vec{r}'|, t) \underset{t \to \infty}{=} \frac{im}{2\pi\hbar} \left(\frac{1}{|\vec{r} - \vec{r}'|}\right) \exp\left(-\frac{i}{\hbar}\sqrt{2mE_o}\ |\vec{r} - \vec{r}'|\right) \qquad [f]$$

Noting that E_o is the energy of the free electron, we can write $E_o = \frac{(\hbar k)^2}{2m}$ where $|\vec{k}| = |\vec{k}_o|$. Equation [f] can then be rewritten as

$$F(|\vec{r} - \vec{r}'|, t) \underset{t \to \infty}{=} \frac{im}{2\pi\hbar} \frac{1}{|\vec{r} - \vec{r}'|} \exp(-ik|\vec{r} - \vec{r}'|) \qquad [g]$$

Substituting this relation into equation [a], we can finally write equation [a] as follows:

$$\psi_\infty(\vec{r}, t) = \exp\left(-i\vec{k}_o \cdot \vec{r} + \left(\frac{i}{\hbar}\right) E_o t\right) - \frac{m}{2\pi\hbar^2} \int \exp(-i\vec{k}_o \cdot \vec{r}')\, V(\vec{r}')\, \frac{\exp(-ik|\vec{r} - \vec{r}'|)}{|\vec{r} - \vec{r}'|}\, d\vec{r}' \qquad [h]$$

ACKNOWLEDGMENTS

The author is deeply grateful and indebted to Professor Robert M. Glaeser, who suggested the research topic described in this thesis, for his guidance, helpful discussions and encouragement during the course of this work. A special appreciation is also due to Professor Thomas L. Hayes and Gareth Thomas who offered many valuable suggestions and comments. I would like to thank my colleagues, Mr. D. Grano, whose program on "z-modulus display" I used, and Mr. K. A. Taylor for his stimulating discussions.

I am very thankful to my wife, Marlen, for her encouragement and her help in compiling and in typing the first draft of this thesis.

Finally, I would also like to thank Mr. John Flambard for the excellent drawings and Ms. Deberah Olson for her expert typing. This work has been supported in part by NIH Grant GM-19452-01.

REFERENCES

1. Allpress, J.G., Sanders, J.V. and Wadsley, A.D. (1969), Acta Cryst. B25, 1156.
2. Barker, D.L. and Marsh, R.E. (1964), Acta Cryst. 17, 1581.
3. Berry, M.V. (1971), J. Phys. C 4, 697.
4. Born, M. (1926), Z. Physik, 37, 863; 38, 803.
5. Cowley, J.M. and Iijima, S. (1972), Z. Naturforsch. 27a, 445.
6. Cowley, J.M. and Moodie, A.F. (1957), Acta Cryst. 10, 609.
7. Davisson, C.J. and Germer, L.H. (1927), Nature 119, 558; (1927) Phys. Rev. 30, 705.
8. Dorset, D.L. and Parsons, D. F. (1974), American Crystallographic Association, Summer meeting. Proceedings by International Union of Crystallography Intercongress Symposium on Intra- and Inter-Molecular Forces, 260.
9. Doyle, P.A. and Turner, P.S. (1968), Acta Cryst. A24, 390.
10. Eisenhandler, C.B. and Siegel, B.M. (1966), J. Appl. Phys. 37, 1613.
11. Erickson, H. and Klug, A. (1971), Phil. Trans. Roy. Soc. London B21, 105; (1970), Ber. Bunsenges. Phys. Chem. 74, 1129.
12. Fejes, P. (1972), *30th Ann. Proc. Electron Microscopy Soc. Amer.* 558.
13. Feynman, R.P. (1948), Rev. Mod. Phys. 20, 367.
14. Feynman, R.P. and Hibbs, A.R. (1965), *Quantum Mechanics and Path Integrals*, McGraw-Hill Book Company.
15. Frank, J. (1974), J. Phys. D 7, L75.

15a. Fujiwara, K. (1959), J. Phys. Jap. 14, 1513.

16. Glaeser, R.M. (1971), J. Ultrastruct. Res. 36, 466.

17. Glaeser, R.M. (1974), *High Voltage Electron Microscopy*, Swann, P. R., Humphreys, C.J., and Goringe, M.J., editors, Academic Press.

18. Glaeser, R.M. (1975), in *Physical Aspects of Electron Microscopy and Microbeam Analysis*, Siegel, B., editor, John Wiley & Sons.

19. Glaeser, R.M. and Thomas, G. (1969), Biophysical Journal 9, 1073.

20. Glaeser, R.M., Kuo, I. and Budinger, T.F. (1971), *29th Ann. Proc. Electron Microscopy Soc. Amer.*, 466.

21. Glauber, R. and Schomaker, V. (1953), Phys. Rev. 89, 667.

22. Hui, S.W. and Parsons, D.F. (1974), Science 184, 77.

23. Hashimoto, H., Kumao, A., Hino, K., Endoh, H., Yotsumoto, H., and Ono, A. (1973), J. Electron Microsc. 22, 123.

24. Iijima, S. (1971), J. Appl. Phys. 42, 5891.

25. Imamov, R.M. and Pinsker, Z.G. (1965), Kristallografiya, 10(2), 199.

26. *International Tables for X-Ray Crystallography* (1968), 2, 218 (published by the International Union of Crystallography).

27. Joy, R.T. (1973), Advan. Opt. Electron Microsc. 5, 297.

28. Knoll, M. and Ruska, E. (1932), Ann. Phys. 12, 607.

29. Kuo, I. (1975), Ph.D. Thesis, University of California, Berkeley.

30. Lake, J.A. (1972), *Optical Transforms*, Lipson, H., editor.

31. Lynch, D.F. (1973), Acta Cryst. A30, 101.

32. Matricardi, V.R., Moretz, R.C. and Parsons, D.F. (1972), Science 177, 268.

33. Moliere, G. (1947), Naturforsch. 2a, 133.

34. Moodie, A.F. (1965), International Conference on Electron Diffraction and Crystal Defects, Melbourne.

35. Moodie, A.F. (1971), "Dynamical n-Beam Theory of Electron Diffraction", in *Encyclopaedia Dictionary of Physics Supp.*, Vol. 4, 69, Thewlis, J. editor.

36. Nelson, E. (1964), J. Math. Phys. 5, 332.

37. Olsen, H., Maximon, L.C. and Wergeland, H. (1957), Phys. Rev. 106, 27.

38. Ottensmeyer, F.P., Schmidt, E.E., and Olbrecht, A.J. (1973), Science 179, 175.

39. Parsons, D.F. (1968), *Int. Rev. of Expt. Path.*, G.W.Richter and M.A.Epstein, editors, Academic Press, New York.

40. Parzen, G. (1951), Phys. Rev. 81, 808.

41. Quon, W.K. (1970), Ph.D. Thesis, University of California, Berkeley.

42. Schiff, L.I. (1955), *Quantum Mechanics*, McGraw-Hill Book Co., p. 161.

43. Schiff, L.I. (1956), Phys. Rev. 103(2), 443.

44. Schiff, L.I. (1968), *Quantum Mechanics*, McGraw-Hill Book Co., p. 341.

45. Schomaker, V. and Glauber, R. (1952), Nature 170, 290.

46. Scott, W.T. (1963), Rev. Mod. Phys. 35, 231.

47. Shetten, J. (1969), J. Amer. Chem. Soc. 91, 4545.

48. Siegel, B.M. (1971), Berichte der Bunsengesellschaft 74, 1177.

49. Singleton, R.C. (1969), IEEE Transactions on Audio and Electroacoustics, Au-17, 2, 93.

50. *Standard Mathematical Table, 14th edition*, The Chemical Rubber Co., p. 345.

51. Stout, G.H. and Jensen, L.H. (1968), *X-Ray Structure Determination, A Practical Guide*, p. 253.

52. Taylor, K.A. and Glaeser, R.M. (1974), Science 186, 1036.

53. Vainshstein, B.K. and Pinsker, Z.G. (1949), Zh. Fiz. Khim. 23, 1058.

54. Vainshstein, B.K., Lobachou, A.N. and Stasova, M.M. (1958), Kristallografiya 3, 374, 452; (1958), Dokl. Akad. Nauk. SSSR, 120 523.

55. Voter, W.A. and Erickson, H.P. (1974), *32nd Ann. Proc. Electron Microscopy Soc. Amer.*, 400.

56. Yada, K. and Hibi, T. (1969), J. Electron Microsc. 18, 266.

57. Zeitler, E. and Olsen, H. (1967), Phys. Rev. 162, 1439.

LEGAL NOTICE

This report was prepared as an account of work sponsored by the United States Government. Neither the United States nor the United States Energy Research and Development Administration, nor any of their employees, nor any of their contractors, subcontractors, or their employees, makes any warranty, express or implied, or assumes any legal liability or responsibility for the accuracy, completeness or usefulness of any information, apparatus, product or process disclosed, or represents that its use would not infringe privately owned rights.

TECHNICAL INFORMATION DIVISION
LAWRENCE BERKELEY LABORATORY
UNIVERSITY OF CALIFORNIA
BERKELEY, CALIFORNIA 94720